Mechanical instabilities and dynamics of living matter

From single-cell motility to collective cell migration

Carles Blanch Mercader

Mechanical instabilities and dynamics of living matter

From single-cell motility to collective cell migration

PROGRAMA DE DOCTORAT EN FÍSICA

Línia d'investigació en Física de la Matèria Condensada

Director i tutor de la Tesi:

Jaume Casademunt Viader

Memòria presentada per

CARLES BLANCH MERCADER

per a optar al títol de Doctor en Física

Departament d'Estructura i Constituents de la Matèria

Facultat de Física

Universitat de Barcelona

Acknowledgements

There have been many people who have contributed directly or indirectly in this thesis, to whom I am extremely grateful for their help and support. It is not possible to express my appreciation in simple words, but still, I hope they all feel that some part of this work is theirs.

First of all, I would like to express my recognition and gratitude to Jaume Casademunt for being the advisor of this thesis and introducing me into the field of biophysics. During these years, we had long discussions and shared good moments, with which I learned a lot both at scientific and personal level. We have worked together in many projects, some of them not collected in this thesis, such as the work on the molecular motor KIF1A, or the use of graph theory to solve cooperative ratchets. From the molecular level we went to single cell motility and all the way to collective cell migration in tissues. Along this journey, I consider myself pretty fortunate to have been compelled to learn a variety of mathematical subjects such as topology, graph theory, conformal mapping or dynamical systems.

I would also like to acknowledge Jean-François Joanny, who was a source of inspiration and opened me the doors of the Institut Curie. It is complicated to express in simple terms my privileged experience there, but I deeply appreciate being influenced by his enthusiasm to put together biology and physics and establishing relations as simple as possible between both. From my stays at Institut Curie I also appreciate the illuminating and always supportive discussions with Jacques Prost on our results.

An important part of this thesis has been motivated by the recent studies on epithelial monolayers from the group of Xavier Trepat. I appreciate enriching discussion with him on this subject. In addition, I am grateful for having the opportunity to participate in his lab meetings which were extremely valuable in many senses.

I would also like to express my thanks to Àngel Jorba and Carles Simó, from the Mathematics Faculty of the University of Barcelona, who helped us to shed some light during the mathematical struggles of the problem of cell fragments

motility. They contributed with specific but extremely useful discussions on the complex mathematical issues involved in that problem.

A special acknowledgment to the members of the groups of the Consolider project and the Nonlinear Physics group at the University of Barcelona; the Physical Approach of Biological Problems group at the Institut Curie; and the Integrative Cell and Tissue Mechanics group at the Institute for Bioengineering of Catalonia.

The realization of this thesis would not have been possible without the FPU fellowship supported by the Ministry of Education and the exchange grant from the Quantissue project.

Contents

Chapter 1

General introduction

1.1 Living systems as active matter

This thesis belongs to the field of biological physics. In particular, it is devoted to the study of mechanical processes that operate at the cellular and multicellular scales. Living systems viewed from a physical perspective can be categorized as *soft active matter*. In recent years, active matter has emerged as a new paradigm in non equilibrium physics [1] that has become particularly helpful to provide new physical insights in biological systems. Active materials share the general property that they contain an internal source of energy that drives their behavior, so they are systems intrinsically out of thermodynamical equilibrium. In living matter, this source of energy is the chemical consumption of ATP. Examples of active materials cover a broad variety of physical systems, sometimes defined by collections of self-driven particles with dissipative interactions (flocks, swarms, bacterial suspensions, cells in a tissue), sometimes described as continuous media such as in the so-called theory of active polar gels [2, 3] that formulates a hydrodynamical approach to biological media such as the cell cytoskeleton, or polarized tissues. A human being is an extreme example of active matter that serves to illustrate the potential complexity that active materials can generate whenever different levels of organization at many scales are combined.

In the biological context, active materials do cover a broad spectrum of length scales, ranging from 10 nm at the level of molecular motors to 100 m for animals, with all the intermediate levels including filament networks, cells, tissues, organs and higher organisms [4, 5, 6, 7]. The collective phenomena arising from the interacting elementary units at each level of description gives rise of emerging properties of the ensemble that are not present at the level of the constituents. The concatenation of qualitatively new emerging properties from the different levels

of organization is ultimately responsible for the biological complexity. Clearly, a human being is not just a group of cells.

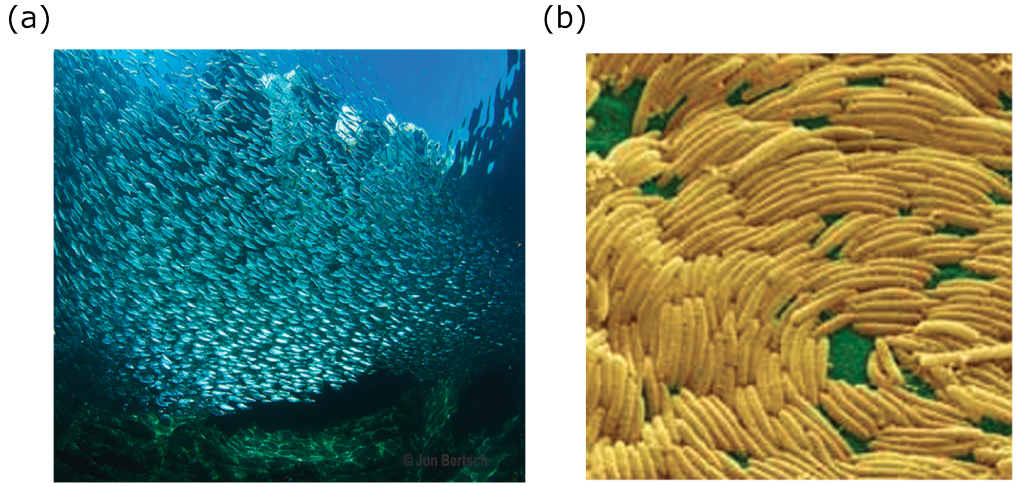

Figure 1.1: (a) A remarkable demonstration of polar order in a sardine school. Figure from Jon Bertsch, from underwater images from the Sea of Cortez: http://www.thalassagraphics.com/blog/? p=167. (b) Liquid crystalline order in a myxobacterial flock. Figure from Gregory Velicer (Indiana University Bloomington) and Juergen Bergen (Max-Planck Institute for Developmental Biology). Both figures are modified from Ref. [1].

On the contrary passive soft materials such as foams, liquid crystals, colloidal suspensions, among others, require an external forcing to drives them out of equilibrium, so that these materials dissipate the energy that is externally supplied. The distinctive features of active vs passive materials may originate qualitatively different behaviors to the same external stimuli. The shear viscosity is a measure of the resistance of a liquid to flow under a shear stress. It is well-known that the more viscous a fluid is, the slower it flows under a given shear stress. However, this statement may not be valid in general for active matter. Remarkably, the viscosity of an active suspension can effectively become zero, a strong signature of activity in the system with no counterpart in passive soft matter [8, 9].

Active processes are present already at the molecular scale. For instance actin polymerization at the cell membrane or the transport of vesicles by molecular motors. The latter are proteins that undergo cycles of conformational changes involving typically the capture and hydrolysis of ATP molecules. Molecular motors are thus the elementary units that transform chemical energy into mechanical work and motion [10, 11]. In this thesis we will be mostly concerned with the family of myosin motors which in combination with actin filaments define one of the most versatile and universal machinery of force generation in the cytoskeleton of eukaryotic cells. At a higher level of organization, the collective action of this molecular machinery is ultimately responsible of muscle contraction. If a single

molecular motor produces forces in the scale of pico-Newtons, their collective action allows to build up forces in the range of Newtons.

Actin monomers (G-actin) may also be considered as a type of molecular motor, in the sense that they also transduce chemical energy into mechanical work. These molecules are a key element in many cellular functions, involving protrusion forces, cell motility, cell division or cell signaling and are one of the main components of the cytoskeleton in eukaryotic cells [10, 12]. Their molecular structure has a well-defined polarity facilitating their assembly into a filamentous organization (F-actin), which preserves the polarity of the constituents. There exist several proteins that regulate the dynamics at both ends of the filament. The growth process from their barbed ends is known as polymerization and it is ATP-driven. The activity induces an imbalance between the processes of actin monomers assembly/dissociation that ultimately generates forces at the polymerizing end. The actin network itself can be assembled in different arrangements and is continuously been assembled at one end and disassembled in the other end generating the so-called treadmilling, an active process that is the base upon the biochemical regulation of the external stimuli.

The development of contractile forces at the cellular scale is essential for many processes ranging from cell motility to tissue morphogenesis. The molecular machinery that is responsible by those contractile stresses is the assembly of myosin motors and actin filaments in the so-called actomyosin gels. The myosin motors act as a cross-linking protein between actin filaments. Their joint collective effect depends on the filament network organization which in turn is highly regulated by the cell. Other proteins affect directly the architecture and physical properties of the actin network. In the presence of ATP, myosin-assemblies perform power strokes, which cause local deformations on the system as illustrated in Fig. (1.2). Collectively the actomyosin system provides a complex machinery that acts as a versatile muscle of the cell. These contractile forces can be transmitted to the cellular environment via adhesion proteins, like cadherin. In addition, the activity of these molecular motors affects dramatically the rheological properties of the actomyosin gel.

Other manifestations of activity in a completely different scale is the dynamics of groups of living organisms such as fish shoals, bird flocks, insect swarms or even human groups [4, 13, 14, 15]. In all these cases the units are seen as self-driven particles following some simple rules of directional motion and interaction with the immediate environment. The inner biological complexity of the individuals is here ignored, and the focus is on the emergence of nontrivial collective dynamical behavior out of such simple rules. These examples serve also to illustrate some common features of active systems. They are also distinguished from passive systems by the fact that each of their elementary units consumes some

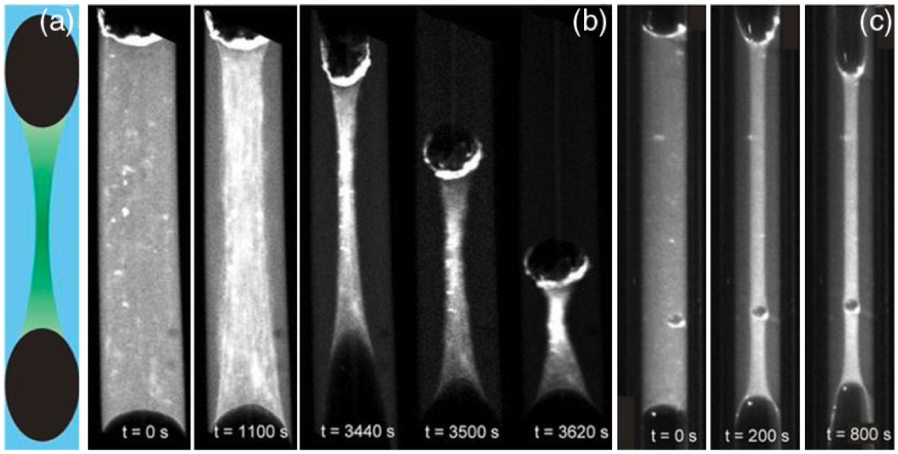

Figure 1.2: Measurements of contractile stresses in cell (Xenopus oocyte) extracts and a reconstituted actomyosin gel made using skeletal muscle myosin II thick filaments: (a) Schematic of active gel in a narrow glass capillary (inner diameter, 400 μm) sandwiched between two oil droplets. (b) Confocal fluorescence images of the network at five different time points show that the active gel first pulls away from the capillary walls and deforms the oil droplets as it contracts before reaching a breaking point when the gel collapses. (c) Dark-field images of contracting cell extract shows the same behavior. Analysis of the deformation of the oil droplet gives an estimate of the contractile force exerted by the actin gel, which consists of bundles of actin filaments cross-linked by α-actinin. This force is around 1 μN or 100 pN per actin bundle. Modified from Ref. [7].

chemical energy from internal origin, so they are also out of equilibrium. The focus in these studies is often more oriented into fundamental aspects of statistical physics describing for instance non-equilibrium phase transitions and anomalous fluctuations.

From a theoretical point of view, there is in general a deep connection between the active nature of a system and the symmetries of the system already at the level of its constituents. Indeed the system cannot be rotationally invariant and exhibit some polarity or nematic order. For instance, the filaments where molecular motors act must be polar so that a net force can be generated. A motile cell must be polarized between front and rear in order to maintain its directed motion. Similarly, the cells on a tissue inherit their polarity from that of the actin network assembly in their cytoskeleton. In the cases of groups of self-driven particles, the directionality of the particles manifestly breaks the rotational symmetry. From an abstract point of view, in the formulation of the theory of active gels, which relies on a hydrodynamic approach based on irreversible thermodynamics, this interplay between active stresses and polarity is clearly manifest. In fact, unless a vector field is available (the polarity or the director field in a non polar nematic), a chemical reaction such as the ATP hydrolysis (a scalar force) can not be coupled to the transport of momentum (a tensorial current), by virtue of the Curie

symmetry principle.

From a general perspective, the previous examples of biological systems can be ideally modeled as an active polar or nematic gel, at least to the extent that a continuum description makes sense. Along the present thesis, we use extensively the theory of active gels, which derives the constitutive equations of an active gel consistent with the constraints of the thermodynamical laws and fundamental symmetries, like time reversal [2, 3]. The elegance of this approach relies on its generality, since the number of inputs included are minimal, and all microscopic and specific details of the systems are encoded in a set of phenomenological transport coefficients. The results are then automatically generic to some extent. A possible limitation of this approach is that, as in traditional irreversible thermodynamics, it is based on a linear relation between fluxes and forces, which in some cases may not be satisfied in biological systems. In those cases the theory may still be qualitatively correct. However, if strong nonlinearities are essential, these must be specifically modeled since no general theory can be invoked. In any case, even if only as a first approach, this framework has proven extremely insightful and has contributed substantially to our understanding of biological systems, in search of general organizational principles and generic mechanisms in living matter [16, 17, 18, 19, 20, 21, 22].

The work in the present thesis, is mainly based on the approach of the theory of active polar gels and focuses on two types of biological systems: cell motility and dynamics of epithelial tissues. In the following sections we will centre our discussion on these particular cases and provide a general overview of the main aspects in which we are interested.

1.2 Actin-based cell motility

One of the most remarkable properties of living systems is their capacity to propel. Apart from inherent physical interest of self-locomotion mechanisms, this feature plays a key role in many fundamental processes in living organisms. Obviously, for unicellular organisms the capacity to migrate is essential for survival when nutrients are not sufficiently available. In collections of cells, for instance during embriogenesis, individual cells move relative to each other in order to form a multicellular organism. On the other hand, a detailed understanding of the mechanisms involved in cell migration can have a strong impact in the context of cancer diseases, since during metastasis, cancer cells invade other parts of the body by migrating through constricted environments. Cell motility in general may involve swimming of cells, in which specific structures such as cilia and flagella may operate. Here we will limit ourselves to the so-called actin-based motility, used by cells

crawling on a substrate, which involves the machinery of the actomyosin complex that is highly regulated, [23, 24, 25]. Our perspective here will be on elucidating the basic principles and mechanisms that define the physical base upon which the biochemical signaling is constructed. Examples of cell crawling span length scales between $10 - 100$ μm and velocities ranging from 1 to 10 μm/min with a typical persistence time of $10 - 100$ min.

Many efforts has been devoted on understanding the underlying molecular basis behind the locomotion of crawling cells. The interaction between Rac1 and RhoA proteins is known to be crucial to maintain the front-rear polarity in migratory cells. The former is localized at the leading edge and enhances the actin polymerization, whereas the latter is mainly distributed at the trailing edge and regulates myosin contractility. The spatial asymmetry between both proteins defines a directionality within the cell, which is necessary to sustain motion [26]. Our approach is essentially mechanistic and based on a coarse graining of the cellular components, so that the description loses details in exchange for gaining global physical insights.

In general and simple terms, the locomotion process of a crawling cell is subdivided in three steps that are performed in a cyclic manner, Fig. (1.3).

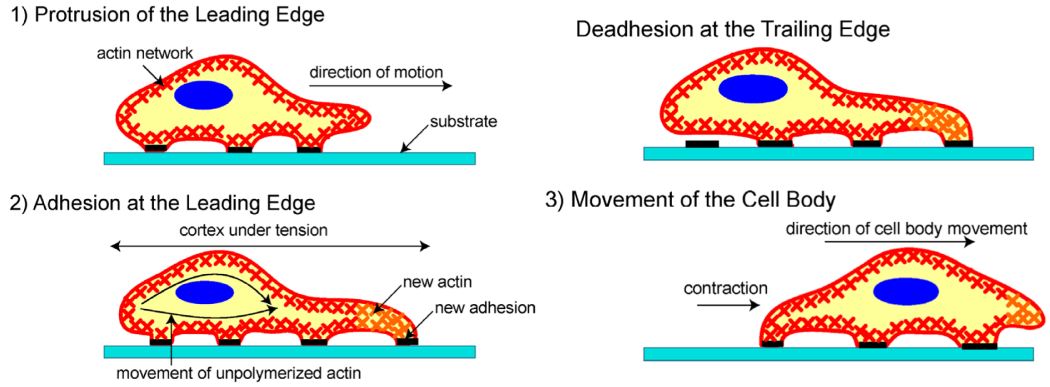

Figure 1.3: A schematic of the three stages of cell movement, based on [10, 27]: after determining its direction of motion, the cell extends a protrusion in this direction by actin polymerization at the leading edge. It then adheres its leading edge to the surface on which it is moving and de-adheres at the cell body and rear. Finally, it pulls the whole cell body forward by contracile forces generated at the cell body and rear of the cell. Modified from Ref. [28].

1. At the front of the cell, the actin is assembled into an organized network which polymerizes beneath the cell membrane with the help of regulatory proteins like Wasp. Other proteins like Arp2/3 cooperate to form new branches of actin in old filaments, controlling the architecture of the network together with cross linking or capping proteins [29]. This complex

nearly two-dimensional structure that is formed in the front of the cell is called the lamellipodium. It develops protrusion forces at the front due to actin tread milling displacing the cell membrane in the direction of migration. This process induces a net retrograde flow of actin filaments towards the rear part of the cell, where actin depolymerize.

2. Cell-substrate adhesion proteins like integrins are recruited at the new region created at the leading edge. Some of these proteins form complexes that link the lamellipodium to the underlying substrate, so that the forces induced by the backwards flow of the actin network are transmitted to the substrate. Thereby, new adhesive junctions are formed at the leading edge. Simultaneously, at the rear part of the cell, the old adhesions disappears causing an imbalance of forces. Myosin motors mainly concentrated at this rear region, help to depolymerize actin filaments and disassemble cell-substrate anchoring complexes.

3. Ultimately, the trailing edge retracts in part due to the collective contractile forces of myosin motors, inducing a prograde flow, that transport depolymerized actin monomers towards the leading edge.

As we will discuss in the specific introduction of Chapter 2, it has been observed that isolated pieces of the above machinery seem to be autonomously motile [30, 31]. These interesting experiments by Verkhovsky and co-workers raised the question of determining the minimal ingredients to produce sustained motion based on actin. A more detailed description of the context and the appropriate references will be provided in the introduction of Chapter 2.

1.3 Tissue growth and form

One of the most formidable challenges in understanding the physical basis of biological complexity is the study of the development of an organism out of a single cell. In general terms, how an embryo evolves and shape emerges as a collective property of highly coordinated dynamics of proliferating and moving cells is far from being understood. An important and most common focus on this study is obviously on genetic control and the dynamics of morphogens. It is less common to focus on the interplay between the biochemical regulation and the mechanics of the tissue.

Drosophila melanogaster is considered a convenient model system to investigate the molecular mechanisms involved in the control of the shape and the formation of patterns in tissues. Understanding the fundamental mechanisms underlying the

complex co-regulation of signaling patterns and cell mechanics that ultimately give rise to tissue growth and remodeling becomes a great challenge. At the cellular level, cell division, cell death, cell shape changes and cell rearrangements, are identified as the principal processes involved in tissue shaping [32]. Their long-range coordination may depend on the spatial distribution of proteins such as growth factors, which promote cell division. Conversely, local intracellular compression induced by cell division may trigger cellular signaling cascades that determine cell fate.

In particular our focus of attention in this area originates in the development of the imaginal disk of the wing of *Drosophila melanogaster*. During this process, the number of cells increase 3 orders of magnitude after continuous replication, resulting in an increment of the apparent radius of the one cell-thick wing from 10 μm at the early larva stage to 100 μm at the pupal stage. The existence of a mechanism that regulates the size of the tissue is manifested in the fact that the cell division events are randomly distributed throughout the monolayer but still, when it acquires the shape of the adult wing, cells enter into a quiescent state. The cell adhesion molecule Fat, which triggers the Hippo pathway [33], or the morphogen Dpp, both regulating tissue growth [34, 35], have been invoked to model the latter mechanism. In parallel, long-range oriented cell division contributes to some extent to the elongation of the wing disk during its development [36]. The cell polarity pathways, such as Dachsous and Fat [37], may be implicated in the molecular bases of the mechanisms involved in the global reorientation of the axis of cell division.

Our point of view here will be to try to understand the interplay between the different physical forces that come into play in a growing tissue, including both passive and active ones, and the actual shape that they spontaneously generate. The spirit of this purely physical and very simplistic approach is not to provide a realistic description of a morphogenetic process, but to understand the mechanical base upon which the biological regulation must operate. We will thus determine the different shapes that can be expected in a broad range of different physical parameters and conditions and as a function of time in the absence of any biological regulation. The effects of relaxing some of the simplifying assumptions will also be discussed.

A more detailed description of the context and the appropriate references will be provided in the introduction of Chapter 3.

1.4 Epithelial tissues

Epithelial cells forms cohesive layers usually covering organs, like the intestine. Despite the variability of morphologies and structure, these cells usually develop protective tasks. The part of the membrane in contact with the external environment is called the basal membrane, whereas on the opposite side, the membrane pointing towards the interior of the organ is called apical membrane, which is distinguished by the presence of microvilli and primary cilium [38]. Both domains have a differential composition of lipids and proteins, so that the internal architecture of these cells, defines a directionality (i.e apical-basal polarity). The maintenance and control of this polarity allows to adapt the cell shape as well as the directional transport of epithelial functions. The specific molecular mechanisms involved in the formation of this asymmetry are yet to be elucidated, although the PAR complex, the Crumbs complex and the scribble homologue have been identified as the major polarity complexes, [39, 40].

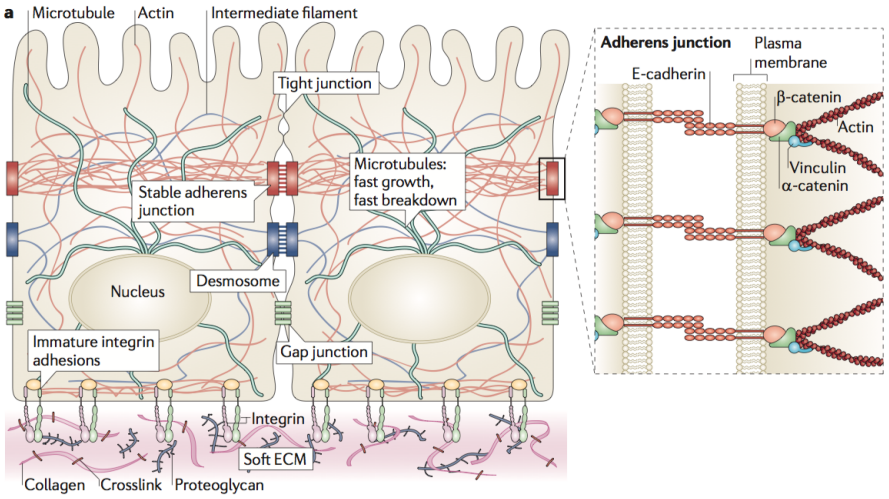

Figure 1.4: Tissues are mechanically integrated structures, the physical behaviour of which is defined by interconnected networks of cell-cell junctions, cell-matrix adhesions, intracellular filament networks (of actin, microtubules and intermediate filaments) and the extracellular matrix (ECM). Embedded throughout the network are mechanotransducing machines that convert mechanical stimuli into biochemical signals. This process, termed mechanotransduction, enables cells and tissues to sense and respond to their physical surroundings. The ECM controls network connectivity and tension on the network, thereby regulating sites of mechanotransduction. Modified from Ref. [41].

Epithelial cells tend to assemble into monolayers bound together by lateral adhesions subdivided in tight junctions, adherens junctions, desmosomes and gap junctions. These cell-cell linkers stabilize the apical-basal polarity and they are in-

volved in the cohesiveness of the monolayer, [42, 43]. The main adhesive complexes in the adherens junctions are the cadherin-catenin and nectin-afadin complexes [44]. From one side, they are connected to the equivalent complex of the adjacent cell, forming an extracellular union, whereas from the other side they are connected to the actin filaments and microtubules via cytoplasmatic proteins, like α-catenin or afadin [45, 46, 47]. Alternatively, tight junctions separate physically the apical domain from the rest of the cell, while forming a link between neighboring cells [48]. These junctions also mediate some intracellular signaling pathways [49].

At the basal membrane, the interaction with the outer medium can be mediated by protein complexes, like focal adhesions. These elements are known to translate the external mechanical cues into biochemical signals that might trigger changes at the cellular scale. In addition, focal adhesions establish a mechanical link with the cytoskeleton, so that epithelial cells can exert physical forces onto their surroundings [41].

Collective cell migration in epithelial tissues involves complex coordination of cell movements and is an essential mechanical phenomenon that is directly relevant to a variety of biological processes including wound healing, tissue morphogenesis or cancer invasion. Our theoretical study was inspired by a series of pioneering experiments by the group of X. Trepat [5, 50, 51] where valuable mechanical information could be obtained locally across the tissue. A more detailed description of the context and the appropriate references will be provided in the introduction of Chapter 4.

1.5 Outline of the thesis

The main goal of the thesis is to understand and characterize different mechanical instabilities and dynamic behavior of living matter, from the scale of a single cell to that of tissues.

The theoretical framework used treats the biological systems as active polar gels. This type of materials are intrinsically out of equilibrium, due to the continuous source of energy supplied by the out-of-equilibrium ATP hydrolysis. Within a certain range of validity the cells, cytoskeletons, tissues, schools of fish etc are expected to satisfy the same material properties as an active gel. Our approach, coarse-grains the systems by assuming that the large-scale and long-time limit is well described by a limited number of continuum fields, like the density of cells or the velocity and polarization of actin gels, depending on each particular case. This theory is a natural generalization of the hydrodynamics of liquid crystals

[52], where the role of the nematic director is played by the polarization of the biological materials, usually made of polar semi-flexible filaments.

The thesis is organized as follows.

- In Chapter 2, we show that actin lamellar fragments driven solely by polymerization forces at the binding membrane are generically motile when the circular symmetry is spontaneously broken, with no need of molecular motors or global polarization. We base our study on a nonlinear analysis of a recently introduced minimal model for an actin lamellar fragment. We prove the nonlinear instability of the center of mass and find an exact and simple relation between shape and center-of-mass velocity. A complex subcritical bifurcation scenario into traveling solutions is unfolded, where finite velocities appear through a non-adiabatic mechanism. Examples of traveling solutions and their stability are studied numerically.

- In Chapter 3, we study and classify the time-dependent morphologies of polarized tissues subject to anisotropic but spatially homogeneous growth. Extending previous studies, we model the tissue as a fluid and discuss the interplay of the active stresses generated by the anisotropic cell division and three types of passive mechanical forces: viscous stresses, friction with the environment and surface tension at the tissue boundary. The morphology dynamics is formulated as a free-boundary problem, and conformal mapping techniques are used to solve the evolution numerically. We combine analytical and numerical results to elucidate how the different passive forces compete with the active stresses to shape the tissue in different temporal regimes and derive the corresponding scaling laws. We show that in general the aspect ratio of elongated tissues is non-monotonic in time, eventually recovering isotropic shapes in the presence of friction forces, which are asymptotically dominant.

- In Chapter 4, we study the collective cell migration occurring in expanding cohesive epithelial cell sheets. This process involves the coordination of single cell traction forces, which are mechanically transmitted to adjacent neighbors via cell-cell junctions. The maps of reactive intracellular forces display a complex and heterogeneous spatio-temporal distribution. In order to understand the physical properties of the expanding tissue emerging from this collective phenomenon, we describe the system as an active polar fluid incorporating the active traction forces onto the elastic substrate. The analytical stress and velocity profiles are directly compared with the experimental measurements of expanding MCF10a and MDCK cell sheets, so that we are able to track the temporal variations of the active cellular

traction force, the nematic correlation length and the effective viscosity at time scales within $\sim 10 - 1000$ min.

In the second part of Chapter 4, we generalize the previous biophysical model by incorporating a more realistic description of the material properties of an active gel. In particular, we include contractile active stresses originated in part from the interaction between myosin motors and the intertwined actin meshwork within epithelial cells. We unveil a transition from the homogenous polarized state into an oscillatory periodic pattern in which both active contributionr contained in the model play a qualitatively different role. On the one hand, the onset of the instability depends on the contractile stresses, whereas traction forces controls the wave velocity. Interestingly, the complex material properties of an active gel allows to sustain elastic-like waves in viscous media, which are fueled by activity. We classify in a phase-diagram the nonlinear steady profiles originated from random perturbations over the reference state, showing a rich variety of dynamical phenomena. We perform a weakly nonlinear analysis to classify the dynamics in the context of the Complex Ginzburg-Landau equation. Finally, we extent the analysis for a $2d$ system in order to characterize the mechanical patterns observed in expanding epithelial sheets in $2d$ confined geometries.

- The conclusions and perspectives of the thesis are drawn in Chapter 5.
- To fullfil the requirements of the University of Barcelona, in Chapter 6 we include a summary of the thesis in catalan. In this summary we briefly review the most relevant results in each chapter.
- Finally, Chapter 7, is devoted to the supplementary information that provide useful details regarding some technical aspects of the contents of each chapter.

Chapter 2

Spontaneous motility of actin lamellar fragments

2.1 Introduction. Cell fragments as models systems for motility

Cell motility is deeply connected to spontaneous symmetry-breaking and maintenance of functional asymmetry. In the context of actin-based motility of crawling cells, the transition from a roughly circular static cell to a motile cell has been an important focus of attention in recent years in experiments, theory and numerical simulation, in a effort to explain the shape of motile cells such as keratocytes and fibroblasts and the mechanical mechanisms behind the complex acto-myosin system that sustains motion [23, 24, 25]. Remarkably, fragments of cells that contain the acto-myosin machinery but lack essential cell components, have also been shown to undergo such transitions to self-sustained motion [30, 31]. It remains unclear, however, to what extent molecular motors and global polarisation of such fragments are fundamental to achieve and sustain motion or, on the contrary, polymerisation forces alone can couple to the shape providing a motility mechanism without an external or intrinsic symmetry-breaking of the dynamics.

From a physical point of view, it is customary to construct minimal models of reduced complexity to elucidate the underlying mechanisms that connect shape to motion in such systems, and the role of the different biological ingredients that are present in real motile cells [53, 54]. Within this spirit, a hydrodynamic approach based on the theory of active polar gels [2, 3] has been proposed as a minimal model for cell lamellar fragments [55]. It has been shown that in the presence of high friction with the solid substrate, the actin gel dynamics can be approximated by a simple 2d Darcy flow, in similar conditions to viscous fingering

in Hele-Shaw cells, a well-known paradigm of interfacial pattern formation [56, 57, 58]. However, the problem differs from viscous fingering in some fundamental aspects and thus it can be viewed also as a new prototype system in the context of Laplacian growth phenomena. In Ref. [55], it was found that acto-myosin fragments do exhibit a viscous-fingering-like morphological instability, but the fundamental question of whether such a model contains the minimal ingredients to initiate and sustain motion remained unsolved. Extensions of this model to include an explicit symmetry-breaking of the dynamic equations to generate motility have also been reported [59]. Here we show that spontaneous symmetry-breaking of the circular shape is sufficient to initiate and sustain motion, even in the absence of myosin motors and large-scale polarization, when nonlinearities are taken into account. We obtain an exact connection between geometry and kinematics of the fragments, showing that motile shapes are indeed generic. By means of conformal mapping techniques we unfold a complex bifurcation scenario in the transition from static to traveling states, where nonadiabatic effects confer a finite velocity to the traveling solutions.

2.1.1 Locomotion of lamellar fragments

In this section we will discuss some of the experimental features observed in lamellar actin fragments and keratocytes that essentially motivated the present study.

Cell migration requires the co-ordination of a large number of elements to sustain an intrinsic asymmetry within the cell. In the case of crawling motility such asymmetry is manifest in the differentiated role of the front and the rear part of the cell. Keratocytes are able to maintain for a long time a fast and directional migration, even in the absence of external stimuli. Unlike the case of fibroblasts, the mechanism by which keratocytes generate a front-rear asymmetry does not require the action of microtubules. The overall picture is that the leading edge of the keratocytes has a lamellipodium architecture, whereas at the rear part, the cell contraction occurs due to the interplay between myosin II and actin. Remarkably, in Ref. [30], it was shown that the components necessary to sustain the functional asymmetry in keratocytes are also present in lamellar fragments obtained from the keratocyte lamellipodia. Even though they are subunits notably simpler than the intact cells, they are capable to migrate directionally in a persistent manner, Fig. (2.1). These results suggest that the machinery involved in lamellipodia-based motility (i.e the actin-myosin II system) is capable to generate the asymmetry and sustain directed motion without a specific regulation or large-scale coordination. Specifically, a standing circular lamellipodial fragment initiates migration after being pushed by a stream from a micropipette and, after a transient, it acquires a steady motile state, as the one shown in Fig. (2.1).

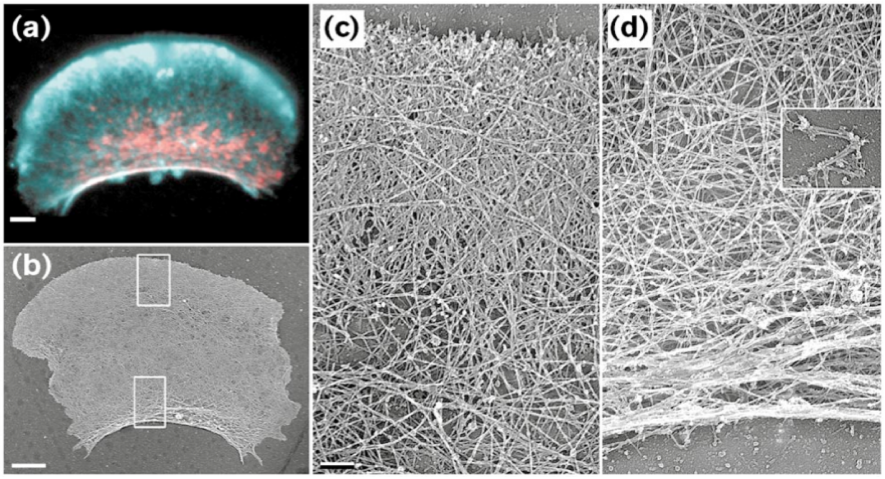

Figure 2.1: Cytoskeletal organization of (a - d) a keratocyte fragment undergoing locomotion. Reproduced from Ref. [30]

During the transition from a static into a motile state, the keratocytes undergo a sequence of structural changes. In stationary circular keratocytes, the actin flows inwards preserving the radial symmetry. The initiation of motion could be triggered either via a transient mechanical or chemical stimulus, [23, 30]. After the symmetry-breaking, the rear actin assembly reorganize and orients along the migration direction, followed straightaway by a global retraction and the structural change of the leading edge, which ultimately leads to the persistent movement of the entire cell. It is observed that the inhibition of myosin II, reduces notably the frequency of motility initiation, while a stimulation of the activity of these molecular motors produces an increase of this frequency, [23]. Among the variety of roles of myosin II, it is remarkable for instance that the stimulation of stationary keratocytes by means of the myosin II activator, calyculin A, can start the transition into a motile state. These molecular motors control a broad spectrum of tasks involved in cell motility, such as cell body translocation, traction force production or actin network disassembly, [24, 31]. With respect to the former there are two different pathways of actin disassembly, one of which is controlled by myosin II, [24]. Nevertheless, the inhibition of myosin, despite changing the flow field patterns within the cell, turns out to be insufficient to prevent locomotion by itself. It is necessary to combine it with the stabilization of the actin network via Jasplakinolide to completely block cell motility, [24].

2.1.2 Previous theoretical approaches

In the recent years, there has been an increasing interest in understanding the detailed physical mechanisms underlying and controlling cell locomotion. In this

section, we will briefly overview a small portion of the large body of theoretical work related to this topic.

In Ref. [60], the authors analysed two motility mechanisms via numerical simulations of contractile droplets placed in 2 and 3 dimensional environments. In the absence of actin tread-milling as the driving force of motility, [18, 59, 61], the active contractility turns out to be an alternative way for cells to migrate, provided that the activity of the molecular motors surpasses a certain threshold, Fig. (2.2). Interestingly, in a $2d$ configuration the cell-substrate interactions affect differently the propagation velocity of the contractile droplets depending on whether the dominant mechanism is based on the tread-milling of actin or the contraction of the cytoskeleton via molecular motors. The former mechanism generates higher travelling velocities for larger values of the friction coefficient, whereas the latter mechanism is in essence the opposite. Therefore, as supported by experimental studies of epithelial tumors, $3d$ cell motility could be mainly driven by the contractile stresses. In order to get better insights on the physics behind this mechanism, the authors of Ref. [62] investigated analytically the $3d$ migration of active contractile droplets, including in addition the effects of the resistive forces from the passive external medium.

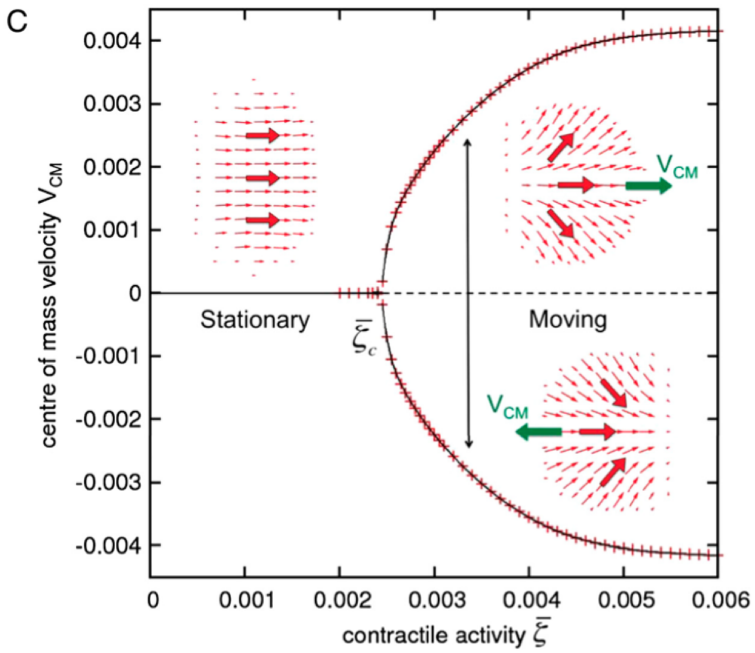

Figure 2.2: Bifurcation diagram showing spontaneous symmetry breaking from a uniform and stationary state to a splayed and moving state as the activity parameter $\bar{\zeta}$ is increased. Reproduced from Ref. [60]

Nevertheless, there are other theoretical works on crawling mechanisms that involve and explicit treatment of the active contractile stresses as a fundamental

ingredient. In simple terms the mechanism studied in Ref. [63] is based on a sustained cortical flow due to an instability of the cortex controlled by the activity of molecular motors. Alternatively, in Ref. [64] a motility mechanism is analysed that grounds on a self-sustained advection of molecular motors compensated by diffusion effects, which ultimately results into a transition from a stationary into a motile state, provided that there is a spontaneous symmetry breaking in the system. Remarkably, in Ref. [65] using the same prototypical model of a crawling cell, the original idea of finding the optimal concentration of molecular motors within the cells that maximises the efficiency of self-locomotion is explored. Conversely, other authors has put more emphasis on a more realistic description of the cell-substrate adhesion dynamics and the cell mechanics [53, 54, 66] via phase-field models, successfully reproducing the phenomenology of cell motility.

Other migration modes has also been studied. We may remark the studies performed in confined geometries, that provide an explanation of the observed sustained motion in narrow channels of mutant dendritic cells lacking integrin complexes, [67, 68]. On the other hand, in Refs. [69, 70], the authors has focused on the amoeboid-like migration, in which the nucleation and coordination of protrusions is still unclear.

2.2 Theoretical model of a lamellar fragment

Following Ref. [55] we describe a thin actin layer of actin cytoskeleton as an effective 2d single component, viscous fluid, bounded by a membrane with an arbitrary shape [3]. We assume that the relevant dynamics is sufficiently slow to neglect elastic effects. Actin is assumed to polymerize at the membrane, with a velocity v_p normal to it. Depolymerization is assumed to occur uniformly at a constant rate k_d in the fragment interior. Ignoring the dynamics of the actin polarization field as in Ref. [55], and assuming in addition that no myosin motors are present, the constitutive law reduces to that of an isotropic viscous fluid with viscosity η. Neglecting inertia this leads to $-\nabla P - \xi \mathbf{v} + \eta \Delta^2 \mathbf{v} = 0$, where P is the pressure and ξ is an effective friction coefficient. The velocity $\mathbf{v}$ can then be assumed to satisfy Darcy's law $\mathbf{v} = -d\nabla P$ either because friction forces with the solid substrate dominate over viscous forces [55], implying $d = 1/\xi$, or more generally, by considering the actin layer to be in a confined geometry, for instance in a Hele-Shaw cell with a gap b. In this case, the standard averaging over the narrow third dimension yields $d = \frac{b^2}{12\eta} + \frac{1}{2\xi}$ [67]. The problem is thus reduced to a free-boundary problem for the boundary $\partial\Omega(t)$ of a 2d domain $\Omega(t)$. The flow equations of polymerized actin are non-conventional in two ways, namely, the uniformly distributed sink that accounts for actin depolymerization in the

bulk, and the existence of a line source localized at the boundary that accounts for actin polymerization, that is,

$$\nabla \cdot \mathbf{v} = -k_d, \tag{2.1}$$

$$V_n = \mathbf{v} \cdot \hat{\mathbf{n}} + v_p, \tag{2.2}$$

where the normal velocity of the interface V_n differs from the normal velocity of the fluid by the constant v_p, assuming that actin polarization is normal to the membrane [55]. In addition to the kinematic condition (2.2) that defines the motion of the boundary as part of the solution, we must supply a boundary condition for the pressure field. The simplest choice is to assume a Young-Laplace pressure drop across the membrane [55]. Neglecting the viscosity of the outer fluid this reads $P|_{\partial\Omega} = \gamma\kappa$, where κ is the curvature (taken positive for a circle) and γ is an effective surface tension.

2.3 Conformal mapping approach

In this section, we derive explicitly the equation of motion for the boundary of a cell fragment using conformal mapping techniques. By analogy to viscous fingering and other Laplacain-growth problems, hereinafter we will refer to the boundary of the lamellar fragment as the 'interface'. For more details on the applications of conformal mapping techniques in two-dimensional free-boundary problems, the reader is referred to [56, 71].

The original model for a cell fragment described in the Sec. 2.2 was defined by

$$\xi \mathbf{v} = -\nabla P, \tag{2.3}$$

$$\nabla \cdot \mathbf{v} = -k_d. \tag{2.4}$$

Being $\xi = 1/d$, an effective friction coefficient.

Following Ref. [55], the viscosity of the outer medium was neglected with respect to the cell fragment viscosity ($\eta \sim 10^4$ Pa·s). The interface that defines the cell fragment contour ($\partial\Omega$) was considered stress-free, and it was assumed to be satisfied the Laplace-law ($P|_{\partial\Omega} = \gamma\kappa$). The temporal evolution of the cell fragment interface is encoded in the expression $V_n = \mathbf{v} \cdot \hat{n} + v_p|_{\partial\Omega}$, being v_p the actin polymerization velocity and k_d the rate of actin depolymerization. Formally, this physical model belongs to the family of Laplacian growth problems.

Let us define the transformation $\mathbf{v} = \mathbf{v}' - k_d\mathbf{r}/2$ and $P = P' + \xi k_d|\mathbf{r}|^2/4$, where $\mathbf{r}$ is the position vector. In terms of the new fields $(\mathbf{v}', P')$, Eqs. (2.3-2.4) reduce

to the equations of a Newtonian incompressible fluid in a Hele-Shaw cell.

$$\xi \mathbf{v}' = -\nabla P', \tag{2.5}$$

$$\nabla \cdot \mathbf{v}' = 0. \tag{2.6}$$

Through this transformation, it becomes clearer the existence of two harmonic fields, P' and the stream function ψ', which are coupled by the relations $\xi \partial_x \psi' = \partial_y P'$ and $-\xi \partial_y \psi' = \partial_x P'$. In other words, $-P'/\xi$ and ψ' are harmonic conjugates. The stress-free boundary condition and the kinematic equation of the interface are also affected by the latter transformation

$$P'|_{\partial\Omega} = \gamma\kappa - \frac{\xi k_d}{4}|\mathbf{r}|^2|_{\partial\Omega}, \tag{2.7}$$

$$V_n = \mathbf{v}' \cdot \hat{\mathbf{n}} - \frac{k_d}{2}\mathbf{r} \cdot \hat{\mathbf{n}} + v_p|_{\partial\Omega}. \tag{2.8}$$

Notice that even though Eqs. (2.7-2.8) contain terms that depend explicitly on the cell fragment position in space, which would seem to break the translational invariance of the problem, the latter is not the case when all equations are taken into account.

Taking the natural set of units $k_d = 2v_p = \xi = 1$, the physical model is left with one control parameter $\beta \equiv k_d\gamma/\xi v_p^2$, which is a dimensionless surface tension.

Then, we define the complex velocity potential as $\Phi(z) = -P'(x,y)/\xi + i\psi(x,y)$, which for construction is an analytical function of $z = x+iy$. On the other hand, we define a complex analytic function $z = f_t(\omega)$, which maps conformally a reference domain defined by the unit disk in the ω-complex plane ($|\omega| \leq 1$), onto the physical domain Ω in the z-complex plane. In particular, $f_t(e^{is})$ establishes a one-to-one relation between the contour of the unit disk ($|\omega| = 1$) with the cell fragment contour $\partial\Omega$. In other words, $f_t(e^{is})$ will be our parametrization of the cell fragment contour. The subindex t emphasizes that $f_t(\omega)$ may vary over time due to the interface evolution. Combining both definitions, one concludes that $\Phi(f_t(\omega)) = \Phi(\omega)$ is an analytical function on the reference domain.

Before proceeding with the derivation, let us say a few words with respect to the conformal mapping $f_t(\omega)$. In general, it can be represented as an infinite series $f_t(\omega) = a(t) + \sum_{n=0}^{\infty} a_n(t)\omega^{n+1}$, where the coefficients $a_n(t)$ and $a(t)$ are complex functions, usually called normal amplitudes. For sufficiently small values of these amplitudes, these modes correspond to sinusoidal deformations of the unit circle, as defined for instance in Ref. [55]. In broad terms, all the normal amplitudes contain a piece of the information of the interface shape, except for the normal amplitude $a(t)$, which sets the position in the physical domain of the unit disk center in the reference domain. In this problem $a(t)$ plays a crucial role, as it will

become clearer below.

So, the real part of Φ on the unit circle can be expressed as

$$\mathrm{Re}\left[\Phi\left(e^{is}\right)\right] = -\left.\frac{P'}{\xi}\right|_{\partial\Omega} = \phi_0 + \sum_{n=1}^{\infty}\left(\phi_n e^{ins} + \phi_n^* e^{-ins}\right),$$

which can be extended throughout the whole unit disk as

$$\Phi(\omega) = \phi_0 + 2\sum_{n=1}^{\infty}\phi_n\omega^n. \tag{2.9}$$

The complex amplitudes ϕ_n are determined from Eq. (2.7). Even if it might seem non evident at first glance, (2.9) turns out to be a solution of Eqs. (2.5-2.7) for the appropriate values of ϕ_n. Alternatively, the stream function on the unit circle could be written as

$$\psi'|_{\partial\Omega} = \mathcal{H}_s\left[-\left.\frac{P'}{\xi}\right|_{\partial\Omega}\right],$$

where $\mathcal{H}_s$ is the Hilbert transform which is defined as

$$\mathcal{H}_s[g] = \frac{1}{2\pi}P\int_0^{2\pi} g(s')\cot\left(s-s'\right)ds'. \tag{2.10}$$

Finally, the last step would be to express the stress-free boundary condition (2.7) and the cell fragment interface kinematic equation (2.8) in terms of the conformal mapping $f_t(e^{is})$. As an example, we compute explicitly the term $-k_d\hat{\mathbf{n}}\cdot\mathbf{r}/2$

$$\begin{aligned}
\hat{\mathbf{n}} &= \frac{-i\partial_s f}{|\partial_s f|},\\
\mathbf{r} &= f,\\
-\frac{k_d}{2}\mathbf{r}\cdot\hat{\mathbf{n}} &= -\frac{k_d}{2}\frac{\mathrm{Im}[f^*\partial_s f]}{|\partial_s f|},
\end{aligned} \tag{2.11}$$

where the asterisk denotes the complex conjugate. Notice that in the left-hand side we use vector notation for $\mathbf{r}$ and $\hat{\mathbf{n}}$ while in the right-hand side we use complex variable notation for vectors. We will keep this abuse of language in some cases for clarity. Similarly

$$P'|_{\partial\Omega} = \gamma\kappa[f] - \frac{\xi k_d}{4}|f|^2, \tag{2.12}$$

$$\mathbf{v}\cdot\hat{\mathbf{n}}|_{\partial\Omega} = -\left(\hat{\mathbf{t}}\cdot\nabla\psi'\right)|_{\partial\Omega} = \frac{\partial_s\mathcal{H}_s\left[\frac{\xi k_d}{4}|f|^2 - \gamma\kappa\right]}{|\partial_s f|}, \tag{2.13}$$

$$V_n = \frac{\mathrm{Im}[\partial_s f\partial_t f^*]}{|\partial_s f|}. \tag{2.14}$$

Where $\kappa[f] = \mathrm{Im}\,[\partial_s^2 f/(\partial_s f|\partial_s f|)]$ is the mean curvature in complex notation and $\hat{\mathbf{t}}$ stands for the unitary tangent vector at $\partial\Omega$.

After substituting the above equations into Eq. (2.8), we obtain

$$\mathrm{Im}[\partial_s f \partial_t f^*] = \partial_s \mathcal{H}_s \left[\tfrac{k_d}{4}|f|^2 - \tfrac{\gamma}{\xi}\kappa[f]\right] + v_p|\partial_s f| - \tfrac{k_d}{2}\mathrm{Im}[f^*\partial_s f]. \tag{2.15}$$

It is important to remark that the latter equation is invariant under the next transformations: a translation c in space ($f \to f + c$), a global rotation of angle θ ($f \to fe^{i\theta}$) and ($f(e^{is}) \to f(e^{i(s+s_0(t))})$) (discussed in Section 2.4.3). The latter transformation is associated with the arbitrariness in setting the angle origin $s_0(t)$ in the unit circle of the reference domain.

2.4 Numerical framework

In this section, we provide a detailed explanation of the main steps followed to construct the numerical approach used along this thesis to integrate the interfacial dynamics of the cell fragment model. The objective is to transform the evolution equation for the conformal mapping into an infinite set of ODEs for the normal amplitudes.

The starting point is the equation derived in Section 2.3,

$$\mathrm{Im}[\partial_s f \partial_t f^*] = \partial_s \mathcal{H}_s \left[\frac{k_d}{4}|f|^2 - \frac{\gamma}{\xi}\kappa[f]\right] + v_p|\partial_s f| - \frac{k_d}{2}\,\mathrm{Im}[f^*\partial_s f]. \tag{2.16}$$

For simplicity of the notation, in this section we will relabel the normal amplitudes using the definition

$$f_t(e^{is}) = a(t) + \sum_{n=1}^{\infty} a_n(t)e^{ins} \tag{2.17}$$

The conformal mapping has then two separated parts, one that contains all the geometrical information on the fragment shape, $\sum_{n=1}^{\infty} a_n(t)e^{ins}$, and the term $a(t)$ which defines its position in space. It is worth stressing that the original model from Ref. [55] has translational invariance and therefore, right-hand side of Eq. (2.16), which depends on the shape of the interface, should be independent of $a(t)$. Although not obvious at first sight, it can be explicitly shown that all explicit dependence on $a(t)$ in the right-hand side of Eq. (2.16) is exactly cancelled.

In order to transform Eq. (2.16) into an infinite set of ODE's for the normal amplitudes, first we define the mean curvature as $\kappa[f] \equiv c_0(t) + c_0^*(t) + \sum_{n=1}^{\infty}\{c_n(t)e^{ins} + c_n^*(t)e^{-ins}\}$. The coefficients $c_k(t)$ are usually complicated functions of the normal amplitudes of the conformal mapping $f_t(e^{is})$ (i.e the mean

curvature depends only on the shape of the interface). Then, introducing the formal expressions of the conformal mapping and the mean curvature into Eq. (2.16), each term becomes

$$\begin{aligned}
\mathrm{Im}[\partial_s f \partial_t f^*] &= \frac{1}{2}\sum_{n=1}^{\infty} n\left(a_n \dot{a}_n^* + a_n^* \dot{a}_n\right) \\
&+ \frac{1}{2}\sum_{l=1}^{\infty}\left\{\sum_{n=l+1}^{\infty}\left(n a_n \dot{a}_{n-l}^* + (n-l) a_{n-l}^* \dot{a}_n\right) e^{ils} + cc\right\} \\
&+ \frac{1}{2}\sum_{l=1}^{\infty}\left\{l a_l \dot{a}^* e^{ils} + cc\right\}, \\
\partial_s \mathcal{H}_s\left[\frac{k_d}{4}|f|^2\right] - \frac{k_d}{2}\mathrm{Im}\left[f^* \partial_s f\right] &= -\frac{k_d}{2}\sum_{n=1}^{\infty} n a_n a_n^* \\
&- \frac{k_d}{2}\sum_{l=1}^{\infty}\left\{\sum_{n=l+1}^{\infty}(n-l) a_n a_{n-l}^* e^{ils} + cc\right\}, \\
\partial_s \mathcal{H}_s\left[-\frac{\gamma}{\xi}\kappa[f]\right] &= -\frac{\gamma}{\xi}\sum_{l=1}^{\infty}\left\{l c_l e^{ils} + cc\right\},
\end{aligned}$$

where cc denotes the complex conjugate of the terms inside the curly brackets. For the previous derivation it is necessary to know a useful property of the Hilbert Transform $\mathcal{H}_s$:

$$\mathcal{H}_s\left[F_0 + F_0^* + \sum_{n=1}^{\infty} F_n e^{ins} + F_n^* e^{-ins}\right] = F_0 - F_0^* + \sum_{n=0}^{\infty} F_n e^{ins} - F_n^* e^{-ins}.$$

being $F = 2F_0(t) + 2\sum_{n=1}^{\infty} F_n(t) e^{ins}$ an analytic function. Due to this property one could write $F = Re[F] + i\mathcal{H}_s[Re[F]]$, which introduces an equivalent definition of the Hilbert Transform.

The only term missing from Eq. (2.16) is $v_p|\partial_s f|$. In order to express it in terms of the normal amplitudes of the conformal mapping $f_t(e^{is})$, we will define yet another set of coefficients as

$$-ie^{-is}\partial_s f = \left(\sum_{n=0}^{\infty} b_n(t) e^{ins}\right)^2, \tag{2.18}$$

where in general the $b_k(t)$'s are complex functions of time, which are related to the normal amplitudes of the conformal mapping $f_t(e^{is})$ by Eq. (2.18), (i.e. $a_{n+1}(t) = \sum_{m=0}^{n} \frac{b_m(t) b_{n-m}(t)}{n+1}$ for $n \geq 0$). Given the normal amplitudes $a_k(t)$'s, there is a unique choice of $b_k(t)$'s that satisfies the previous relations. As an example, if both are real $b_0(t) = \sqrt{a_1(t)}$.

Therefore, in terms of these new coefficients $v_p|\partial_s f|$ takes the simple form:

$$v_p|\partial_s f| \;=\; v_p\left\{\frac{1}{2}\sum_{n=0}^{\infty} b_n b_n^* + \sum_{l=1}^{\infty}\sum_{n=l}^{\infty} b_n b_{n-l}^* e^{ils} + cc\right\}.$$

The same procedure was followed at the beginning when we expressed the mean curvature in terms of the complex coefficients $c_k(t)$'s. Although in this case, the relations between these coefficients and the normal amplitudes of the conformal mapping $f_t(e^{is})$ are established by the less trivial equality

$$\kappa(s) = \frac{\mathrm{Im}[\partial_{ss} f \partial_s f^*]}{|\partial_s f|^3}. \tag{2.19}$$

The coefficients $c_k(t)$'s can be computed numerically for instance by using a FFT algorithm on the right-hand side of Eq. (2.19).

In summary, Eq. (2.16) properly normalized in units of $k_d = 2v_p = \xi = 1$ is fully equivalent to

$$\sum_{n=1}^{\infty} n a_n \dot{a}_n^* + n a_n^*(\dot{a}_n + a_n) \;=\; \sum_{n=0}^{\infty} b_n b_n^* \tag{2.20}$$

$$l a_l \dot{a}^* + 2\beta l c_l + \sum_{n=l+1}^{\infty} n a_n \dot{a}_{n-l}^* + (n-l) a_{n-l}^*(\dot{a}_n + a_n) \;=\; \sum_{n=l}^{\infty} b_n b_{n-l}^* \tag{2.21}$$

where l runs over all the positive integers. Being $\beta = k_d\gamma/\xi v_p^2$ the dimensionless surface tension.

As a trivial exact solution of the interface dynamics described by Eqs. (2.20-2.21), we can re-derive the solution of a circular interface with varying radius $R(t)$. These shapes could be parametrized by a conformal mapping whose normal modes are $a(t) = const$, $a_1(t) = R(t)$ and $a_k(t) = 0$ for $k > 0$. On the other hand, the coefficients $b_k(t)$'s that satisfy Eq. (2.18) are $b_0(t) = \sqrt{R(t)}$ and $b_k = 0$ for $k > 0$ and the same for the mean curvature yields to $c_0(t) = 1/R(t)$ and $c_k(t) = 0$ for $k > 0$. If one substitutes these expressions into Eqs. (2.20-2.21), one obtains that $\dot{R} = -\frac{k_d}{2}R + v_p$, which states that any initially circular cell fragment approaches exponentially the circular shape with a radius $R_0 = 2v_p/k_d$. Note that this result is valid for arbitrary large deviations of the initial radius from the stationary one.

2.4.1 Numerical integration of the interface dynamics

In this section, we will expose the main steps followed to construct a numerical method that allows us to integrate the interfacial evolution of our free-boundary problem.

We truncate the Fourier series involving $b_k(t)$'s coefficients in Eq. (2.18) (right-hand side) at a given order N, which is left as one of the program inputs i.e. $-ie^{-is}\partial_s f \approx \left(\sum_{n=0}^{N} b_n(t)e^{ins}\right)^2$. The conformal mapping is chosen to be truncated at the order $2N+1$ in the Fourier expansion, i.e $f \approx a(t) + \sum_{n=1}^{2N+1} a_n(t)e^{ins}$, and similarly for the Fourier expansion of the mean curvature although the truncation in that case is $3N+1$. Then, given the set of b_k for $0 < k \leq N$ at a certain instant of time, the coefficients of the truncated conformal mapping and mean curvature are determined by solving the linear system of equations originated from Eq. (2.18) and Eq. (2.19), respectively. Afterwards, the program solves the dynamical Eqs. (2.20-2.21) using either an explicit or an implicit Euler method with variable time step, which returns the values of the $b_k(t)$'s coefficients at the next time point. This scheme can be applied indistinctly to real or complex amplitudes.

The number of operations per iteration scales as $\mathcal{O}(N^2)$. Typically, temporal evolutions of the interface involve in our cases values of $N \sim 20$. However, if the coefficients of the truncated mean curvature Fourier expansion are computed using an FFT algorithm, N can be increased to ~ 30 within similar computation times.

2.4.2 Continuation methods for steady motile solutions

In this section we present the procedure followed to compute the steady cell fragment shape numerically, and the continuation method used over the single dimensionless parameter of the present physical model.

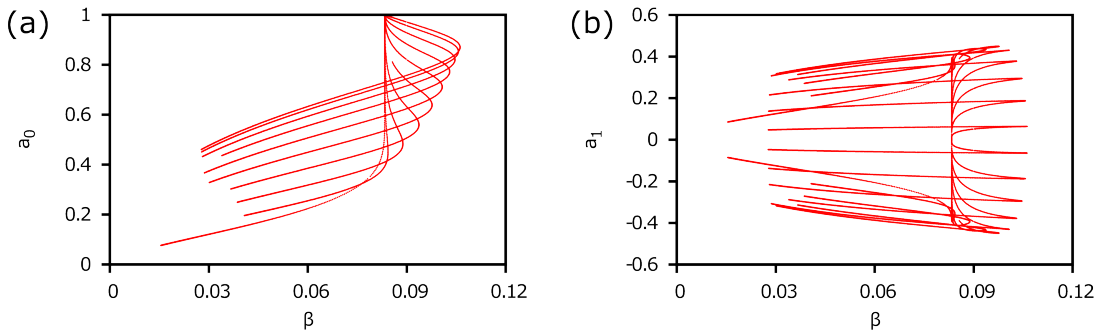

Figure 2.3: Each branch correspond to an steady solution parametrized by a truncated conformal mapping $f = a(t) + \sum_{n=0}^{2N} a_n e^{i(n+1)s}$. (a) The normal mode a_0 of several steady shapes versus the dimensionless surface tension β. (b) The normal mode a_1 of the same steady shapes as in (a) versus the dimensionless surface tension β. The values are plotted in units of $2v_p = k_d = \xi = 1$.

We have computed the steady solutions of the dynamical system explained in

Section 2.4.1 by means of a Newton-like method over a grid of initial conditions close to the circular steady interface. The truncation order N is one of the main inputs. On each steady solution, we apply a continuation method on the single free-parameter left in the physical model β. Examples of the bifurcation diagram are shown in Fig. (2.3). To elucidate some of the most delicate issues of convergence, in some cases it has been necessary to use extremely high arithmetic accuracy, up to 64 digits. We have implemented this accuracy using the software package **QD** (`http://crd-legacy.lbl.gov/~dhbailey/mpdist/`).

The number of operations per iteration scales as $\mathcal{O}(N^2)$. Our typical truncation values to obtain steady shapes are of the order of $N \sim 100$.

Convergence as $N \to \infty$ of steady solutions as a function of β

The next Figure (2.4) shows the bifurcation diagrams with respect to the area (left column) and the velocity (middle column) for two different steady motile solutions, in which N varies from 20 to 70.

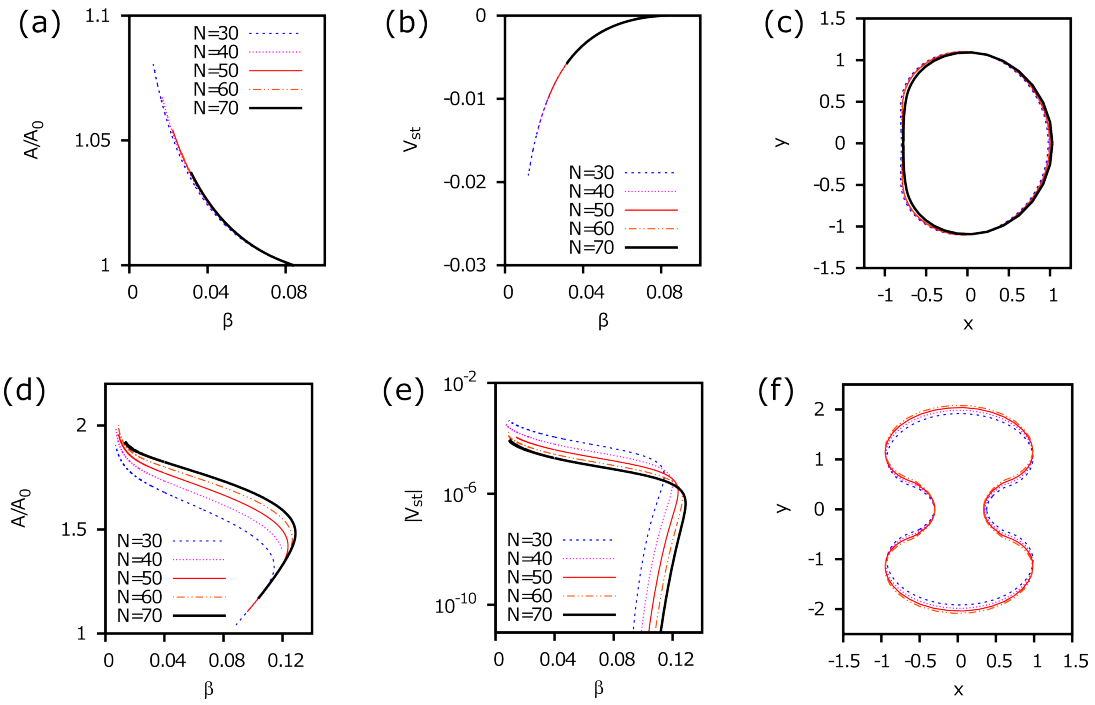

Figure 2.4: Analysis of the convergence of a pair of steady motile solutions with N, (a,d) Area normalized by the steady circular cell fragment's area vs the dimensionless surface tension (β). (b,e) Propagation velocity vs the dimensionless surface tension. (c,f) Motile steady shape at a fixed value of $\beta = 0.04$. The color-code in (c,f) is the same as in (a,d) or (b,e), respectively. The values are plotted in units of $2v_p = k_d = \xi = 1$.

Convergence as $N \to \infty$ of the geometrical properties of a steady shape at a fixed value of β

In Figure (2.5), it is shown the dependency of different magnitudes related with a chosen steady motile solution in terms of the order of truncation N. One can observe a distinction between the convergence at large values of N of the intrinsic geometrical properties from the steady shape and the normal amplitudes of the conformal mapping. As it will be shown below, the stationary traveling velocity is proportional to the difference between the contour and the areal center of masses (Sec. 2.5.2). This analysis suggests that the geometrical properties converge faster than the normal amplitudes. In the case displayed in Fig. (2.5), it seems that the area or the velocity saturate at a value $N \sim 40$, although this threshold may vary from shape to shape. It is expected that convergence of the steady shapes originated at bifurcation points of the steady circular shape occurs at smaller values of the truncation order as the free parameter β approaches the critical value.

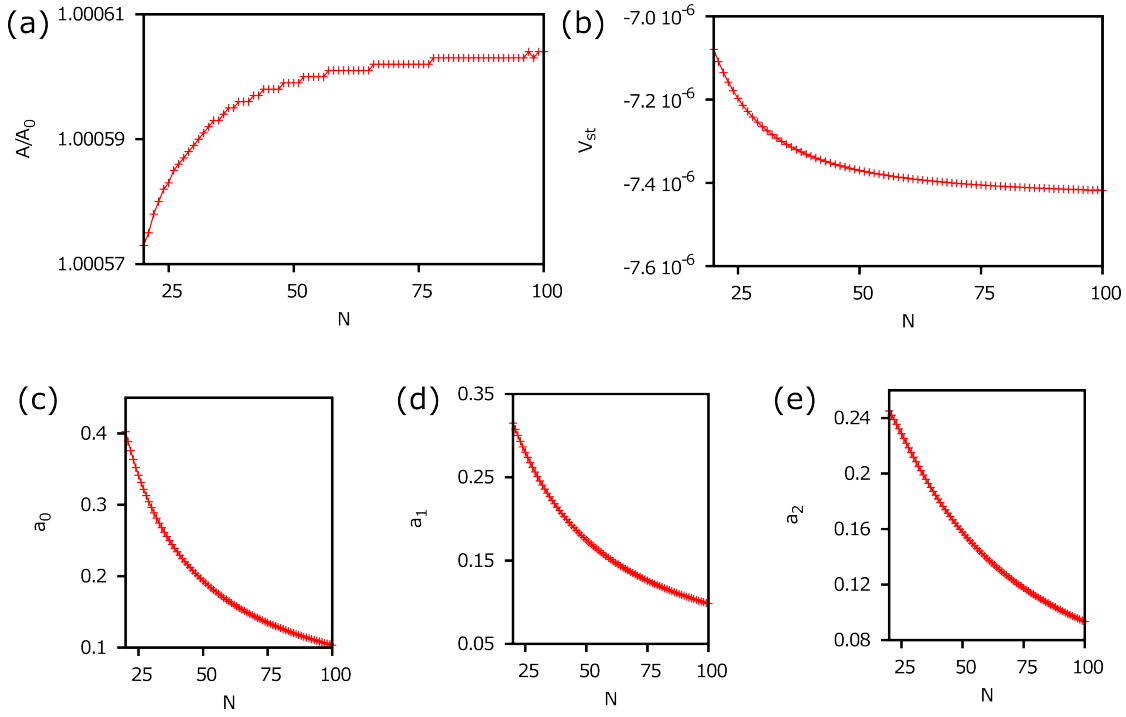

Figure 2.5: Analysis of the convergence of a single steady motile solution with N: (a) Area normalized by the steady circular cell fragment's area vs the truncation's order N and (b) propagation velocity vs the truncation's order N, for an steady motile solution at a value of $\beta = 0.082$. (c-e) correspond to the zeroth, first and second normal modes of the conformal mapping $f \approx a(t) + \sum_{n=0}^{2N} a_n e^{i(n+1)s}$ parametrizing the same steady motile solution as in (a) and (b) at a value of $\beta = 0.082$ vs the truncation's order N, respectively. The values are plotted in units of $2v_p = k_d = \xi = 1$.

2.4.3 Conformal mapping gauge invariance

In this section we briefly discuss a gauge symmetry on the dynamical equation (2.15), which implies that there exists an infinite set of conformal mappings that parametrize the same physical interface, that is the same shape. Apart from trivial symmetries such as global rotational and translational symmetries, there is indeed a high degeneracy of the conformal approach. This is clearly illustrated by the fact that there exist a family of conformal mappings of the unit circle onto itself, the so-called Möbius transformations. As usual in physics, such degeneracy must be avoiding in practice by an adequate choice of gauge. Specifically, we will show that there is an arbitrariness at each instant of time on the choice of the coordinate origin of the conformal parametrization of the physical contour.

Let us define the conformal mappings $f(s,t) = a(t) + \sum_{n=0}^{\infty} a_n(t) e^{i(n+1)s}$ and $f_{s_0(t)} = f(s+s_0(t),t)$. Both mappings parametrize the same physical interface. At a fixed instant of time, the inverse image of every point on the physical contour differs a phase $s_0(t)$ between both maps. Remarkably, such a phase $s_0(t)$ may depend on time, meaning that at each instant of time, one has the freedom to choose the phase $s_0(t)$. Equivalently, the normal modes $a_n(t)$ are constrained by such symmetry. To see that this freedom is indeed available, it is sufficient to show that the left-hand side of Eq. (2.15) for both conformal mappings are the same.

$$\begin{aligned}
\mathrm{Im}[\partial_s f_{s_0(t)} \partial_t f^*_{s_0(t)}] &= \mathrm{Im}[\partial_s f_{s_0(t)} ((\dot{a}(t) + \sum_{n=0}^{\infty} \dot{a}_n(t) e^{i(n+1)(s+s_0(t))})^* + \partial_s f^*_{s_0(t)} \dot{s}_0(t))] \\
&= \mathrm{Im}[\partial_s f_{s_0(t)} (\dot{a}(t) + \sum_{n=0}^{\infty} \dot{a}_n(t) e^{i(n+1)(s+s_0(t))})^*].
\end{aligned}$$

In practice, this symmetry has been exploited in our construction of the numerical method to integrate the interfacial dynamics, by imposing that the amplitude of the expansion/compression normal mode, $a_0(t)$, is real for all time.

2.5 Exact results for motile lamellar fragments

2.5.1 Harmonic moment expansion

In this section we derive the dynamical equation for the so-called harmonic moments of the present physical model for a cell fragment. Other examples in which this formalism has been used in Laplacian free-boundary problems can be find in Refs. [71, 72]. This formalism is particularly useful to obtain global geometric information of the shape evolution.

The temporal evolution of the free interface can be described in terms of the temporal evolution of the harmonic moments. The complex m-th moment is defined as

$$M_k^A = \int_\Omega z^k da, \tag{2.22}$$

where $z = x + iy$, being x and y the cartesian coordinates in the physical domain and k is a positive integer. The moments are complex magnitudes associated with geometrical properties of the contour $\partial\Omega$. Their time evolutions, however, encode the dynamics according to the physical properties of the system. For instance the area is the zeroth moment and its temporal evolution is governed by a mass balance equation (see below). For the present case, it will be convenient to define analogous properties based on integrals over the boundary, rather than its interior. We thus define

$$M_k^L = \int_{\partial\Omega} z^k dl, \tag{2.23}$$

the integral of z^k along the contour $\partial\Omega$ of the domain Ω. M_k^L may be a complicate function of the moments M_k^A.

The temporal derivative of a moment satisfies

$$\frac{dM_k^A}{dt} = \int_{\partial\Omega} z^k V_n dl, \tag{2.24}$$

where V_n is the normal velocity of the interface, [71, 72]. Then, if we substitute V_n by $\mathbf{v}\cdot\hat{\mathbf{n}} + v_p$ into Eq. (2.24) and apply the divergence theorem in $2d$, we obtain

$$\int_{\partial\Omega} z^k V_n dl = v_p M_k^L + \int_\Omega \nabla\left(z^k \mathbf{v}\right) da. \tag{2.25}$$

The second term in the right hand side of Eq. (2.25), can be further simplified by exploiting the incompressibility condition, the analyticity of z^k and Eq. (2.3), giving rise to

$$\int_\Omega \nabla\left(z^k \mathbf{v}\right) da = -k_d M_k^A - \frac{1}{\xi}\int_\Omega \nabla\left(P\nabla z^k\right) da. \tag{2.26}$$

The second term of the right hand side of Eq. (2.26) can be transformed back into a contour integral by means of the divergence theorem and afterwards replacing the pressure field at the interface by the Laplace law, we obtain

$$-\frac{1}{\xi}\int_\Omega \nabla\left(P\nabla z^k\right) da = -\frac{\gamma}{\xi}\int_{\partial\Omega} \kappa\hat{n}\cdot\nabla z^k dl. \tag{2.27}$$

Finally, gathering all these results together, we get the following dynamical equa-

tion for the k-th moment:

$$\frac{dM_k^A}{dt} = v_p M_k^L - k_d M_k^A - \frac{\gamma}{\xi}\int_{\partial\Omega} \kappa \hat{n} \cdot \nabla z^k dl. \tag{2.28}$$

This infinite set of equations is an alternative formulation of the problem and thus it contains all the geometrical information, with different moments encoding different types of integral information of the interface shape.

2.5.2 Exact equation of motion: kinematics and geometry

As mentioned above, the zeroth areal moment is the total area. Similarly, M_0^L yields contour length, that is, the perimeter L. Therefore, the dynamical equation for the area can be written as

$$\frac{dA}{dt} = v_p L - k_d A. \tag{2.29}$$

The above equation expresses the mass balance, implying that the total area may vary as a result of the imbalance between the mass injected by the boundary (actin polymerization) and the mass lost at the distributed sink in the interior (constant bulk rate of actin depolymerization). On the other hand, note that the center of mass of the area is expressed as $R_A = M_1^A/M_0^A$, while the center of mass of the contour reads $R_L = M_1^L/M_0^L$. Remarkably, Eqs. (2.28) allow one to deduce an explicit equation for the instantaneous velocity of the center of mass R_A in terms of only geometrical properties of the interface's shape, which has the following expression

$$\frac{dR_A}{dt} = \frac{v_p L}{A}\left(R_L - R_A\right). \tag{2.30}$$

This is a very interesting result that relates geometry to kinematics with no explicit dependence on the parameter β. Eq. (2.30) is an exact result that establishes a simple relation between the instantaneous velocity of the center of mass and geometrical properties of the contour. In other words, given the shape of a cell fragment at a given time, we do know its instantaneous velocity. Furthermore, if we knew the evolution of the shape, we would be able to integrate the trajectory of the center of mass. It is worth stressing that the fact that $\dot{R}_A \neq 0$, does not mean that the fragment will necessary sustain motion, since a time variation of the center of mass may also reflect a transient deformation. However, it is interesting to note that with this result, the issue of knowing whether this set of equations contains steadily traveling solutions, a highly non-trivial and controversial question, is reduced to that of whether non-symmetrical stationary shapes exit, which is much simpler to answer. As long as the interface shape remains stationary, then Eq. (2.30) yields necessarily its traveling velocity V_{st}.

In order to know the complete time evolution one needs to include higher orders and then the problem is no longer solvable, not even with $\beta = 0$, in contrast to other examples of Laplacian growth for which the whole hierarchy can be solved for zero surface tension. It is also important to stress that the detailed evolution of the shape may be sensitive to details that have not been taken into account in our simplified model, as we will discuss later. However, our focus here is in understanding the minimal ingredients and mechanisms that produce and sustain motion through a morphological instability, and not to achieve a realistic description of the served morphologies in actual living systems. Other more elaborated models in the literature have been designed to yield more realistic shapes. As shown in Ref. [25], for instance, the steady migrating morphologies of keratocytes, can be classified with a finite set of geometrical quantities. The area and the aspect ratio are sufficient to capture 93% of the cell shape variations in motile keratocytes. As a matter of fact, in the same reference, there is one of the first attempts to construct with physical arguments, an explicit analytical expression of the propagation velocity in terms of the geometrical properties of the shape. Therefore, it would be worth to contrast as well the predictability of the latter exact expression for the instantaneous velocity of the centre of mass on this family of migrating shapes in keratocytes, Fig. (2.6).

Physical interpretation

Eq. (2.30) expresses a relation between the instantaneous velocity of the center of mass and geometrical properties of the physical domain enclosed by the interface. In order to have sustained motion, the shape must be such that the center of mass of the area, that is, the sink of matter uniformly distributed in the bulk, must be different from the center of mass of the contour, that is, the source of matter distributed along the boundary. Effectively, the system behaves as if there were a point source of matter at the center of mass of the contour and a point sink at the center of mass of the area, with a net flow of matter from one to the other. It is thus the existence of a dipolar structure what is associated to the possibility of motion.

To pursue this idea let us express the velocity of the center of mass into different ways. It can be shown that

$$\frac{dM_0^A}{dt} = \frac{d}{dt}\int_\Omega da = \int_\Omega (-k_d)da + \int_{\partial\Omega}(v_p)dl, \tag{2.31}$$

$$\frac{dM_1^A}{dt} = \frac{d}{dt}\int_\Omega z da = \int_\Omega z(-k_d)da + \int_{\partial\Omega} z(v_p)dl, \tag{2.32}$$

are fully equivalent to Eq. (2.28) for $k = 0, 1$. Making an electrostatic analogy,

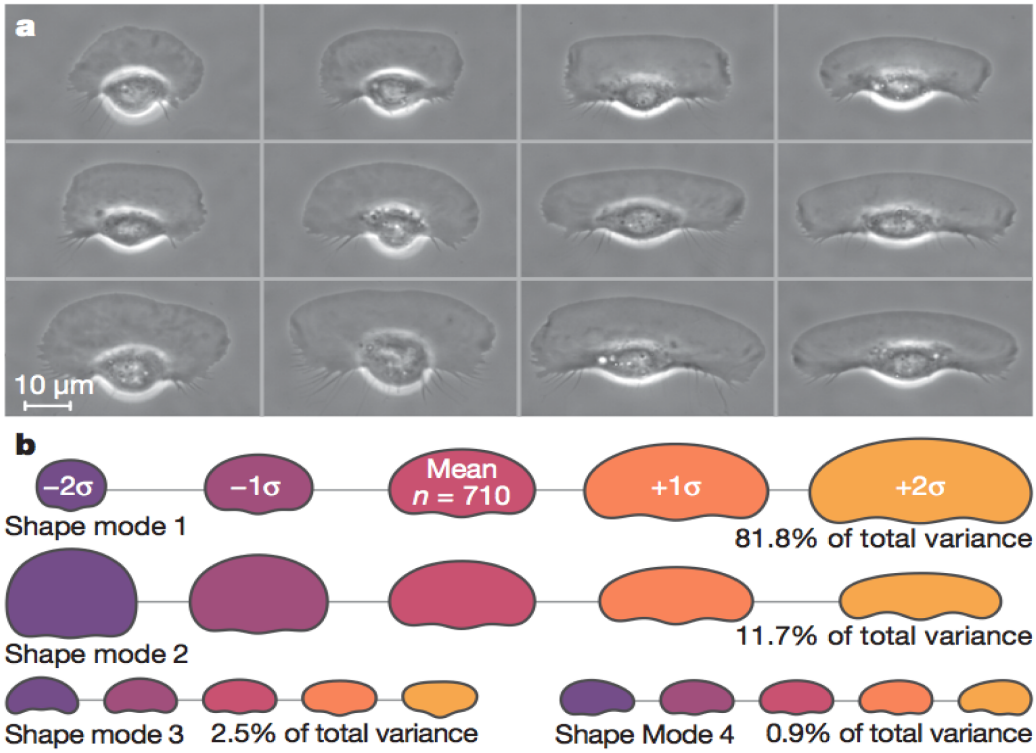

Figure 2.6: Keratocyte shapes are described by four primary shape modes. **a**, Phase-contrast images of different live keratocytes illustrate the natural shape variation in the population. **b**, The first four principal modes of keratocyte shape variation, as determined by principal components analysis of 710 aligned outlines of live keratocytes, are shown. These modes - cell area (shape mode 1), 'D' versus 'canoe' shape (shape mode 2), cell-body position (shape mode 3), and left-right asymmetry (shape mode 4) - are highly reproducible; subsequent modes seem to be noise. For each mode, the mean cell shape is shown alongside reconstructions of shapes one and two standard deviations away from the mean in each direction along the given mode. The variation accounted for by each mode is indicated. (Modes one and two are scaled as in **a**; modes three and four are 50% smaller.). This figure was extracted from Ref. [25]

the right-hand side of Eq. (2.31) could be interpreted as the total charge of a system with a surface charge density proportional to $-k_d$ in Ω and line charge density proportional to v_p at $\partial\Omega$. Equivalently, the right-hand side of Eq. (2.32) corresponds to the dipolar moment of the latter charge distribution. Therefore, at the steady state the dipolar moment of the distribution of sources/sinks of matter in the cell fragment sets speed and the direction of motion.

In Fig. (2.7), it is represented an actin filament immersed in a reservoir of actin monomers. Actin polymerization/depolymerization processes are thought to occur at the opposite ends of the filament. Therefore, both cases (a) and (b), have a finite dipolar distribution in the sources/sinks of matter. However in case (a) the actin filament is suspended in the medium, so the global momentum

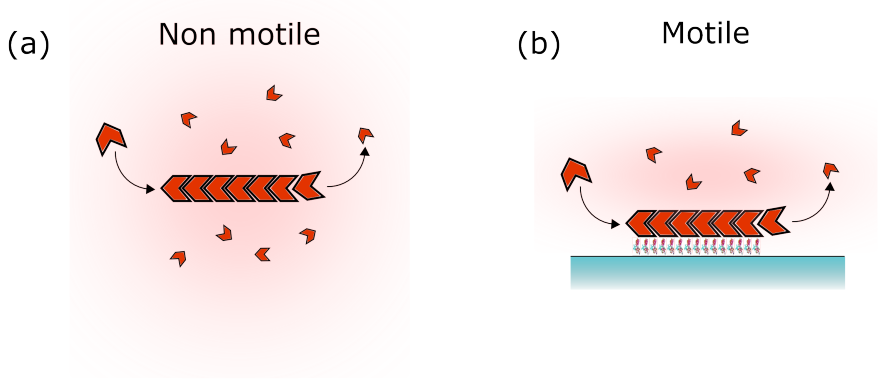

Figure 2.7: Schematic representation of a two-component system: actin monomers and actin filaments. (a) Suspended in an ideal solution and (b) on top of a substrate, at which actin filaments are weakly attached.

must be conserved and the reservoir moves in the opposite direction to the actin filament. Consequently, the filament in case (a) cannot propel. On the other hand, in case (b) the actin filament is weakly attached to a substrate, so an effective friction force is responsible for the exchange momentum, allowing it to propel. This simple example, highlights the fundamental role of passive friction forces in the present mechanism of cell locomotion.

It is interesting to emphasize that the cell fragment is propelling in over-damped conditions, and that in principle all forces are balanced. It may not be obvious, though, that each of the different external forces add up to zero separately. Indeed, it can be shown that the total friction force integrated in the whole domain vanishes exactly, that is, $\int_\Omega \xi \mathbf{v} da = 0$. Similarly, the total force produced by the capillary pressure due to the effective surface tension of the interface also vanishes, being $\int_{\partial\Omega} \gamma\kappa\hat{n}dl = 0$. Finally, if we define a protrusion force as proportional to $\int_{\partial\Omega} \xi v_p \hat{n} dl$, it also vanishes exactly.

2.5.3 General exact expression for center of mass velocity

The aim of this subsection is to briefly address the possible generalizations of the previous result and provide a phenomenological expression for the fragment velocity that is valid in a much more general sense. Several effects or physical ingredients were disregarded in the simple cell fragment model (2.3,2.4). This has helped us to elucidate the minimal mechanisms for spontaneous motility as a proof of principle, but the shapes and velocities arising from this minimal model

may not be realistic. Nevertheless, a similar framework can still be maintained in order to extrapolate our results to more realistic descriptions of the cell fragments, including for instance more general boundary conditions at the membrane, the effect of molecular motors, the presence of other external forces, the possibility of inhomogeneous values of the parameters k_d, v_p or γ, etc. In particular, Eq. (2.30) can be cast in a more general form and may become useful as a test to relate simple direct experimental observables to shape and velocity.

Let us consider the physical model defined by

$$\begin{aligned} \xi v_\alpha &= \partial_\beta \sigma^{tot}_{\alpha\beta} + f^v_\alpha \\ \partial_\beta v_\beta &= -k_d \\ \sigma^{tot}_{\alpha\beta}\hat{n}_\beta &= f^s_\alpha|_{\partial\Omega} \\ V_n &= v_n + v_p|_{\partial\Omega} \end{aligned}$$

where k_d and ξ are assumed to be constant for simplicity, but v_p is allowed to be heterogenous in space. The term $\mathbf{f}^v$ accounts for a general external force per unit area. The term $\mathbf{f}^s$ stands for a force per unit length at the cell membrane, produced for instance by the resistance of the external medium or the elasticity of the cell membrane. In this case, the generalization of the Laplace law takes the form $\mathbf{f}^s = -\gamma\kappa\hat{\mathbf{n}}$.

In this general case, and following analogous calculations to those described in Section 2.5.1, we can derive as well an exact expression for the instantaneous velocity of the centre of mass. At the steady state, it takes the form

$$V_{st} = \frac{\langle v_p z\rangle_L}{A} - R_A\frac{\langle v_p\rangle_L}{A} + \frac{\langle f^v\rangle_A}{\xi A} + \frac{\langle f^s\rangle_L}{\xi A}. \tag{2.33}$$

where 2d vectors (V_{st}, R_A, f^v, f^s) are written as complex numbers, as before. The bracket $\langle\ \rangle_L$ stands for the integral along the interface $\partial\Omega$, whereas $\langle\ \rangle_A$ stands for the integral throughout the inner domain Ω. Physically, the first two terms at the right-hand side of Eq. (2.33) have a meaning similar to the original minimal model. The third and forth terms on the contrary are averaged external mechanical forces. It is worth noticing, that $\sigma^{tot}_{\alpha\beta}$ has not been specified, a fact that highlights the generality of the latter expression for the steady velocity (V_{st}). In particular, the assumption of Darcy flow is not a requirement. The only strong restriction of the analysis is that the problem must be quasi-twodimensional.

Next we discuss a more explicit example where the use of the above expression can be more clearly illustrated. Note that in our description, the dynamics of the polarization field of the actin network has been fully decoupled from the contour dynamics. In reality, though, the transition to a motile state, the cytoskeleton

polarizes along the direction of migration. Such large-scale reorganization of the cytoskeleton is strongly regulated and obviously enhances de motility of cells, [23]. In addition, the distribution of myosin motors is heterogenous and concentrated at the rear of the cell, [24]. Still without involving the full dynamics of the polarization field and its coupling to the active stresses from molecular motors, we can use our result to relate the velocity to the actual stationary distribution of those fields. In particular we may incorporate a more general boundary condition that does not restrict the polarization field to be perpendicular to the membrane, taking the form $v_p \sim v_p^0(\mathbf{p}\cdot\hat{\mathbf{n}})$. Moreover, it can be shown that in the conditions of 2d confinement in a Hele-Shaw cell, the effect of molecular motors can be reduced to a simple body force of the form $\mathbf{f}^v = -\zeta\Delta\mu\mathbf{p}$, where $\mathbf{p}$ is the polarization field describing the local alignment of actin filaments, and $\zeta\Delta\mu$ is a phenomenological parameter proportional to the active stresses produced by these molecular motors [67]. In this case the active stresses are contractile and therefore ζ is negative. Finally we take the Laplace law at the interface in the form $\mathbf{f}^s = -\gamma\kappa\hat{\mathbf{n}}$. Under these hypothesis Eq. (2.33) becomes

$$V_{st} = v_p\left(\frac{\langle z\,(\mathbf{p}\cdot\hat{\mathbf{n}})\rangle_L}{A} - R_A\frac{\langle \mathbf{p}\cdot\hat{\mathbf{n}}\rangle_L}{A}\right) - \frac{\zeta\Delta\mu\langle\mathbf{p}\rangle_A}{\xi A}.$$

Remarkably, Eq. (2.33) can be evaluated without defining additional transport equations for the field $\mathbf{p}$, just using empirical information on the corresponding observables, for instance measuring the polarization field and the possible inhomogeneities of motor concentration. As an illustrative exercise, let us assume a semicircular fragment, with an actin network aligned radially with respect to the circle center, as shown in Fig. (2.8). Note that the alignment is parallel to the boundary in the straight part, a situation that is reminiscent to the actin cables sometimes observed at the rear of propelling cells. Assuming a uniform distribution of molecular motors, one can now derive an expression for the steady of the form

$$V_{st} \;=\; \frac{4}{3\pi}v_p - \frac{2}{\pi}\frac{\zeta\Delta\mu}{\xi}.$$

Note that even in the absence of molecular motors, and thanks to the strong polarization, the velocity is of order one with respect to v_p. This is in contrast to the velocities that will be obtained in the coming sections for cases where the polarization is forced to remain perpendicular to the membrane. Notice also that, since $\zeta < 0$, the effect of the active stresses due to myosin motors enhances significantly the velocity.

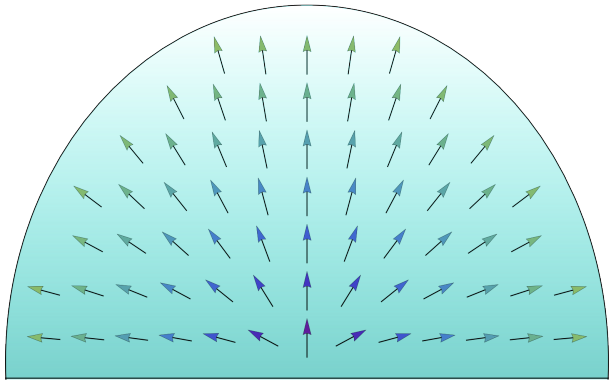

Figure 2.8: Schematic crescent-like cell fragment. The arrows stand for the local alignment of the actin network.

2.6 Nonlinear morphological instabilities

2.6.1 Center-manifold reduction and nonlinear analysis

As mentioned in the introduction to this chapter, our main objective in this problem is to work out the connection between the morphological instability reported by [55] and the spontaneous transition to motile states. The analysis of [55] was linear and therefore, by symmetry arguments it could not conclude on whether the instability could lead to motion, since the only mode that singles out a direction in space is the displacement mode (mode with $n = 1$ in [55] and in the following discussion). Since this mode is exactly marginal because of translational invariance, the mechanism by which a spontaneous symmetry breaking can lead to motion must necessarily involve the coupling between different modes, that is, it must be inherently nonlinear. The purpose of this section is to pursue this analysis into the nonlinear regime to prove that the rest of the center of mass is nonlinearly unstable, and that therefore, without invoking any other mechanisms that could coexist, circular fragments are generically motile. To prove the nonlinear instability of the rest state we will use center-manifold reduction techniques. These will in turn unveil a complex bifurcation scenario that we will explore in a combination of analytical and high-precision numerical work. In Appendix 7.1 we review the basic concepts of center-manifold reduction in some detail and in its most general form since they play a central role in our systematic weakly nonlinear analysis, and because the problem at hand presents some mathematical subtleties that require a careful treatment.

To implement a systematic weakly-nonlinear expansion of the dynamics defined by Eq. (2.15) in a neighborhood of the circular resting shape, we will first derive a convenient formulation of an equivalent infinite-dimensional dynamical system based on conformal mapping techniques. Next we will perform the center-manifold

reduction of it and work out in detail the bifurcation scenario leading to the different types of instabilities present in this problem. Finally we will discuss the main analytical and numerical results, and their implications for the problem at hand.

Conformal mapping gauge fixing

In this section, we discuss an alternative way to express the temporal evolution of the physical interface, which it is more convenient to perform the weakly nonlinear analysis. This corresponds to exploit the gauge invariance of the problem by choosing a convenient gauge. The arbitrariness that we will remove is that associated to the tangential component of the interface velocity, which is physically meaningless. Indeed, from the viewpoint of the free-boundary problem, only the geometry of the interface (i.e. its shape) is relevant, and the dynamics of such curve is unambiguously defined if only the normal component of the velocity at each point is fixed. Different tangential components are then related to reparametrizations of the curve.

We may write the tangential velocity at the interface V_t such that the next equality is satisfied

$$\partial_t f = -i\frac{\partial_s f}{|\partial_s f|}V_n + \frac{\partial_s f}{|\partial_s f|}V_t. \tag{2.34}$$

In general, $V_n = n_0 + \sum_{m=1}^{\infty} n_m e^{ims} + n_m^* e^{-ims}$ and $V_t = t_0 + \sum_{m=1}^{\infty} t_m e^{ims} + t_m^* e^{-ims}$ are real functions. Eq. (2.34) could then be expressed as

$$\begin{aligned}\partial_t f &= \sum_{l=1}^{\infty} l a_l c_0 e^{ils} + \sum_{l=2}^{\infty}\left(\sum_{m=1}^{l-1} m a_m c_{l-m}\right) e^{ils} + \sum_{m=1}^{\infty} m a_m d_m \\ &+ \sum_{l=1}^{\infty}\left(\sum_{m=l+1}^{\infty} m a_m d_{m-l}\right) e^{ils} + \left(\sum_{m=l+1}^{\infty}(m-l) a_{m-l} d_m\right) e^{-ils},\end{aligned}$$

being $c_m = n_m + i t_m$ and $d_m = n_m^* + i t_m^*$. Imposing the analyticity of the conformal mapping implies then that $d_m = 0$ for $m > 1$. On the other hand, $\mathrm{Im}[c_0]$ is arbitrary and we choose it to be zero. This is related to the phase invariance of the conformal mapping discussed in Section 2.4.3. Finally, it only remains to determine the (time-dependent) complex quantity d_1. In Ref. [56], the authors had imposed $d_1 = 0$. The criterion followed in this thesis is $d_1 = n_1^*$. Therefore, the starting point for our weakly nonlinear analysis will be the dynamical system

defined by

$$\begin{aligned}\partial_t f &= \sum_{l=1}^{\infty} l a_l n_0 e^{ils} + \sum_{l=2}^{\infty}\left((l-1)a_{l-1}n_1 + \sum_{m=1}^{l-2} 2m a_m n_{l-m}\right)e^{ils} \\ &+ a_1 \cdot n_1^* + \sum_{l=1}^{\infty}(l+1)a_{l+1}n_1^* e^{ils}, \end{aligned} \tag{2.35}$$

where one should keep in mind that the coefficients n_k depend on the amplitudes of the conformal mapping.

Center-manifold reduction in the cell fragment model

In this section we describe the weakly nonlinear analysis applied on the present minimal problem of cell fragments. We address the reader to Appendix 7.1 for further details and clarification on the use of the method.

The modeled cell fragments exhibit a steady circular shape, with a radius that is fixed by the balance between the polymerization and depolymerization processes $R_0 = 2v_p/k_d$. In terms of the conformal mapping, this shape can be described as $f = R_0 e^{is}$. The linear stability analysis of sinusoidal perturbations on the steady circular shape was carried out in Ref. [55], showing that an n-fold sinusoidal perturbation of small amplitude evolves in time exponentially with a characteristic growth rate

$$\lambda(n)k_d^{-1} = \frac{1}{2}(n-1) - \beta n(n^2-1), \tag{2.36}$$

being $\beta = \gamma/(\xi k_d R_0^3)$ the dimensionless surface tension of the cell membrane. Here we label the modes as in Ref. [55], with $n = 0$ being the expansion mode, $n = 1$ the displacement mode, $n = 2$ the eliptical mode and $n > 3$ the n-fold petal mode. Accordingly, the growth rate of all the normal modes, except for the zeroth ($\lambda(0) = -k_d/2$) and the first ($\lambda(1) = 0$), changes sign at a critical value of the dimensionless surface tension specific for each node. As discussed in Ref. [55] this instability in analogue to the viscous-fingering instability in Hele-Shaw cells, and is controlled by the interplay of the friction forces produced by the active inwards flow of actin and the capillary forces at the membrane. A generic perturbation on the steady circular shape can be parametrized by the conformal mapping

$$f = R_0 e^{is} + a(t) + \sum_{n=0}^{\infty} a_n(t) e^{i(n+1)s}, \tag{2.37}$$

being $a(t)$ and $a_n(t)$ complex functions of time. The amplitude a_n are also called

n-th normal mode. When $|a_n| \ll 1$ the deformation corresponds to a sinusoidal perturbation of small amplitude. The linearized dynamics of the normal modes are given by $\dot{a}_n = \lambda(n)a_n + \mathcal{O}(\epsilon^2)$, where we formally assume that $a_n \sim \mathcal{O}(\epsilon)$, being $\epsilon \ll 1$ a dimensionless book-keeping parameter that keeps track of the order of the nonlinearities. It is worth recalling at this point that a linear perturbation of the amplitude a_1 is equivalent to a displacement of the center of the circular shape without any shape change. Since the problem is translationally invariant, this mode must be marginal (i.e. $\lambda(1) = 0$). This is in contrast to the problem of a viscous fluid in a rotating Hele-Shaw cell, which has remarkable similarities with our problem here, but is not translationally invariant, since the centrifugal force drives the displacement mode exponentially away from the center of rotation. Therefore, as discussed above, the displacement mode will have to be coupled to other modes at nonlinear level if the present model is to give rise to net and sustained motion of the cell fragment.

Introducing the conformal mapping as expressed in Eq. (2.37) into Eq. (2.35) one would derive a dynamical system whose variables are the normal amplitudes $a_n(t)$ and $a(t)$, that has a fixed point at the origin, with the parameter β controlling its stability. The corresponding infinite set of ODE's must take the generic form

$$\dot{a} = N(a_0, a_1, ...), \tag{2.38}$$

$$\dot{a}_m = \lambda(m)a_m + N_m(a_0, a_1, ...). \tag{2.39}$$

for $m \geq 0$, where N and N_m are nonlinear functions of their arguments, and take the form of a power expansions. Note that the fact that there is no net center of mass velocity at linear level imposes that no linear term is present in the equation for $a(t)$. Note also that the linear part of the dynamics for all the $m \geq 0$ modes is diagonal in these amplitudes.

Before proceeding, let us briefly digress to tackle the role $a(t)$ in the latter dynamical system. As was discussed before, the coefficient $a(t)$ sets the position of the physical interface in space. Formally, it specifies the image in physical space of the origin of the circle in the reference domain. The translational invariance of the physical model is reflected in the fact that the temporal derivatives do not depend on $a(t)$. This implies that the dynamics of the $m \geq 0$ that define the interface shape, are decoupled from $a(t)$. Similarly, the trajectory of the center of mass in space, encoded in $a(t)$ can only depend on the evolution of the shape of the interface, encoded in the $a_m(t)$ for $m \geq 0$. This is consistent with the exact equation of the center of mass derived in the previous section. Consequently, one may disregard the equation for $a(t)$ to study and focus only on the a_m modes that define the shape evolution, and obtain the velocity as a function of them. Specifically, if a stationary shape is parametrized by the

conformal mapping $f = a(t) + \sum_{n=0}^{\infty} a_n^{st} e^{i(n+1)s}$, then $\dot{a} = N(a_0^{st}, a_1^{st}, ...)$ becomes its traveling velocity. Finally, note that at linear order $a(t)$ coincides with $a_1(t)$. However both amplitudes have a different morphological information for the full nonlinear problem.

Coming back to the central thread, for any value of the dimensionless surface tension, mass balance combined with incompressibility impose the zeroth normal mode to be stable with a fixed decay rate. The displacement mode is always marginal because of translational invariance, so any center manifold analysis will necessarily include this mode. On the other hand, each of the n-th normal mode for $n \geq 2$ becomes marginal at a specific value of $\beta = \beta_n \equiv 1/(2n(n+1))$, when $\lambda(n, \beta_n) = 0$. It is convenient to define yet another variable $g_m \equiv \beta - \beta_m$, which measures the distance to each of these bifurcation points $\beta = \beta_m$. Then, the normal modes can be grouped in three categories depending on their stability at linear order: stable, unstable or marginal. At values of β close to the critical value β_m, one would have to deal with two marginal modes, the modes $a_1(t)$ and another one nearly marginal $a_m(t)$, so the center manifold will have 2 (complex) modes. For values of β different from the critical values β_n for $n > 1$, only the first mode $a_1(t)$ will be marginal, and so the center manifold would have 1 degree of freedom. Therefore, there are two qualitatively different types of bifurcations in the system.

As described in detail in the Appendix 7.1, the center-manifold reduction theorem tells us that the inherently nonlinear structure of the dynamical system, including all the bifurcation structure, can be projected in a manifold with the dimension of the number of marginal (central) modes. Let us consider a dynamical system of the generic form

$$\dot{a}_c = L_c a_c + N_c(a_c, a_s, a_u), \tag{2.40}$$

$$\dot{a}_s = L_s a_s + N_s(a_c, a_s, a_u), \tag{2.41}$$

$$\dot{a}_u = L_u a_u + N_u(a_c, a_s, a_u), \tag{2.42}$$

where a_s denotes the set of stable modes (which in our case will typically be infinite), a_u the set of unstable modes (which in our case will be a finite number), and a_c denotes the set of central (marginal) modes (which in our case will be a very small number), and where we have explicitly split the linearized dynamics defined by the matrices L_c, L_s and L_u (which can always be decoupled from each other by a linear change of variables), and the nonlinear dynamics defined by the functions N_c, N_s and N_u. The center-manifold reduction theorem then states that the dynamics of the above dynamical system is homeomorphic to an equivalent

one which takes the form

$$\dot{a}_c = L_c a_c + N_c(a_c, h_s(a_c), h_u(a_c)), \tag{2.43}$$
$$\dot{a}_s = L_s a_s, \tag{2.44}$$
$$\dot{a}_u = L_u a_u. \tag{2.45}$$

where the functions $h_s(a_c)$ and $h_u(a_c)$ are algebraic relations that define the center manifold and that can be constructed as power expansions following an explicit procedure that imposes the exact invariance of the dynamics in such manifold. This method is a rigorous formalization of the adiabatic elimination of fast variables that is often used in many physical contexts. However, we will see that our specific problem exhibits some mathematical subtleties and unusual properties that will require a firm mathematical ground if to ensure reaching rigorous conclusions. Specifically, the fact that the theorem also applies in the presence of unstable modes, that is, including Eq. (2.45), which is not the usual case in typical physical applications, will be crucial to prove the instability of the center of mass.

The next step is now to apply the center-manifold reduction theorem to a certain value of the free parameter β close to one of the bifurcation points. First, in Section 2.6.2) we will study the bifurcation scenario of n-fold symmetrical (non-travelling) interfaces. Next, in Section 2.6.3 we study the special situation where the only marginal mode is $n = 1$ (i.e. $\beta - \beta_n \sim \mathcal{O}(1)$ for $n > 1$). And finally, we address the most interesting and nontrivial case of bifurcations into travelling solutions by reducing the dynamics in the bifurcations corresponding to β close to β_n for $n > 1$ (i.e. $\beta - \beta_2 \sim \mathcal{O}(\epsilon)$). The complex bifurcation in this nontrivial case will be elucidated with a complementary numerical study using extremely high-precision arithmetics.

2.6.2 Subcritical bifurcations into symmetric solutions

Here we obtain the bifurcation scenario to stationary petal-like symmetric shapes that do not travel. As opposed to related viscous-fingering-like problems, in our case the nonlinear growth of a linearly unstable mode saturates to a finite amplitude. These stationary solutions are stable with respect to perturbations that preserve their symmetry. Although we cannot obtain them analytically, we will show that a branch of unstable solutions that can be obtained explicitly bifurcates from the circular shape and defines a generic subcritical bifurcation scenario.

A symmetric interface is parametrized by a conformal mapping of the form $f = \sum_{m=0}^{\infty} a_{lm} e^{i(lm+1)s}$, where $l > 1$ is an integer value. The shape for $l = 2$ has the symmetry of an ellipse and for $l > 2$ of $l-$folded petals. We will refer

to them as l-symmetric. Because of the rotational invariance of our equations, this symmetry must be preserved by the dynamics if it is present in the initial condition. Accordingly, Eq. (2.39) is now written as:

$$\dot{a}_{lm} = \lambda(lm)a_{lm} + N_{lm}(a_0, a_l, a_{2l}...),$$

for $m \geq 0$.

Therefore, in a neighborhood of the instability threshold of the l-th mode, that is when β is close to β_l, the projection of the dynamics onto the center manifold is given by

$$\dot{a}_l = -a_l l(l^2-1)g_l + B(l)a_l|a_l|^2 + \mathcal{O}(\epsilon^5) \quad (2.46)$$

$$\dot{a}_{lm} = \lambda(lm)a_{lm} \quad (2.47)$$

for $m > 1$ and $m = 0$, and where formally we assume $a_l, g_l \sim \mathcal{O}(\epsilon)$. The coefficient $B(l)$ can be explicitly determined and is given for any $l > 1$ by

$$B(l) = \frac{(l^2-1)\,(26l^3 - 39l^2 + 6l - 1)}{8(3l+1)(2l-1)} > 0. \quad (2.48)$$

The sign of the coefficient $B(l)$ states that the bifurcation of the l-symmetric interfaces is always subcritical. On the other hand, for positive values of g_l there is a new branch of nonlinear l-symmetrical interfaces emerging from the corresponding bifurcation point $g_l = 0$. This means that while the $l-$mode is still linearly stable, it is nonlinearly unstable for finite-amplitude perturbations. The branch of solutions that bifurcates subcritically can be determined explicitly as a power expansion. The unstable branch of solutions can be parametrized with the area A and to lowest order it reads

$$A - \pi = \frac{\pi}{2}\frac{l\,(l^2-1)^2}{B(l)}g_l + \mathcal{O}(g_l^2), \quad (2.49)$$

where we expressed it in units in which the radius of the steady circle is 1.

2.6.3 Translational invariance and nonlinear instability of the center of mass

It is an interesting and illuminating exercise to determine the center-manifold reduction of our problem when the only marginal mode is the displacement mode $n = 1$, that is with $\beta - \beta_n \sim \mathcal{O}(1)$ for any $n > 1$. The fact that this mode is marginal reflects, at linear level, the translational invariance of the problem. To

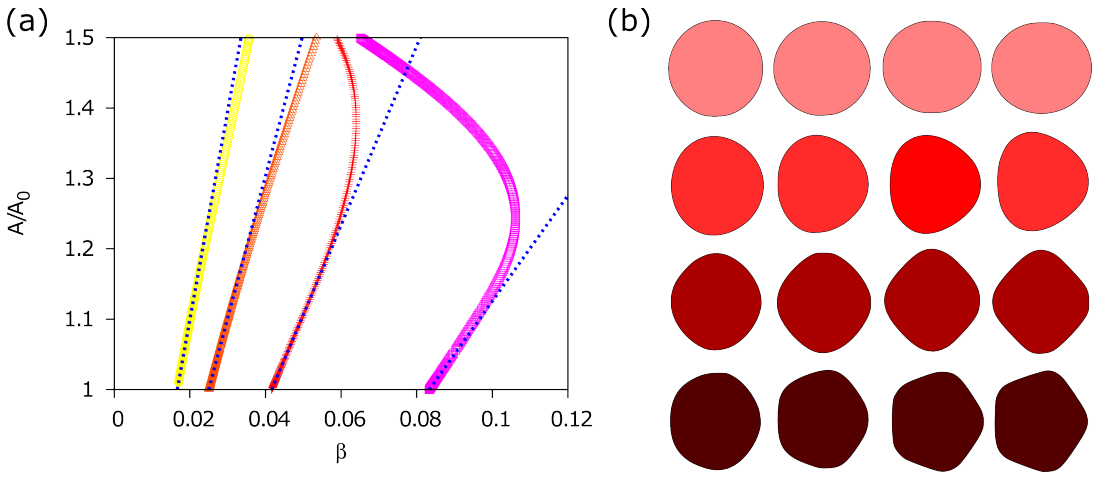

Figure 2.9: (a) Area normalized by the area of the steady circle ($A_0 = \pi R_0^2$) against β. Each pointed curve is an steady motile solution emerging from a different bifurcation point. The dashed lines are the analytical predictions for the first nonlinear term of the area of l-symmetric, Eq. (2.49). (b) Table of l-symmetric solutions. The dimensionless surface tension decrease from right to left.

gain insight into how the full nonlinear dynamics reflects this exact symmetry, we perform explicitly the center-manifold projection in this case. Note that the corresponding functions N_c, h_u and h_s defined in Eqs. (2.40)-(2.42) are nontrivial and must be determined order by order. We have carried out explicitly this procedure with the help of the symbolic calculus software *Mathematica* up to twentieth order, and have checked explicitly that there is an exact cancellation order by order. For simplicity we have restricted the analysis to real amplitudes. The center-manifold reduction of the problem in this case thus reads, formally assuming $a_1 \sim \mathcal{O}(\epsilon)$,

$$\begin{aligned} \dot{a}_1 &= \mathcal{O}(\epsilon^{22}), \\ \dot{a}_m &= \lambda(m) a_m. \end{aligned}$$

For $m > 1$ and $m = 0$. Similarly, we can determine explicitly $N(a_0, a_1, ...)$ from Eq. (2.38), and substitute all the mode amplitudes expressed in terms of a_1, and we obtain $\dot{a} = \mathcal{O}(\epsilon^{22})$. Therefore, for any finite value of a_1, we obtain a non-traveling solution. For consistence, this should correspond to a circle centered at a finite distance from the origin. Again, we can recover the shape that corresponds to a finite $a_1 \neq 0$ by writing explicitly the conformal mapping at the center-manifold, with all the amplitudes expressed in terms of a_1. It takes the form

$$f_{cm} = \frac{\delta e^{is}}{1 - a_1 e^{is}/\delta} + \mathcal{O}(\epsilon^{22}),$$

where

$$\begin{aligned}\delta &= 1 - a_1^2 - 2a_1^4 - 7a_1^6 - 30a_1^8 - 143a_1^{10} - 728a_1^{12} \\ &- 3876a_1^{14} - 21318a_1^{16} - 120175a_1^{18} - 690690a_1^{20}.\end{aligned}$$

This functional form corresponds precisely to a Möbius transformation that implements the translation of a unit circle to another one at finite distance. This proves, up to the order considered, that the different values that a_1 takes in the center manifold correspond to unit circles at rest.

If $\beta > \beta_2$, then all the fast modes are stable and it can be concluded that also at the nonlinear regime any initial interface would approach a circle asymptotically. Note, however, that the center of mass of the initial and the final interfaces need not coincide. During these transient evolution towards a final steady circle, the instantaneous velocity of the center of mass might be non zero, and hence, result into a global net displacement between the initial and the final state. For example, let us assume an initial interface given by the conformal mapping, $f(t=0) = R_0 e^{is} + a_1(t=0)e^{i2s}$, with the passage of time a_1 would remain constant whereas the other normal modes would relax exponentially towards its value at the center manifold, provoking a displacement of the center of mass between the initial and the final interfaces, $\Delta R_A \propto a_1(t=0)^3 \neq 0$. Therefore, during a transient it has propagated.

On the contrary, if $\beta < \beta_2$, there are some linearly unstable normal modes. If the initial condition close to the unit circle contains a certain finite amplitude on one of the unstable modes, the instantaneous velocity of the center of mass increases exponentially with time. For instance, if $\beta_2 > \beta > \beta_3$, a_2 would be the unique unstable mode. At short times a_2 would get away from the center manifold, contrary to the rest of fast modes. From Ref. [73], we know that the transverse perturbation to the center manifold $a_2 - h_{a_2}(a_1) \sim \exp(\lambda(2)t) + \mathcal{O}(\epsilon^2)$. Then, during a transient the instantaneous velocity of the center of mass would depend on time as $\dot{R}_A \sim (a_2 - h_{a_2}(a_1))^2 a_1 > 0$. The dynamics in this case cannot be extrapolated to long times because the local, weakly nonlinear analysis inherent to the center-manifold reduction is no longer valid. However, this argument proves the nonlinear instability of the center of mass, in the sense that an arbitrary perturbation of the unit circle, if $\beta < \beta_2$ will generically lead to an exponential displacement of the center of mass. Note that this does no yet imply that the motion can be sustained for all time. To explore analytically whether there may exist stationary propagating solutions that can be approached asymptotically, we must circumscribe the analysis to the neighborhood of a bifurcation point $\beta \sim \beta_n$, where the reduced description holds, and elucidate whether there are branches of asymmetric stationary solutions that bifurcate from that point, and whether

those solutions have a finite velocity. This analysis will be pursued in the following section.

2.6.4 Bifurcation to traveling solutions at $\beta = \beta_2$

Center manifold reduction for $\beta = \beta_2$

Here we address in detail the nonlinear dynamics of the system in a neighborhood of the critical value $\beta = \beta_2$. In this case all the fast normal modes are linearly stable and there are two slow modes, a_1 and a_2. We will combine and compare both analytical calculations obtained from a weakly nonlinear analysis at the critical point β_2, with the numerical solutions obtained from the procedure described at Section 2.4, so as to unveil a complex structure of the bifurcation scenario. One of the subtle points that cannot be elucidated analytically is whether or not the asymmetric solutions have a finite velocity. This is due to the fact that the dependence of the velocity with the distance to the bifurcation turns out to be transcendental (i.e. exponentially small), a non-adiabatic effect that can escape to the center-manifold reduction. To address this point, we have used high-precision arithmetics, up to 64 digits, as described in Section 2.4.2.

The center manifold in this case will include the modes amplitudes a_1 and a_2, which we restrict to be real for simplicity. In principle, it is expected that the nonlinear couplings of these amplitudes will break the rotational symmetry and open the possibility of sustained motion. As usual, in order to organize the expansion we assume a formal scaling with a book-keeping small parameter ϵ such that both slow modes are assumed to be of order ϵ as well as $g_2 \equiv \beta - \beta_2$. The structure of the bifurcation that arises from the projection of Eqs. (2.38-2.39) onto the corresponding center manifold turns out to be extremely involved and complicated. The lowest order nonlinear contributions to the dynamics of the system take the form

$$\dot{a} = 9 g_2 a_1 a_2 + \mathcal{O}(\epsilon^4), \tag{2.50}$$

$$\dot{a}_1 = 9 g_2 a_1 a_2 + \mathcal{O}(\epsilon^4), \tag{2.51}$$

$$\dot{a}_2 = -6 g_2 \left(a_2 - a_1^2\right) + \frac{9}{8} a_2^3 + \mathcal{O}(\epsilon^4), \tag{2.52}$$

$$\dot{a}_m = \lambda(m) a_m. \tag{2.53}$$

where $m > 2$. This illustrates how the nonlinear couplings give rise to a finite velocity, but also serves to illustrate how a naive analysis of the lowest orders may be strongly misleading. In fact, one could be tempted to extract stationary branches out of these equations. However, the order at which such an expansion can be truncated to completely unfold the nonlinear structure of the system is not

known *a priori*. One should proceed to the point where the number and structure of solutions is not modified by adding higher order contributions. Remarkably, the structure of the bifurcation scenario at β_2 in our case is unusually complex. With the help of symbolic calculus software, we have explicitly determined the center-manifold projection up to order fourteen in ϵ, and we have found that the number of stationary branches that bifurcate from β_2 keeps increasing at each order. Although without prove, this suggests that most likely the number of branches will be infinite, as new ones will come into play at each order of expansion. For completeness in Appendix 7.2, we provide Eqs. (2.50-2.52) at higher order in ϵ. The table (4.1) summarizes all the solutions found at order fourteenth. We write them to lowest order in g_2 for simplicity but we have determined them up to order ϵ^{14} (results not shown). These results are exact to the corresponding orders. The coefficients given in decimal notation are also known exactly but not written exactly for simplicity of the display. Notice that for all the solutions, the coefficient of the lowest order in g_2 of the area coincides with the value computed for the 2-symmetrical interfaces, Fig. (2.9). In general, the area difference between solutions starts to differ at the higher order terms in g_2. In Fig. (2.10), we plot a representation of the structure of the bifurcation obtained numerically.

In order to quantify the number of steady branches as a function of the order of the expansion in ϵ, a suitable mathematical procedure is particularly useful, based on the determination of the so-called Newton polygon of the resultant of the polynomials defined by the right-hand side of Eqs. (2.51-2.52) at a given order in ϵ (see Appendix 7.3 for details). We choose a_1 to be the variable of these polynomials, and so the coefficients are thought to be functions of a_2 and g_2. In general, their functional form changes with the order of ϵ at which Eqs. (2.51-2.52) has been truncated. One of the properties of our resultant is that the steady solutions of our system are roots from itself (see Appendix 7.3). In general, the polynomial form of our resultant would be $\sum_{i,j=0}^{k_i,k_j} c_{ij} a_2^i g_2^j$, where the coefficients c_{ij} are real numbers and k_i (k_j) sets the order of the resultant thought as a polynomial in a_2 (g_2). Accordingly, the Newton polygon is defined as the inferior convex envelope of all the points in the (i, j)-plane, such that the coefficient $c_{ij} \neq 0$ (see Fig. (2.11)). Therefore, it selects among all the terms of the resultant, the ones that may yield to solutions of Eqs. (2.51-2.52). In Fig. (2.11), we show that the Newton polygon changes with the order of ϵ, and that it does not present a clear signature of saturation at large orders. This is a strong indication that the number of solutions will keep increasing. In addition to that, we have observed that the Newton polygon changes regularly with the order of the expansion in ϵ of Eqs (2.51-2.52), suggesting that the number of solutions may indeed be infinite. As a final comment, let us remark that the solutions of this infinite set need not be all stable. On the contrary, one may expect that most of them will be unstable

$a_1^{st} = 2\sqrt[4]{3} g_2^{1/4}$ $a_2^{st} = \frac{16}{\sqrt{3}} g_2^{1/2}$	$a_1^{st} = \frac{\sqrt{2}}{\sqrt[8]{3}} g_2^{1/8}$ $a_2^{st} = \frac{2}{\sqrt[4]{3}} g_2^{1/4}$	$a_1^{st} = \frac{2^{1/3}}{3^{1/4}} g_2^{1/12}$ $a_2^{st} = -\frac{2^{2/3}}{\sqrt{3}} g_2^{1/6}$	$a_1^{st} \approx 2.1 g_2^{1/4}$ $a_2^{st} \approx 6.8 g_2^{1/2}$	$a_1^{st} \approx 1.9 g_2^{1/4}$ $a_2^{st} \approx 1.4 g_2^{1/2}$
$a_1^{st} \approx 1.7 g_2^{1/4}$ $a_2^{st} \approx 5.2 g_2^{1/2}$	$a_1^{st} \approx 1.4 g_2^{1/4}$ $a_2^{st} \approx 4.2 g_2^{1/2}$	$a_1^{st} \approx 0.2 g_2^{1/4}$ $a_2^{st} \approx 2.4 g_2^{1/2}$	$a_1^{st} \approx 2.0 g_2^{1/2}$ $a_2^{st} \approx 1.7 g_2^{1/4}$	$a_1^{st} \approx 0.7 g_2^{1/4}$ $a_2^{st} \approx 1.8 g_2^{1/2}$
$a_1^{st} = \frac{2}{\sqrt[4]{3}} g_2^{1/4}$ $a_2^{st} = \frac{64}{3} g_2$	$a_1^{st} = \frac{2}{\sqrt[4]{3}} g_2^{1/4}$ $a_2^{st} \approx -90.5 g_2$	$a_1^{st} = \frac{2}{\sqrt[4]{3}} g_2^{1/4}$ $a_2^{st} \approx 26.5 g_2$	$a_1^{st} = \frac{2}{\sqrt[4]{3}} g_2^{1/4}$ $a_2^{st} \approx 35.1 g_2$	$a_1^{st} = \frac{2}{\sqrt[4]{3}} g_2^{1/4}$ $a_2^{st} \approx -73.066 g_2$
$a_1^{st} = \frac{2}{\sqrt[4]{3}} g_2^{1/4}$ $a_2^{st} \approx 34.3 g_2$	$a_1^{st} \approx 1.8 g_2^{3/4}$ $a_2^{st} = \frac{4}{\sqrt{3}} g_2^{1/2}$	$a_1^{st} \approx 21.3 g_2^{3/4}$ $a_2^{st} = \frac{4}{\sqrt{3}} g_2^{1/2}$	$a_1^{st} \approx 30.6 g_2^{3/4}$ $a_2^{st} = \frac{4}{\sqrt{3}} g_2^{1/2}$	$a_1^{st} \approx 0.3 g_2^{3/4}$ $a_2^{st} = \frac{4}{\sqrt{3}} g_2^{1/2}$
$a_1^{st} \approx 10.9 g_2^{3/4}$ $a_2^{st} = \frac{4}{\sqrt{3}} g_2^{1/2}$	$a_1^{st} \approx 7.1 g_2^{3/4}$ $a_2^{st} = \frac{4}{\sqrt{3}} g_2^{1/2}$	$a_1^{st} \approx 4.7 g_2^{3/4}$ $a_2^{st} = \frac{4}{\sqrt{3}} g_2^{1/2}$	$a_1^{st} \approx 3.4 g_2^{3/4}$ $a_2^{st} = \frac{4}{\sqrt{3}} g_2^{1/2}$	$a_1^{st} = -5.1 g_2^{3/4}$ $a_2^{st} = \frac{4}{\sqrt{3}} g_2^{1/2}$
$a_1^{st} = 19.5 g_2^{3/4}$ $a_2^{st} = -\frac{4}{\sqrt{3}} g_2^{1/2}$	$a_1^{st} \approx 38.8 g_2^{3/4}$ $a_2^{st} = -\frac{4}{\sqrt{3}} g_2^{1/2}$	$a_1^{st} \approx 61.2 g_2^{3/4}$ $a_2^{st} = -\frac{4}{\sqrt{3}} g_2^{1/2}$	$a_1^{st} \approx 0.2 g_2^{3/4}$ $a_2^{st} = -\frac{4}{\sqrt{3}} g_2^{1/2}$	$a_1^{st} \approx 0.8 g_2^{3/4}$ $a_2^{st} = -\frac{4}{\sqrt{3}} g_2^{1/2}$

Table 2.1: Table of the solutions computed from Eqs. (2.51-2.52) expanded at order fourteenth in ϵ. The lowest order in g_2 of the area for every solution is $A - \pi = 8\pi g_2$. All the computed coefficients in powers of g_2 of the traveling velocity V_{st} are null for every steady solution. ($g_2 = \beta - \beta_2$)

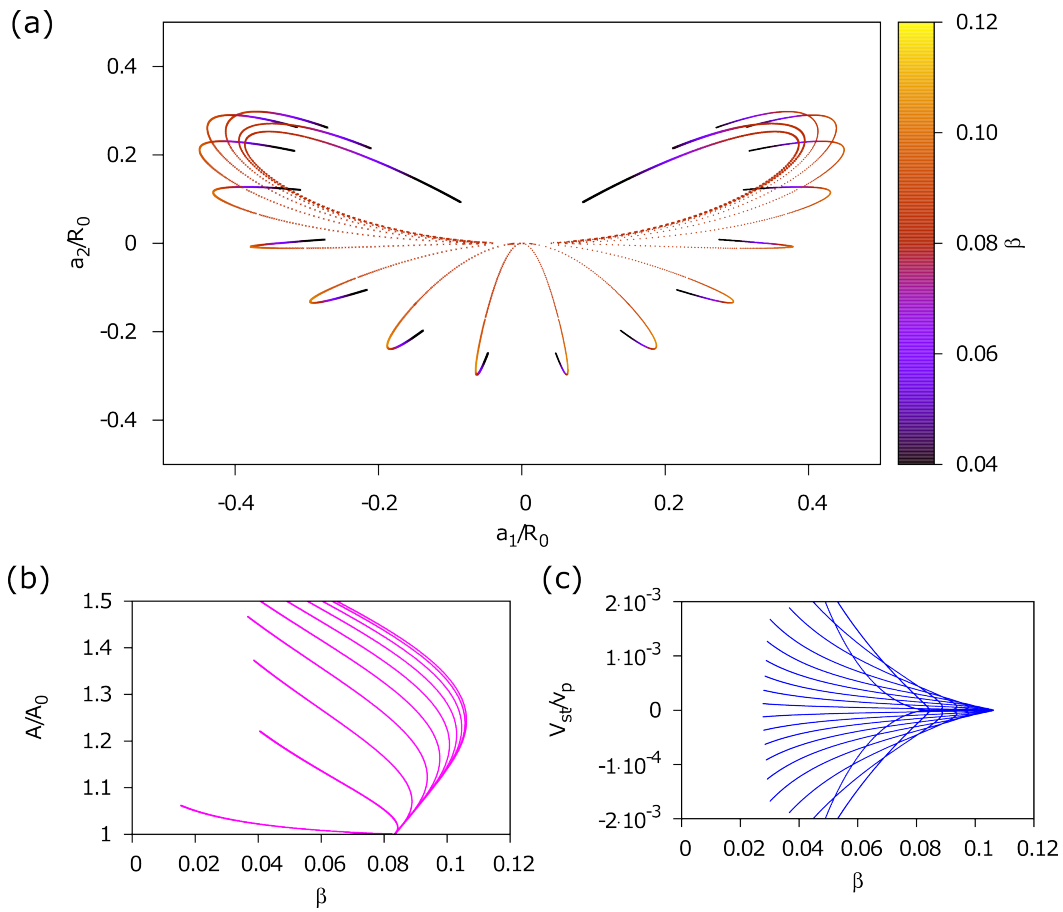

Figure 2.10: (a) Projection on the plane a_1/R_0-a_2/R_0 of steady solutions branching off the bifurcation point β_2 from Eq. (2.15). (b) Area normalised by the area of the steady circle against β. (c) Propagating velocity against β. Each curve represents a different steady interface emerging from the bifurcation point β_2.

and thus not directly observable, as seen in other Laplacian growth problems that exhibit high degeneracy [58].

Finite traveling velocity of asymmetric stationary solutions

One of our main motivations to pursue this analysis was to prove whether traveling solutions exist in this minimal model. Since we can derive explicitly a large number of stationary solutions, we can substitute them into the expression for the velocity of the center of mass and obtain their velocity. Interestingly, all these solutions have a remarkable property in common, which is that the traveling velocity obtained in a power expansion of g_2 following the this procedure vanishes at all orders considered. We have explicitly checked this point in all our high order computations of the expansions of Eqs. (2.51-2.52).

Nevertheless, this surprising cancellation order by order does not necessary

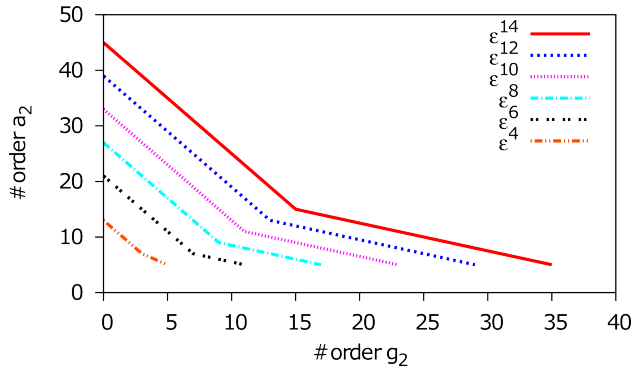

Figure 2.11: Newton's polygon of the Resultant computed from Eqs. (2.51-2.52) at the steady state expanded at different orders in ϵ. The x (y)-axis represents the order in g_2 (a_2) of the terms non-zero from the Resultant.

imply that the velocity is exactly zero, since it may well be that the dependence of the velocity on g_2 is transcendental, for instance exponentially small as $g_2 \to 0$. Since elucidating this limit numerically is computationally highly demanding, in a first exploration we use continuation techniques to follow some of these branches relatively far away from the bifurcation point, to visualize their asymmetry and correspondingly their finite velocity (see Fig. (2.10)). The maximum velocities obtained are indeed finite but still quite small compared to those measured for real cell fragments [25, 30], but this is not surprising taking into account that the effects that have been disregarded for simplicity of the analysis, most importantly the large scale polarization of the fragment, and the contribution of molecular motors, may have a significant quantitative impact.

To pursue the possible transcendental dependence of the velocity close to the bifurcation point, next we have performed a numerical continuation on β of a representative nonlinear asymmetric solution approaching the bifurcation point β_2 with 64 decimal digits accuracy. To this aim we define the function

$$E \equiv \frac{d\log(V_{st})}{d\log(g_2)} = \left\{ \begin{array}{cc} m & V_{st} \propto g_2^m \\ amg_2^{-m} & V_{st} \propto \exp(-a/g_2^m) \end{array} \right\}$$

that allows to discriminate between power law or exponential behaviors of V_{st} as g_2 approaches zero.

In Fig. (2.12), we plot the dependency of E as a function of the distance to the bifurcation point g_2, for the same solution at different orders of truncation of the numerical formulation N. For values of $g_2 < 10^{-2}$, each curve of E exhibits two different behaviors separated by a crossover value of g_2, which seems to decrease as N increases. Asymptotically, E tends to a constant value that fixes the characteristic exponent of the power law decay of V_{st}. Due to the fact that the numerical method introduces a truncation on the conformal mapping that parametrizes cell

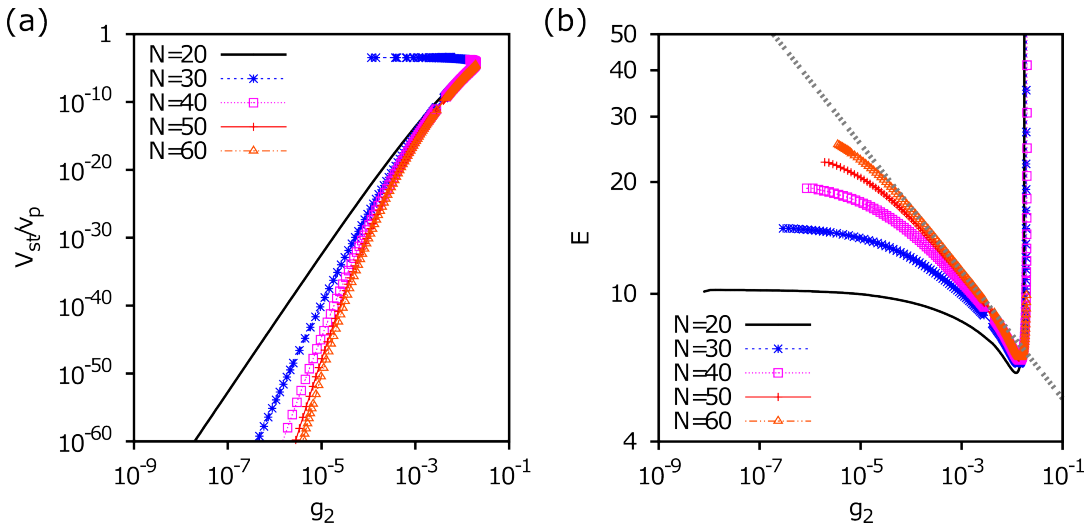

Figure 2.12: (a) Propagating velocity of a single steady solution against g_2 for different values of truncation number N. (b) E against g_2 for the curves from the left hand side figure.

shapes, the numerical steady velocity is expected to necessarily cross over to a power law decay, as it is seen in Fig. (2.12,b). It is the relevant to see if this effective exponent of the truncated system increases monotonically with N, which would be an indication that the exact steady velocity does not follow a power law. Indeed, if this were the case, the behavior would converge to this power with increasing N. The envelope of the E curves shows an intermediate linear regime reminiscent of an exponential decrease, whose range increases with N. By fitting this part with the ansatz $V_{st} \propto \exp(-a/g_2^m)$, we have obtained the values $a \approx 20.6$ and $m \approx 1/6$ (dashed curve in Fig. (2.12)). Consequently, this analysis supports the idea that the traveling velocities takes approximately the form

$$V_{st} \propto \exp(-20.6/g_2^{1/6}). \tag{2.54}$$

This result implies that the mechanism that endows the solutions with a finite velocity is non-adiabatic, in the sense that is missed by the center-manifold reduction. The latter is guaranteed to capture the correct bifurcation structure but it can indeed miss such non-adiabatic effects contained in transcendental dependencies. This puts our problem in contact with the class of problems sometimes referred to as controlled by asymptotics 'beyond all orders' [58].

Structural instability and translational symmetry

The above bifurcation scenario is quite complex. We have conjectured that the existence of an infinite number of branches and the transcendental dependency

of the velocity are deeply connected to the fact that the dynamical system at hand is actually structurally unstable for all values of the control parameter β. This is due to the fact that a_1 remains marginal in all cases, a condition that is imposed by a symmetry of the problem. According to the Peixoto theorem for two-dimensional dynamical systems [74], this fact, or equivalently, the existence of an infinite number of fixed points at a fixed β imply the structural instability. This means that any arbitrary small change in the form of the dynamical equations will qualitatively modify the bifurcation structure.

To pursue this point explicitly we have studied how the structure of the bifurcation scenario and in particular the asymptotic behaviour of V_{st} is modified upon a slight change in the dynamical equations.

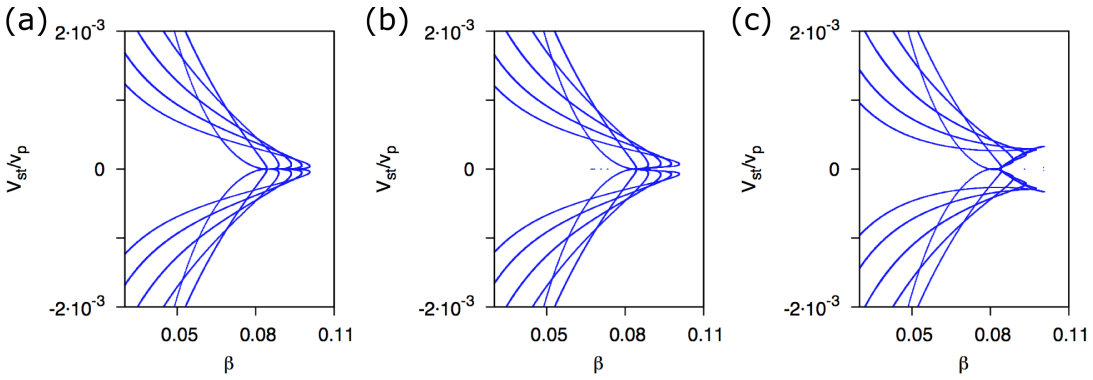

Figure 2.13: Propagating velocity against β. Each curve represents a different steady interface emerging from the bifurcation point β_2 from the dynamical system given by Eq. (2.15) plus the extra term $\delta a_1 g_2 e^{i2s}$. In (a) δ takes the value 10^{-1}, (b) 10^{-2} and (c) 10^{-6}. ($N = 20$)

As an example, we have added into Eq. (2.15) a new linear term onto the right-hand side ($\delta a_1 g_2 e^{i2s}$), where a_1 is the amplitude of first normal mode, g_2 is the distance to the bifurcation point β_2 and δ is a small parameter that defines the amplitude of the perturbation on the original dynamics. The form of this perturbation is arbitrary and does not respond to any physical justification. Note that the new term breaks the translational symmetry of the problem, enforced at linear level by the marginality of the mode $n = 1$ for all β. This perturbation also breaks rotational symmetry.

In Fig. (2.13), we see that the perturbation affects quantitatively the traveling velocity of the solutions, but the qualitative modifications are essentially affecting a small neighborhood of the bifurcation point. It is worth stressing that the asymptotic behavior of V_{st} is also altered by the perturbation. In order to contrast this idea, we have performed a numerical continuation on the same solution for a fixed truncation number ($N = 20$) and varying δ. As it is shown in Fig. (2.14,b), for values of $g_2 < 10^{-2}$, the function E goes from one plateau, corresponding to

the one of the unperturbed dynamics (Fig. (2.12,b)), to another one created by the perturbation of the system. The final value of $E \sim 5/4$ is compatible with the new nonlinear coupling ($\delta a_1 g_2$), provided that the steady amplitude of the first normal mode is $\propto g_2^{1/4}$. On the other hand, the value of g_2 that sets the crossover between these two regimes is correlated with δ. Notice that for a finite value of δ, the asymptotic behavior of V_{st} is altered qualitatively, even if the value of δ is taken arbitrarily small. This clearly illustrates the structural instability of this problem. Also as a corollary of the Peixoto theorem, it is know that the perturbed problem is in principle structurally stable itself, since the dynamical systems with this property are dense in the space of two-dimensional flows. Accordingly, the bifurcation structure of the perturbed problem is presumably the same as the one would obtain with any perturbation. In the context of the structural stability *dogma* as discussed by Guckenheimer and Holmes [74], according to which a reasonable physical model should be structurally stable, it is interesting to remark that, in our case, this lack of structural stability is a consequence of a symmetry of the problem. Consequently, any modification of the equations that leads to a structurally stable, robust model, in two dimensions, must break translational symmetry.

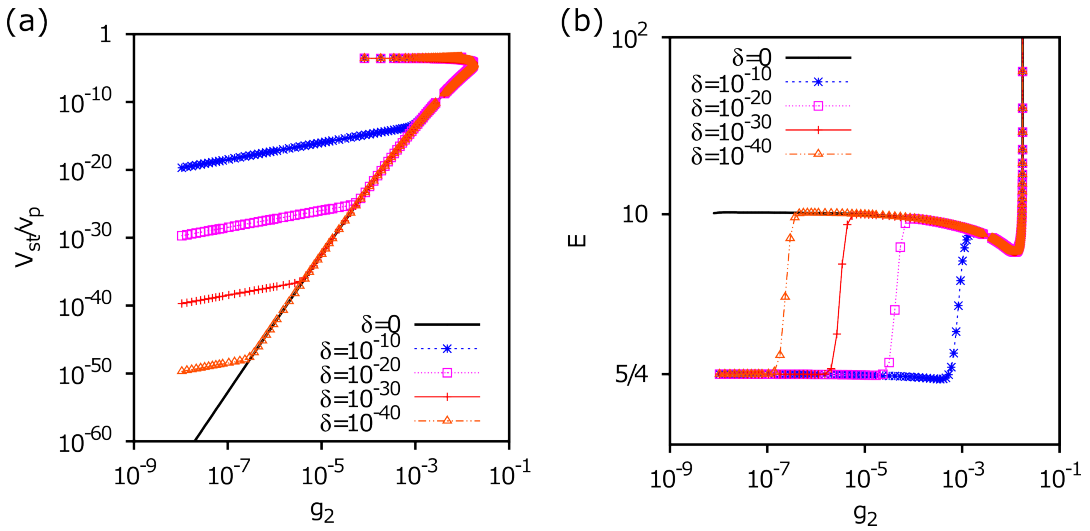

Figure 2.14: (a) Propagating velocity of a single steady solution of Eq. (2.15) plus the extra term $\delta a_1 g_2 e^{i2s}$ against g_2 for different values of δ. (b) E against g_2 for the curves from the left hand side figure.

Stability of the motile solutions

So far, we have discussed exhaustively a subfamily of steady motile solutions existing in our physical model. At his point, we briefly address the question of the stability of these solutions to small fluctuations. We have not explored this point

systematically via a linearization of the dynamics around this solutions, since this are known only numerically. Alternatively, we have addressed the problem from the direct integration of the dynamics from distant initial conditions. Even without being systematic, in this way we can get an idea of the basin of attraction of the stable solutions.

Based on the numerical scheme detailed in Section 2.4.1, we integrate the interfacial dynamics of the free boundary problem. In Fig. (2.16a), we show an example of a trajectory of an initial steady circular interface under random, small perturbations for a values of $\beta < \beta_2$. In general, we detect that for these type of initial conditions, the peanut-shaped motile solution is the one with a largest basin of attraction within random fluctuations of the circle. Nevertheless, there are other motile solutions that coexist with the previous one, as it is shown in Fig. (2.16,b). From our partial exploration of this aspect, it is plausible to expect that the majority of the stationary branches shown in Fig. (2.10) will be unstable and hence essentially unobservable.

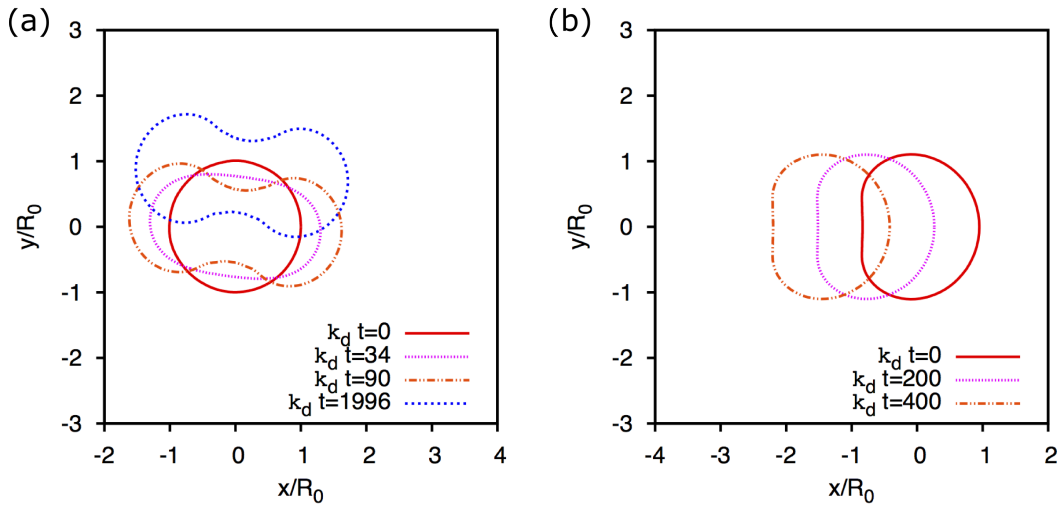

Figure 2.15: (a) Time evolution of a randomly perturbed circular interface for $\beta = 0.06$. (b) Time evolution of a randomly perturbed beam-shaped solution for $\beta = 0.04$.

2.7 Discussion

In this chapter, we have studied the mechanisms that generate motion of perturbed circular actin lamellar fragments, in the absence of molecular motors and of any regulation of the actin polarization. We have shown that spontaneous symmetry-breaking is sufficient to initiate and sustain motion, via a nonlinear mechanism. The minimal model here studied was previously introduced by [55],

who reported a viscous-fingering-like linear instability. The model assumes that the flow of actin, which polymerizes at the cell interface and depolymerizes at the bulk homogeneously, follows a Darcy law. We have shown that when one takes into account nonlinearities, polymerization forces together with friction alone are capable to generate motion through a symmetry-breaking morphological instability, in the absence of molecular motors forces, regulation of the polarization field or any explicit symmetry-breaking of the equations. This results settles a controversial issue, contradicting previous claims that spontaneous motion under these conditions was not possible [59].

We have elucidated the nonlinear character of the instability that makes lamellar fragments spontaneously motile, with the help of center-manifold techniques and high-precision numerical integration. The weakly nonlinear analysis has allowed us to prove the nonlinear instability of the center of mass, and to unfold a complex bifurcation scenario. With the help of the numerical approach, we have shown that the traveling velocity is conferred by non adiabatic effects, and so it cannot be detected neither through linear analysis nor through a weakly nonlinear analysis over the morphological perturbations on the steady circular shape. In the next figure we show a table of a family of representative motile solutions.

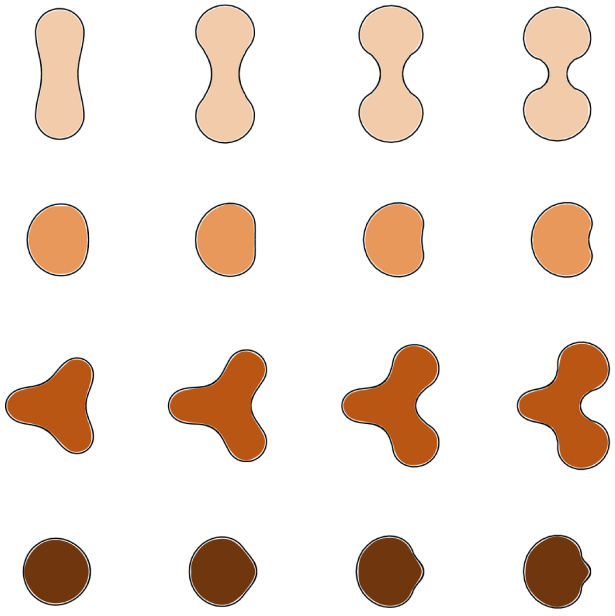

Figure 2.16: Representative examples of the stationary propagating shapes. β increases from right to left and velocity increases from left to right.

We have proved an exact and simple expression that connects the center of mass velocity to the shape of the cell fragment, which provides a new insight into the interplay of the geometry and the kinematics of the problem. This type of relation has also been generalized to a broad class of quasi-twodimesnional

systems, not limited to Darcy flows, and including molecular motors, more realistic boundary conditions at the membrane, and possible inhomogeneities.

The predicted speeds in our minimal model may differ significantly from the typical velocities observed in cell fragments. This quantitative discrepancy can be explained by invoking different physical ingredients that are neglected in the model studied here. Our results must be seen as a proof-of-principle for basic mechanisms of cell motility. Although the model may not be a complete and realistic description of cell fragments, however, the detailed understanding of the basic mechanisms may be realistic from an evolutionary perspective, in the context of much more primitive forms of living matter. Obviously, evolution has generated much more complicated and highly regulated machineries within the cytoskeleton which may coexist or combine with the one exposed here, and contribute to a much more efficient locomotion [60, 64].

As a final remark, it is worth stressing that, in addition to its possible biological relevance, the model here studied is interesting from a physical point of view as a new prototype within the class of Laplacian free-boundary problems in the context of interfacial pattern formation, and also as a new example of a self-propelled systems under non-equilibrium conditions.

Acknowledgments:

We thank À. Jorba and C. Simó for illuminating discussions on the mathematical subtleties of this problem, for suggesting us the Newton's polygon analysis developed in Section 2.6.4 and for help in the use of very high-precision arithmetics.

Chapter 3

Morphology and growth of polarized tissues

3.1 Introduction

The regulation of the growth and shape of tissues is a fundamental property of living organisms. The recent development of new experimental techniques has thrown light on the role of force generation at the cellular scale in tissue morphogenesis. For example, cells can reorganize collectively inducing local deformations and forces, which can be isotropically or anisotropically distributed, by cell division and cell apoptosis [75, 76]. Reciprocally, the biophysical properties of the tissue can alter the state of the cells. Therefore, it is relevant to study the mechanisms that control cell organization and shape tissues [32, 77, 78]. Cell orientation is essential for tissue elongation. For example, in the case of plants it has been shown that the cortical array of microtubules set a preferential direction for cell growth [79, 80, 81]. Another example is the wing disk of the fruit fly *Drosophila melanogaster* in which gradients of morphogens are responsible for the determination of a macroscopic orientation [32, 82]. In this article we focus on the deformations induced at the scale of the tissue shape by oriented cell division. This mechanism requires two essential ingredients: cell replication coupled to a global polarisation of the system [83]. The forces produced by this mechanism in general are anisotropically distributed.

The inclusion of growth in continuum models of elastic tissues has been discussed and applied by several authors [84, 85, 86]. However, it has been shown that at sufficiently long time scales, a hydrodynamical description of a growing tissue as a viscous fluid is justified [83, 87, 88]. Our model here extends the approach of Ref. [87]. The constitutive equations of the tissue are similar to those of an active nematic fluid [1, 3]. Cell division is an active process, in the sense that

it requires a consumption of chemical energy. It is taken into account both as a source of matter and as an active local stress. Most of our discussion deals with confluent tissue layers on a substrate.

The present chapter is organised as follows: First, we present the model and discuss the underlying hypotheses. Then we study the dynamics of the small deformations of an initially circular tissue. In the second and third sections, we extend our results to larger deformations in two limiting regimes, either the dissipation upon growth is dominated by viscous drag forces with the substrate or by tissue viscosity, respectively. Finally, we will analyze two possible generalizations of the physical model: one in which we account for a mechanical coupling between the internal stresses and cell division processes and the other in which we briefly analyze the morphodynamics of $3d$ tissues.

3.2 Physical model

We aim at describing the time evolution of a polarized tissue with an arbitrary initial shape and a spatially uniform rate of expansion. The model is an extension of a previous continuum approach for polarized tissues discussed in Refs. [82, 87], including additional forces that compete with the active stresses, such as friction forces with the environment and effective surface tension at the tissue boundary.

Our physical description is given in terms of the macroscopic fields: the cell density ρ, the cell velocity $\mathbf{v}$, the local cell orientation characterized by a unit vector $\mathbf{p}$, the total internal stresses $\sigma^{tot}_{\alpha\beta}$ and the pressure field P. In this coarse-grained description, the macroscopic fields are assumed to be averaged over a small region comprising several cells.

The cell number balance equation includes a source term which accounts for the increment in cell number due to proliferation and the decrease of cell number due to cell death. We write it as

$$\partial_t \rho + \partial_\alpha(\rho v_\alpha) = k_c \rho, \tag{3.1}$$

where greek indices denote cartesian coordinates and we adopt the Einstein summation convention over repeated greek indices. The growth rate $k_c > 0$ is the difference between cell division and cell death rates. For simplicity we also assume that the tissue is incompressible so that the cell density ρ is assumed to be constant.

Our focus on long time scales, such that local cell rearrangements and cell proliferation/death events lead to an effective fluid-like behaviour of the tissue [83, 87, 88]. Furthermore, a growing tissue must be considered as an active material

because cell division is an active process, which requires a continuous consumption of chemical energy [1]. In this paper we study polarized tissues where the cells have a well-defined orientation ($\mathbf{p}$), which we assume to be fixed by an external field such as a morphogen gradient. Consequently, we treat the tissue as an active polar nematic fluid. The constitutive equation for the total stress in an active nematic fluid is discussed in Refs. [1, 3] and reads

$$\sigma_{\alpha\beta}^{tot} = \eta(\partial_\alpha v_\beta + \partial_\beta v_\alpha) - P\delta_{\alpha\beta} - \sigma_0 p_\alpha p_\beta, \tag{3.2}$$

where η is the effective shear viscosity. The last term on the right hand side is the anisotropic active stress. It exists for symmetry reasons, if the tissue has a macroscopic nematic order, and reflects that the active (energy consuming) process of cell division is spatially oriented. Its amplitude σ_0 is a phenomenological parameter. In principle, within a linear theory the contribution of cell division/death to the active stress should be proportional to the growth rate (i.e. $\sigma_0 \propto k_c$). However, there may be other contributions to σ_0 due to, for example, the activity of the individual cells, which consume ATP. A detailed explanation of the origin of active stresses in a growing tissue can be found in Ref. [83]. It can be shown that for tissues growing in two dimensions that we mostly study below, the case where $\sigma_0 > 0$ and $\mathbf{p}$ points in a given direction is equivalent to the case where $\sigma_0 < 0$ and $\mathbf{p}$ points in the perpendicular direction. Without loss of generality, in the following we assume $\sigma_0 > 0$.

When writing the force balance in the tissue, we include an internal viscous drag force proportional to the local velocity field. In a $2d$ tissue, growing on a solid substrate to which it is weakly attached by transmembrane proteins, the drag force may be due to the relative movement between the tissue and the substrate [88]. On the other hand, for a tissue growing in a $3d$ space, the drag force could be due to the permeation of an external medium through the tissue [89]. It is worth mentioning that both mechanisms are fundamentally different. Neglecting inertia, the force balance condition can be written as

$$\partial_\alpha \sigma_{\alpha\beta}^{tot} - \xi v_\beta = 0, \tag{3.3}$$

where ξ is the friction coefficient per unit area or per unit volume.

In order to simplify the model, we consider that $\mathbf{p}$, k_c, η, σ_0 and ξ are spatially uniform. Furthermore, without loss of generality we choose the coordinate system such that the polarization $\mathbf{p}$ is parallel to the x-axis. Therefore, the two coupled equations describing the growth of the tissue are

$$\eta\Delta\mathbf{v} - \nabla P = \xi\mathbf{v}, \tag{3.4}$$

$$\nabla \cdot \mathbf{v} = k_c. \tag{3.5}$$

It has been argued by several authors that surface effects in a tissue can be described in terms of an effective surface tension [90]. We consider here that the surface tension $\gamma > 0$ is isotropic and we write a mechanical boundary condition at the surface of the tissue ($\partial\Omega$) of the form

$$\sigma^{tot}_{\alpha\beta}\hat{n}_\beta|_{\partial\Omega} = -\gamma\kappa\hat{n}_\alpha, \tag{3.6}$$

where κ denotes the local total curvature of the interface and $\hat{n}$ is the normal vector at the interface pointing outwards. This form imposes vanishing tangential stresses and the Young-Laplace pressure drop condition. We neglected implicitly the viscous effects of the outer medium. Note that the active stresses do not show up explicitly in the bulk equations (3.4,3.5), but are introduced through the boundary condition Eq. (3.6). The evolution of the tissue shape can then be described as the evolution of its boundary, which is determined by the continuity condition at the boundary

$$V_n = \mathbf{v}\cdot\hat{n}|_{\partial\Omega} \tag{3.7}$$

where V_n is the normal component of the boundary velocity given by the value of $\mathbf{v}$ from Eqs. (3.4,3.5,3.6), at the boundary. The dynamics of the tissue is thus formulated as a free-boundary problem.

Some integral properties of the dynamics can be derived exactly for any shape of the tissue and arbitrary parameter values. The simplest ones are obtained in Appendix 7.4. The first global property states that the total area, A (volume, $\mathcal{V}$) of the tissue grows exponentially regardless of the shape, with $A = A_0\exp(k_c t)$ ($\mathcal{V} = \mathcal{V}_0\exp(k_c t)$). This result reflects the fact that we neglect any dependence of the growth rate on stress. Another remarkable exact result is that, under the assumptions of our model and regardless of the shape, the center of mass of the tissue cannot move. This point is not trivial since, in the presence of friction forces, the motion of the center of mass of an active polar fluid could be triggered by morphological symmetry breaking of the boundary as discussed in Chapter 2, [91].

The relative importance of the three different types of passive stresses in the problem depend on the spatial scale considered. Capillary stresses are generically dominant for a small tissue, with high curvature and small velocities. In the opposite limit, for a large tissue, with large velocities, friction forces dominate. Viscous stresses are typically most relevant at intermediate scales. The material parameters of the tissue define three intrinsic length scales that control the crossover between these regimes. The capillary length $L_c \equiv \gamma/(\eta k_c)$ defines the crossover scale between capillary forces, dominant for smaller scales, to viscous forces at larger scales. Similarly, we define a friction length $L_\eta \equiv \sqrt{\eta/\xi}$ as the scale where viscous and friction forces are comparable. At length scales smaller

than L_η viscous stresses dominate the dissipation while at length scales larger than L_η friction dominates the dissipation. The combination of these two lengths defines yet another length scale as $L_\xi \equiv (L_c L_\eta^2)^{1/3} = (\gamma/(k_c\xi))^{1/3}$, which compares capillary against friction forces. The orders of magnitude of these length scales for a $2d$ tissue are $L_\eta \sim 10 - 100$ μm and $L_c \sim 1 - 100$ μm, for typical values of the friction coefficient $\xi \sim 10^3$ Pa·s/μm^2, the growth rate $k_c \sim 1$/day, the surface tension $\gamma \sim 100$ Pa·μm and the shear viscosity $\eta \sim 10^5 - 10^7$ Pa·s, respectively [92, 82, 93]. Consequently, $L_\xi \sim 10 - 100$ μm.

In the following, unless explicitly stated, we focus only on the study of $2d$ tissues growing on a solid substrate.

3.2.1 Linear perturbation analysis of the circular shape

We consider first a tissue spreading in 2 dimensions with an initially circular shape and a varying radius $R(t)$ in the absence of active stresses (i.e. $\sigma_0 = 0$). Cells are constantly produced at a rate k_c and the constraint of constant density imposes a radial flow of cells towards the periphery, which drives the expansion of the tissue. By solving Eq. (3.5), we obtain the radial flow field at position $\mathbf{r}$, $\mathbf{v}_0 = (k_c/2)\mathbf{r}$, where the origin is chosen at the center of the tissue. Using the force balance equation Eq. (3.4), and the Young-Laplace law Eq. (3.6) one can calculate the pressure field induced by the friction forces (there is no viscous contribution in this case). Therefore, the pressure field results in $P_0(r,t) = -\xi k_c(r^2 - R(t)^2)/4 + \eta k_c + \gamma/R(t)$. The size of the tissue grows exponentially: $\dot{R}(t) = k_c R(t)/2$. Consequently, in the absence of active stresses, an initially disk-shaped tissue remains thus circular and increases its area exponentially over time. Importantly, if $\gamma = 0$ and $\xi = 0$, this uniform exponential growth is also exact for any arbitrary shape. The tissue has a self-similar growth with a uniform scale factor that grows exponentially in time (see Appendix 7.5 for details).

Now, we consider that the amplitude of the active stress σ_0 is finite but of order $\epsilon \ll 1$. In order to quantify the anisotropy of the tissue, we use the aspect ratio H, defined as the ratio between the major and minor axes. Taking a circular tissue with radius $R(t)$ as an initial state, we perform a linear perturbation analysis in ϵ to follow the interfacial dynamics. The active stresses create on the system perturbations of order σ_0. The position of the edge of the perturbed tissue would be given in polar coordinates by $r(\theta,t) = R(t) + a_2(t)\cos(2\theta)$, where $a_2(t)$ is of order σ_0, and θ is the polar angle.

We express the new velocity and pressure field as $\mathbf{v} = \mathbf{v}_0 + \epsilon\delta\mathbf{v}$ and $P = P_0 + \epsilon\delta P$, where δP and $\delta\mathbf{v}$ are the perturbation to the pressure and the velocity field induced by the active stress, respectively.

Then, we solved Eqs. (3.4-3.7) for the perturbed fields using the computational software Mathematica. The interface dynamics at linear order in ϵ, in terms of the instantaneous radius $R(t)$ and the aspect ratio $H(t) = 1 + 2a_2(t)/R(t) + \mathcal{O}(\epsilon^2)$ reads

$$\frac{dR}{dt} = \frac{k_c}{2} R, \tag{3.8}$$

$$\frac{dH}{dt} = -k_c \left(f_1(\frac{R}{L_\eta}) + \frac{L_c}{L_\eta} f_2(\frac{R}{L_\eta}) \right) (H-1) \tag{3.9}$$

$$+ \frac{\sigma_0}{\eta} f_3(\frac{R}{L_\eta}), \tag{3.10}$$

where the functions f_i in units of $L_\eta = 1$ read

$$f_1(R) = \frac{R^2 \left((R^2+8) - 4\,(R^2+4)\,\Pi(R) \right)}{\left((R^2+8)^2 + 32 \right) - 4\,(R^2+6)\,(R^2+8)\,\Pi(R)}, \tag{3.11}$$

$$f_2(R) = \frac{6}{R^3} f_1(R), \tag{3.12}$$

$$f_3(R) = \frac{4\left((R^2+12) - (5R^2+24)\,\Pi(R) \right)}{\left((R^2+8)^2 + 32 \right) - 4\,(R^2+6)\,(R^2+8)\,\Pi(R)}, \tag{3.13}$$

where $\Pi(R) = I_1(R)/(RI_0(R))$, $I_1(R)$ and $I_0(R)$ being modified Bessel functions of the first kind [94].

In the following, we discuss the asymptotic behaviour of the interfacial dynamics at the linear regime.

3.2.2 Discussion of the limiting regimes

In this section we discuss the relevant asymptotic limiting cases, in order to gain some physical insights on the mechanisms that control the temporal evolution of the shape of the tissues in the presence of anisotropic cell division. To make the discussion clearer, we constructed a diagram of states of the tissue where the coordinates are $L_c/R(t)$ and $L_\eta/R(t)$, as shown in Fig. (3.1). Four asymptotic regions are distinguished in this diagram according to the relative values of the various intrinsic length scales of the problem.

It is important to remark that the trajectories of a growing tissue are represented in the diagram of state (3.1) as straight lines approaching the origin as the time passes.

- In region A where $L_\eta \gg R \gg L_\xi$, viscous forces dominate the dissipation in the tissue and balance the active stress. In this regime, the aspect ratio

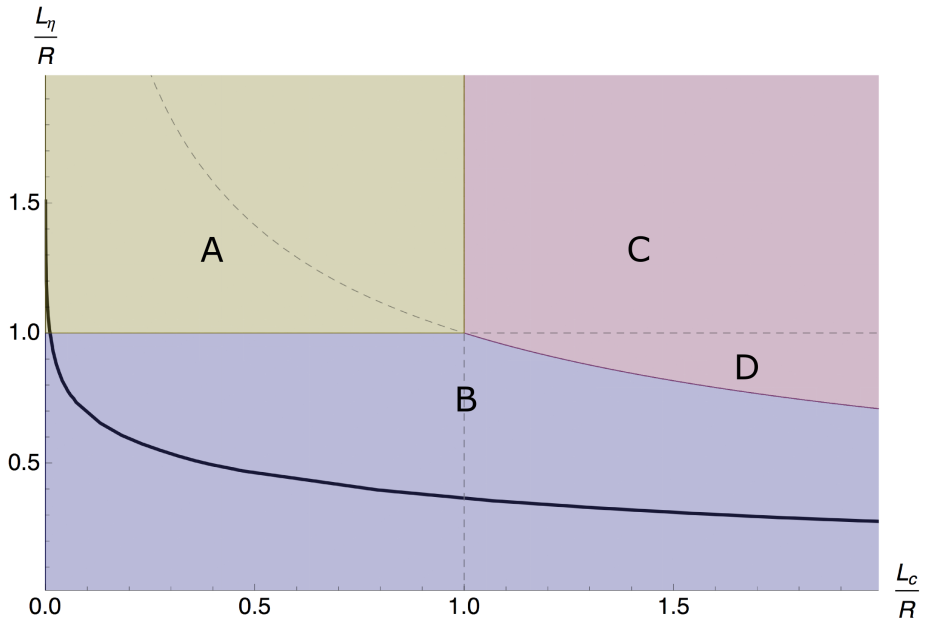

Figure 3.1: Diagram of states subdivided into the three regions of dominance of passive forces: viscous (yellow), capillary (red) and friction (blue). R is the instantaneous radius of the tissue. The boundaries of the various regimes are defined as $R = L_c$, $R = L_\eta$ and $R = L_\xi$ and the dashed curves are the extension of these boundaries. The transition between regions C and D occcurs for $R = L_\eta$. The solid black curve marks the points where the aspect ratio attains its maximum value, for initial radius $R_0 \to 0$, that is, the envelope curve in Fig. (3.2b) (gray triangle line). For finite R_0 the points of maximal aspect ratio occur below this curve, essentially always in region B. is the envelope of the radius R_M shown in Fig. (3.2) and represents the size of the tissue at which the aspect ratio is maximum regardless of the initial size R_0

satisfies

$$\frac{dH}{dt} \approx -\frac{k_c \xi R^2}{6\eta}(H-1) + \frac{\sigma_0}{2\eta}. \tag{3.14}$$

The aspect ratio grows essentially linearly with time and the shape of the tissue becomes anisotropic. In the limit $\xi = 0$, we recover the linear approximation of the case studied in Ref. [87], where the aspect ratio grows exponentially in time.

- In region B where $R \gg L_\eta, L_\xi$, the dissipation is dominated by the friction forces. The aspect ratio satisfies

$$\frac{dH}{dt} \approx -k_c (H-1) + \frac{4\sigma_0}{\xi R^2}. \tag{3.15}$$

Eventually, at long times, any tissue enters into this regime where the aspect ratio relaxes to one regardless of its initial morphology, and reaches a circular

shape assymptotically. This implies that if the initial morphology of the tissue is circular, the aspect ratio increases from one and reaches a maximum before relaxing back to one.

- In the two other regions C and D, the variation of the aspect ratio is dominated by capillary forces. Surface tension drives the tissue to isotropic circular shapes. In region C where $L_\eta, L_\xi \gg R$ the dissipation is dominated by viscous effects and in addition to the cell division time there is a second capillary relaxation time $\propto \eta R/\gamma$. The aspect ratio varies according to

$$\frac{dH}{dt} \approx -\frac{\gamma}{\eta R}(H-1) + \frac{\sigma_0}{2\eta}. \tag{3.16}$$

In region D where $L_\xi \gg R \gg L_\eta$, the dissipation is dominated by friction and the capillary relaxation time is $\propto \xi R^3/\gamma$. The aspect ratio varies according to

$$\frac{dH}{dt} \approx -\frac{6\gamma}{\xi R^3}(H-1) + \frac{4\sigma_0}{\xi R^2}. \tag{3.17}$$

In order to characterize the anisotropy of a growing tissue, from now on, we focus on the evolution of initially circular shapes (i.e. $H(t=0)=1$) and denote by R_0 the initial radius. We integrate numerically the general equations (3.8,3.10) for the aspect ratio and the radius of the tissue, at linear order in the deviation from the circular shape, assuming that the active stress σ_0 is small. In general, the aspect ratio $H(t)$ has a maximum at finite time. We define $H_M(L_c, L_\eta, R_0, \sigma_0/\eta k_c)$ as the maximum aspect ratio during a dynamical evolution and $R_M(L_c, L_\eta, R_0, \sigma_0/\eta k_c)$ as the radius at which the aspect ratio is maximal. As shown on Fig. (3.2), H_M is larger for smaller initial radius.

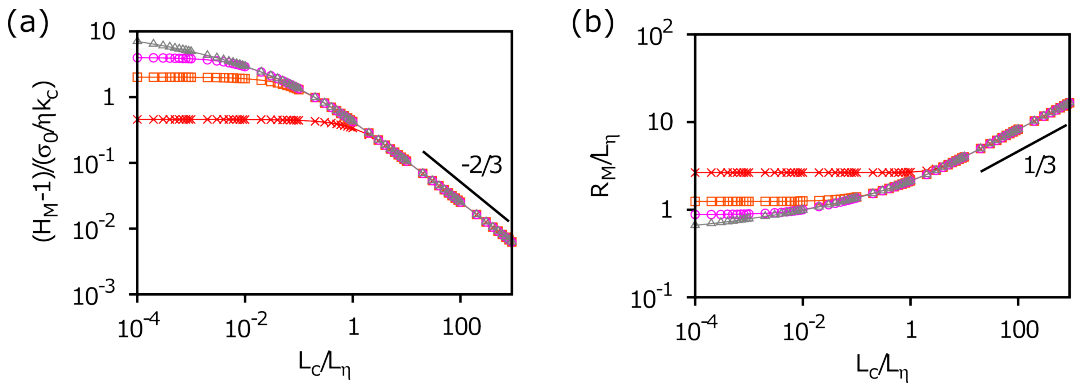

Figure 3.2: (a) H_M as a function of L_c/L_η for different values of R_0, R_0/L_η: 1 (red cross), 0.1 (orange square), 0.01 (pink circle) and 0.0001 (gray triangle). (b) R_M as a function of L_c/L_η using the same color code.

3.3 Friction-dominated growth

In this section we study in more detail the friction regime in which viscous forces are neglected, corresponding to regions B and D in the diagram of states of Fig. (3.1). In order to do so, we implement a numerical scheme based on the conformal mapping formulation derived in Section 3.3.1, which allows to compute the evolution of the shape from an arbitrary initial condition, and therefore to go beyond the linear regime discussed in the previous section. Conformal mapping techniques provide a powerful framework to deal with free-boundary Laplacian problems in $2d$, in particular to allow for analytical insights, such as shown in Section 3.3.2. The connection of the friction-dominated regime to similar problems of Laplacian growth is discussed below.

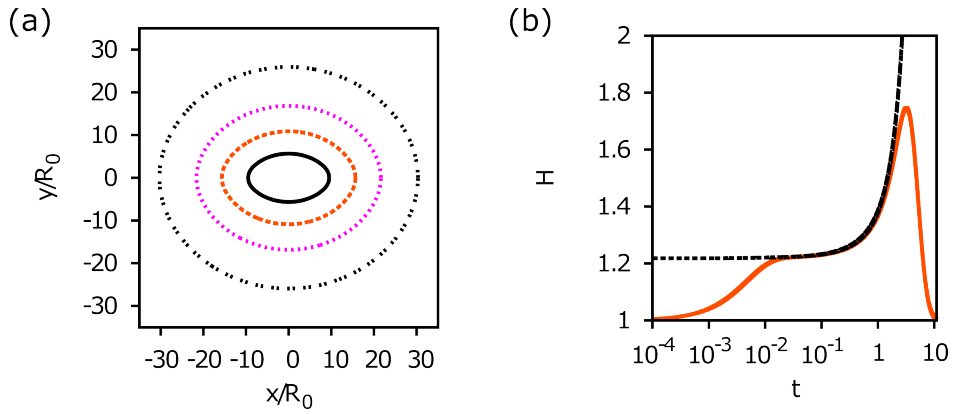

Figure 3.3: Friction-dominated growth. (a) Temporal evolution of the shape of an initially circular tissue with $R_0 = 0.3$ and $\gamma = 1$, where we show the decrease of the aspect ratio at late stages. The color-code stands for $t = 4$ (solid black), $t = 5$ (punctuated orange), $t = 6$ (dotted pink) and $t = 6.5$ (patterned gray). (b) The solid red curve is the temporal evolution of the aspect ratio for the left-hand side case. The dashed black curve is Eq. (3.36) for $\gamma = 1$ and the corresponding perimeters at each instant of time of the left-hand side case. Both figures are in units of $\sigma_0/2 = \xi = k_c = 1$.

If R is the average radius of an almost circular tissue, the friction regime is defined by $R \gg L_\eta$. In this case we approximate the original physical model for tissue growth by an incompressible Darcy flow combined with the stress-free boundary conditions

$$-\nabla P = \xi \mathbf{v}, \tag{3.18}$$

$$\nabla \cdot \mathbf{v} = k_c, \tag{3.19}$$

$$P|_{\partial\Omega} = \gamma\kappa - \sigma_0 \hat{n}_x^2, \tag{3.20}$$

$$V_n = \mathbf{v} \cdot \hat{\mathbf{n}}|_{\partial\Omega}. \tag{3.21}$$

The active stress produces anisotropic forces on the edge of the tissue.

The morphodynamics in the friction dominated regime can be understood qualitatively as follows. For $R \ll L_\xi$, capillary forces are dominant and therefore the interface relaxes to mechanical equilibrium faster than it grows (Eq. (3.17)). Consequently the morphology of the tissue evolves in a quasi-static manner such that the aspect ratio increases. On the contrary if $R \gg L_\xi$, friction forces tend to suppress the effects of the active stresses on the morphology, (Eq. (3.15)), and consequently the aspect ratio of the tissue decreases upon growth. In Fig. (3.3), we show a typical dynamical evolution of the shape and of the aspect ratio. As in the previous section, the aspect ratio shows a maximum H_M at a finite area ($\equiv \pi R_M^2$).

The quasi-static growth of the regime $R \ll L_\xi$ can be described analytically in more detail. In Section 3.3.2 we discuss a family of nontrivial shapes for which the active stresses balance exactly the surface tension, when the growth rate can be taken as vanishingly small. The evolution in this early regime is expected to follow quasi-statically the corresponding sequence of shapes within this family, as shown in Fig. (3.3b).

In Fig. (3.4), we plot both the maximum aspect ratio H_M and the corresponding radius R_M as a function of the initial radius R_0. For both curves, there are clearly two regions separated by a single length scale which is proportional to the length $L_\xi = (\gamma/(\xi k_c))^{1/3}$, which compares the capillary forces against friction forces.

We now give a simple scaling analysis based on the perturbation equations (3.15,3.17). For $R_0 \ll L_\xi$, the aspect ratio evolves quasi statically as $H(t) - 1 \propto \sigma_0 R(t)/\gamma$, whereas in the large size limit the aspect ratio decays as $H(t) - 1 \propto \sigma_0/\xi k_c R(t)^2$. Therefore by matching these two behaviors, we find that the size at which they coincide and the maximal aspect ratio scale as

$$R_M \propto \left(\frac{\gamma}{\xi k_c}\right)^{1/3} = L_\xi, \tag{3.22}$$

$$H_M - 1 \propto \frac{\sigma_0}{(\gamma^2 \xi k_c)^{1/3}}, \tag{3.23}$$

regardless of the initial size R_0.

On the contrary, if $R_0 \gg L_\xi$, the system is already in the large size limit so $H(t) - 1 \propto \sigma_0/\xi k_c R(t)^2$, and the maximum aspect ratio is reached for a radius proportional to R_0. In this limit, we therefore obtain the following scaling

$$R_M \propto R_0, \tag{3.24}$$

$$H_M - 1 \propto \frac{\sigma_0}{\xi k_c R_0^2}. \tag{3.25}$$

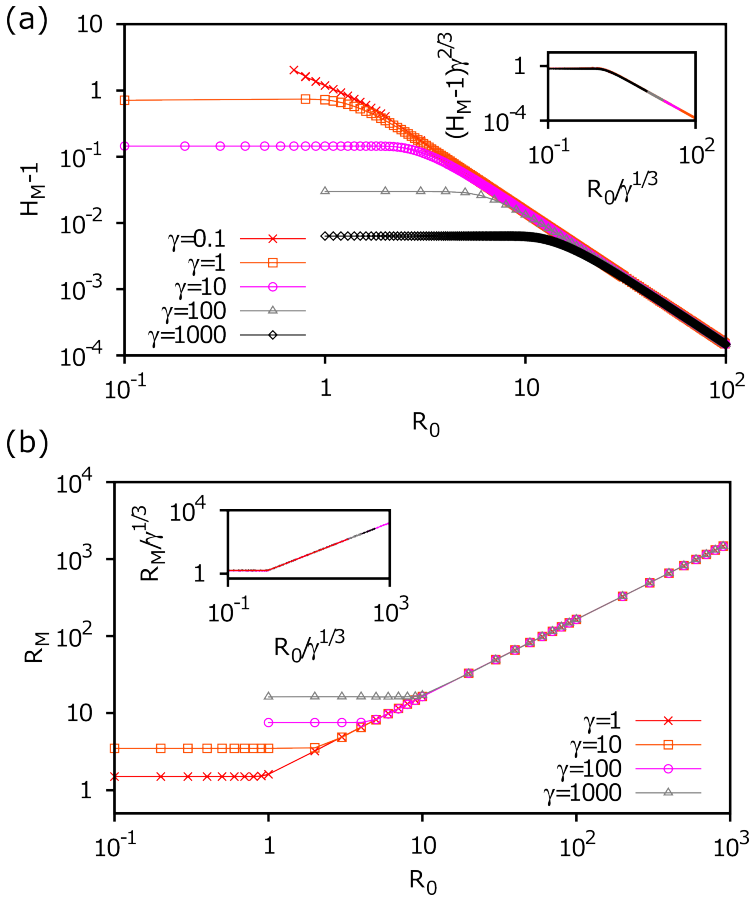

Figure 3.4: Friction-dominated growth. (a) Maximum aspect ratio (H_M) as a function the initial radius R_0. Inset: Master curve obtained by rescaling the radius by L_ξ and the aspect ratio by $\gamma^{2/3}$. (b) Radius at which the aspect ratio is maximal (R_M), as a function of the initial radius R_0 for various values of the surface tension γ. Inset: Master curve obtained by rescaling the lengths by L_ξ. Both figures are in units of $\sigma_0/2 = \xi = k_c = 1$.

In the inset of Fig. (3.4), we rescale the axis to obtain master curves for R_M and H_M showing that our numerical results satisfy these scaling laws.

3.3.1 Conformal mapping formalism for Darcy flow

The physical model constructed in the friction dominated regime defines a new variant of the class of Laplacian growth problems [56, 58]. These free-boundary problems have in common a (usually $2d$) incompressible flow with a Laplacian velocity potential. The different interface dynamics is then determined by the distinct boundary conditions satisfied by the velocity potential at the interface. The model discussed in Chapter 2 is another example in the biological context. These problems can be formulated using conformal mapping techniques, which

usually provide analytical insights and also a convenient numerical scheme that is competitive with other more general boundary-integral methods provided that the shape boundaries are not very contorted. Following Refs. [56, 71], in this section we derive an explicit interface dynamical equation in the friction dominated limit using conformal mapping techniques.

The scheme of the derivation is analogous to the one shown in Section 2.3. In this section, we will provide the main steps followed to construct the equation that governs the temporal evolution of the interface of a tissue driven by the mechanism of anisotropic cell division.

In the friction-dominated regime, the internal cell flow is approximated by an incompressible Darcy flow (3.18-3.19) complemented by the Young-Laplace condition at the interface (3.20). We redefine the pressure and velocity fields according to $P = P' - \xi k_c r^2/4$ and $\mathbf{v} = \mathbf{v}' + k_c \mathbf{r}/2$ such that the new fields $\mathbf{v}'$ and P' satisfy the equations,

$$-\nabla P' = \xi \mathbf{v}', \tag{3.26}$$

$$\nabla \cdot \mathbf{v}' = 0, \tag{3.27}$$

that correspond exactly to the bulk equations of usual viscous fingering-like problems [56, 58]. Therefore P' is a Laplacian field.

After this change of variables the kinematic boundary condition reads

$$P'|_{\partial\Omega} = \frac{\xi k_c r^2}{4} + \gamma\kappa - \sigma_0 \hat{n}_x^2. \tag{3.28}$$

In this context, the contour of the interface can be described by a complex function $z = f(\phi, t)$ that maps the unit circle on a reference domain into the physical interface of our tissue, being ϕ the polar angle of the circle in the reference domain and $z = x+iy$ the complex coordinate in the physical domain. The second variable t refers to time, to indicate that the shape evolves with time. The kinematic boundary condition in terms of this parametrization reads

$$P'|_{\partial\Omega} = \frac{\xi k_c |f|^2}{4} + \gamma\kappa[f] - \sigma_0 \frac{Re[\partial_\phi f]^2}{|\partial_\phi f|^2}. \tag{3.29}$$

where $\kappa[f] = \mathrm{Im}[\partial_\phi^2 f \partial_\phi f^*]/|\partial_\phi f|^3$. The other interfacial quantities can be written in terms of the conformal mapping as

$$V_n = \frac{\mathrm{Im}[\partial_t f^* \partial_\phi f]}{|\partial_\phi f|}, \tag{3.30}$$

$$\mathbf{v}' \cdot \hat{n} + \frac{k_c}{2} \mathbf{r} \cdot \hat{n}|_{\partial\Omega} = -\frac{1}{\xi} \frac{\partial_\phi \psi'}{|\partial_\phi f|} + \frac{k_c}{2} \frac{\mathrm{Im}[f^* \partial_\phi f]}{|\partial_\phi f|}, \tag{3.31}$$

where ψ' is the harmonic conjugate of P'.

Following Refs. [56, 71], $\psi' = \mathcal{H}_\phi[P']$, where $\mathcal{H}_\phi$ is the Hilbert transform in the unit circle (2.10).

Therefore combining the previous results, one obtains the next dynamical equation for the contour of the tissue

$$\mathrm{Im}[\partial_t f^* \partial_\phi f] = \frac{k_c}{2}\mathrm{Im}[f^*\partial_\phi f] - \partial_\phi \mathcal{H}_\phi[\frac{k_c|f|^2}{4} + \frac{\gamma}{\xi}\kappa[f] - \frac{\sigma_0}{\xi}\frac{\mathrm{Re}[\partial_\phi f]^2}{|\partial_\phi f|^2}] \quad (3.32)$$

The numerical integration of the dynamics is based on this equation, which is reduced to a set of ordinary differential equations for the Fourier coefficients of the function $f(\phi)$. The numerical scheme is analog to the one in Section 2.4.

3.3.2 Exact stationary solutions

In this section we derive a class of exact stable solutions in the friction-dominated regime in the case where there is no tissue growth but in the presence of finite active stresses. These stationary solutions would correspond to situations where one can claim the existence of anisotropic active stresses that do not originate in cell division, but on other active processes of the cells. Even if the only active stresses are those of cell division, these solutions are still relevant to the dynamics as the sequence of shapes that the tissue is following quasi-statically, due to the fast relaxation of capillary forces (with a time scale ($\propto \xi R^3/\gamma$)) compared to the time scale of growth ($1/k_c$), so that $\xi R^3/\gamma \ll 1/k_c$. In this case, the radius can be considered as a slow variable that can be eliminated adiabatically. Remarkably, to the extent that the tissue dynamics can be considered to follow these shapes quasi-statically, the analysis of the morphology is not restricted to a small perturbation of the circle, since the solutions are exact. At this point it is worth stressing that such exact solutions in Laplacian-growth problems with a finite surface tension, where capillary forces can exactly cancel the corresponding driving forces of the problem are very rare. The only two non-trivial situations where this has been shown to be possible so far in viscous fingering problems are reported in Refs. [95, 96]. Remarkably and contrary to those referred examples, our solutions are here linearly stable and therefore they are directly observable and play a relevant role in the dynamics.

Following the preceding examples, we start with an ansatz of exact mechanical equilibrium at the interface with zero flow, which reads

$$\gamma\kappa - \sigma_0 \hat{n}_x^2 = P_0 = P_1 - \frac{\sigma_0}{2}\left(\hat{n}_x^2 + \hat{n}_y^2\right), \quad (3.33)$$

where P_0 and P_1 are integration constants. The last equation is evaluated at the edge of the tissue. Parametrizing the contour with the arclength (s), Eq. (3.33) becomes

$$\gamma \partial_s \Theta(s) - \frac{\sigma_0}{2} \cos\left(2\Theta(s)\right) = P_1, \tag{3.34}$$

where $\Theta(s)$ is the angle between the tangent vector at the interface and the axis of cell polarization, taken as the x-axis. The analytical solutions belong to a family of uniparametric curves, controlled by the dimensionless parameter

$$\alpha^2 \;=\; 1 + \left(\frac{4\pi\gamma}{\sigma_0 L}\right)^2, \tag{3.35}$$

where L is the perimeter of the contour.

It is important to stress that in the absence of cell division, the area is a conserved geometrical quantity, and therefore the perimeter is a one-to-one function of the area. In Fig. (3.5), we plot some examples of the previous solutions. The aspect ratio of a given solution of this family takes the form

$$H = \sqrt{\frac{\alpha+1}{\alpha-1}} \frac{\arctan\left(\frac{\sqrt{2}}{\sqrt{\alpha-1}}\right)}{\operatorname{arctanh}\left(\frac{\sqrt{2}}{\sqrt{\alpha+1}}\right)}. \tag{3.36}$$

The asymptotic behaviours of the aspect ratio can be found in the corresponding limits of small and large values of the dimensionless perimeter $\frac{\sigma_0 L}{\gamma}$,

$$H \sim \quad 1 + \tfrac{\sigma_0 L}{6\pi\gamma} \qquad \frac{\sigma_0 L}{\gamma} \ll 1, \tag{3.37}$$

$$H \sim \quad \tfrac{\sigma_0 L}{4\gamma \log(\sigma_0 L/2\gamma)} \qquad \frac{\sigma_0 L}{\gamma} \gg 1. \tag{3.38}$$

Finally, we checked numerically that these solutions are generically stable to small perturbations. In addition, Eq. (3.17) states that at linear regime these exact solutions are stable as well.

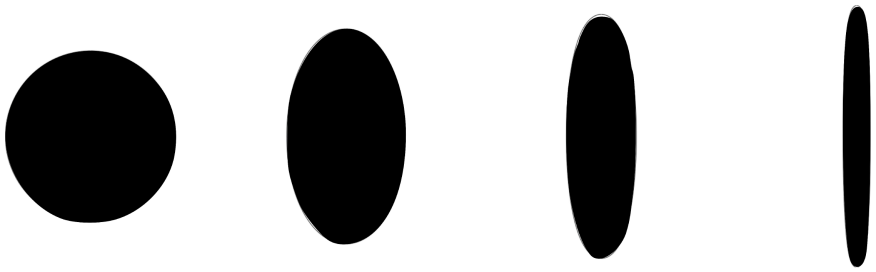

Figure 3.5: Illustrative examples of exact stable solutions. The parameter α decreases from left to right. The shapes are oriented in the vertical axis for convenience.

3.4 Viscosity-dominated growth

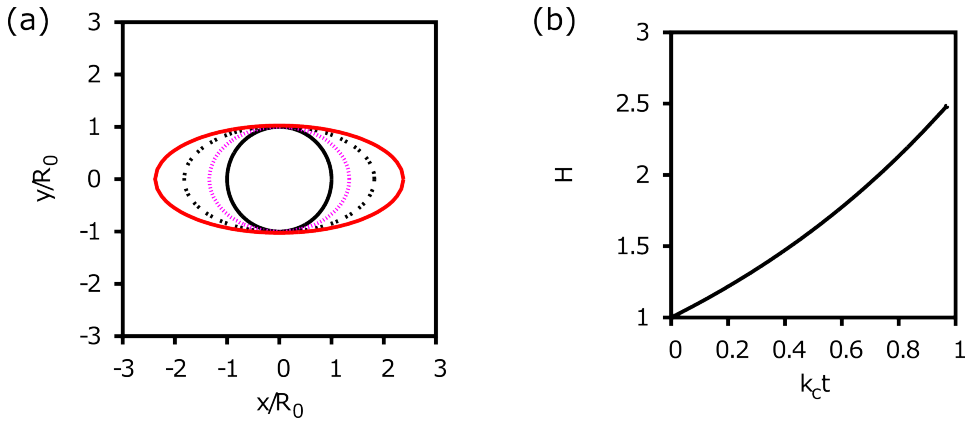

Figure 3.6: Viscosity-dominated growth. (a) Temporal evolution of the shape of an initially circular tissue with $R_0 = 10$ and $\sigma_0 = 1$. The color-code stands for $t = 0$ (black), $t = 0.3$ (red), $t = 0.6$ (orange) and $t = 0.9$ (pink). (b) Temporal evolution of the aspect ratio from left-hand side case. Both figures are in units of $2\eta = k_c = \gamma = 1$.

In this section, we extend our discussion to the regime defined by $R \ll L_\eta$, corresponding to regions A and C by using conformal mapping techniques. In this regime, only viscous and capillary forces are considered. The ratio between these two forces defines the capillary length scale L_c. Contrary to the friction dominated regime (i.e. $R \gg L_\eta$), the shape anisotropy grows monotonically over time (Fig. (3.6)) because neither the capillary force nor the viscous force can counterbalance the active stresses. Nevertheless the interface dynamics depends on the value of the initial radius of the circular tissue (R_0) compared to L_c, as shown in Fig. (3.7). For $R_0 \gg L_c$, we recover the self-similar growth found in Ref. [82]. On the contrary if $R_0 \ll L_c$, capillary effects act during a transient time estimated to be around $t \sim \log\left(L_c/R_0\right)/k_c$, inducing quasi-static deformations of the shape of the tissue. The aspect ratio grows then as $H(t) \sim \sigma_0 R(t)/\gamma$ as seen from Eq. (3.16).

3.4.1 Conformal mapping formalism for Stokes flow

Conformal mapping techniques can also be used to describe the evolution in the viscosity-dominated regime, in which the problem corresponds to a Stokes flow. In this section we derive the corresponding formulation, taking $\xi = 0$.

We first subtract from the physical fields the reference solution found in the absence of surface tension as $\mathbf{v} = \mathbf{v}' + (Ax, By)$ and $P = P' + C$ where $A \equiv (k_c + \sigma_0/2\eta)/2$ and $B \equiv (k_c - \sigma_0/2\eta)/2$ and $C \equiv \eta k_c - \sigma_0/2$. The original

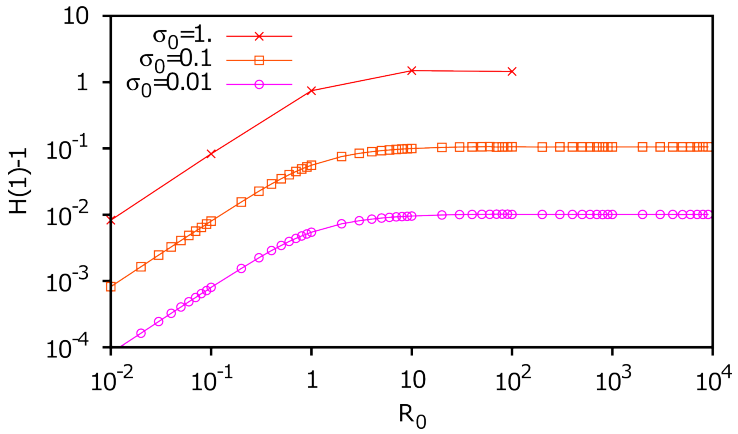

Figure 3.7: Viscosity-dominated growth. Aspect ratio at the time point $t = 1$ as a function of the radius R_0 of the initial circular shape for different values of σ_0. The values are in units of $2\eta = k_c = \gamma = 1$.

incompressible Stokes flows converts then into

$$\eta \Delta \mathbf{v}' - \nabla P' = 0, \tag{3.39}$$
$$\nabla \cdot \mathbf{v}' = 0. \tag{3.40}$$

These equations are formally equivalent to the hydrodynamic equations of a passive incompressible isotropic fluid. Although, the boundary conditions are transformed into

$$\left(\eta \left(\partial_\alpha v'_\beta + \partial_\beta v'_\alpha\right) - P' \delta_{\alpha\beta}\right) \hat{n}_\beta|_{\partial\Omega} = -\gamma \kappa \hat{n}_\alpha, \tag{3.41}$$
$$V_n = \mathbf{v}' \cdot \hat{n} + (Ax, By) \cdot \hat{n}|_{\partial\Omega}. \tag{3.42}$$

We have thereby eliminated the active and anisotropic ingredients of the original equations. It is now possible to make use of conformal mapping techniques to solve these dynamical equations. For more details about the derivation, we refer the reader to the Refs. [71, 97].

The pressure field P' is harmonic and the stream function ψ' associated to the velocity field $\mathbf{v}'$ is biharmonic. We define the Airy stress function $\mathcal{A}$ as:

$$-P' + \eta \left(\partial_x v'_x - \partial_y v'_y\right) = -2\eta \partial_y^2 \mathcal{A}, \tag{3.43}$$
$$\eta \left(\partial_y v'_x + \partial_x v'_y\right) = 2\eta \partial_{xy}^2 \mathcal{A}, \tag{3.44}$$
$$-\delta P + \eta \left(\partial_y v'_y - \partial_x v'_x\right) = -2\eta \partial_x^2 \mathcal{A}, \tag{3.45}$$

which by construction is also a biharmonic function. Using the Goursat represen-

tation of biharmonic functions ψ' and $\mathcal{A}$ [71] may be expressed in the form:

$$\mathcal{A} + i\psi' = -z^*\mu(z) - \chi(z), \tag{3.46}$$

where $z = x + iy$ is the complex coordinate, x and y being the cartesian coordinates. The two functions, μ and χ are analytic functions. Using the Goursat representation and parametrizing the physical interface with a conformal mapping $z = f(\phi, t)$, that maps the contour of a unit circle into the physical interface, being ϕ the polar angle of the circle in the reference domain and $z = x + iy$ the complex coordinate in the physical domain, we can rewrite the stress free boundary conditions (3.41) as

$$z\left(\frac{d\mu}{dz}\right)^* + \left(\frac{d\chi}{dz}\right)^* + \mu + \mathcal{G}(\phi)\Big|_{z=f(\phi,t)} = 0, \tag{3.47}$$

$$\mathcal{G}(\phi) = \frac{\gamma}{2\eta}\int^{\phi} \kappa[f(\phi', t)]\partial_{\phi'} f(\phi', t) d\phi'. \tag{3.48}$$

and the kinematic boundary condition (3.42) as

$$\mathrm{Im}[\partial_t f^* \partial_\phi f] \;=\; -\mathrm{Im}[(2\mu + \mathcal{G})\,\partial_\phi f^*] + \mathrm{Im}[\frac{f}{2}\left(\frac{\sigma_0}{2\eta}\partial_\phi f - k_c \partial_\phi f^*\right)]. \tag{3.49}$$

where $\kappa[f] = \mathrm{Im}[\partial_\phi^2 f \partial_\phi f^*]/|\partial_\phi f|^3$.

We used these equations to solve numerically the time evolution of the shape of the tissue in the viscous-dominated regime, such as those shown in Fig. (3.6).

3.5 Model extensions

In our study we have omitted several effects and introduced simplifications for the sake of clarity of the analysis. Here we briefly discuss how the current scenario would be enriched or modified by the consideration of some of these additional effects.

An important restriction of our analysis is to assume that the rate of cell division and apoptosis does not vary across the tissue, in particular that is not affected by the local stress. This may not be justified in particular when stresses become large, resulting in some type of confinement of the growing regions to the appropriate boundary layers [98]. Inhomogeneous growth rates are certainly expected to affect the resulting morphology. In Section 3.5.1, we briefly discuss the problem near homeostatic conditions and we show that the circular tissue can reach a finite aspect ratio different from one at long times.

Another effect that could be introduced in the formalism is an anisotropy of the effective surface tension (i.e. $\gamma = \gamma_0 + \gamma_1(\mathbf{p}\cdot\hat{n})^2 > 0$), [99]. This could play a major role for small enough tissues and compete with the anisotropic cell division in defining the transient shapes of the growing tissue.

Regarding the dynamics of the cell polarization field, we have simplified the model by imposing that the axis of cell division is fixed by a spatially homogeneous external field. This is a justified assumption for instance in the growth of the imaginal disk of the fruit fly *Drosophila melanogaster* [82]. More generally, one could consider situations with a preferential cell orientation at the boundaries [100] or the reorientation of cell polarity by shear flow [101], which may be relevant in other contexts of tissue morphodynamics.

Finally, throughout this study we have mostly addressed the case of $2d$ tissues. The case of three-dimensions is qualitatively similar and is briefly discussed in Section 3.5.2.

3.5.1 Tissue growth near the homeostatic state

In this section we briefly discuss the morphodynamics of a tissue that grows close to the homeostatic state and contrast the results with respect to the physical picture presented in the rest of this chapter. The discussion is limited to the friction-dominated regime and for simplicity we neglect capillary effects. We consider here a case in which the mechanical environment of the cell affects the cell state.

As a starting point we take the model given by Eqs. (3.18-3.19) with the boundary condition $P|_{\partial\Omega} = -\sigma_0(\hat{n}_x^2 - \hat{n}_y^2)/2$ and the kinematic equation (3.7), except that now the growth rate depends on the local stress, as $k_c(P) = k_c - P/\bar{\eta} > 0$. The quantity $\bar{\eta}$ has units of a viscosity. Its order of magnitude is estimated to be $\bar{\eta} \sim 10^9$ Pa·s for a spheroid composed of CT26 cells, [98], and the single characteristic length scale for this system is $L_{\bar{\eta}} \sim \sqrt{\bar{\eta}/\xi} \sim 1$ mm.

In the absence of active stresses (i.e. $\sigma_0 = 0$) a circular tissue spreads isotropically as shown in Fig. (3.8 a). If $R(t) \ll L_{\bar{\eta}}$, we observe an exponential growth which suggests that $k_c(P)$ is roughly homogenous across the tissue, whereas if $R \gg L_{\bar{\eta}}$, then the radius increases linearly in time. This indicates that in the central region of the tissue, the division and death rates are balanced (homeostatic conditions) and thus only the cells at a distance of the order of $L_{\bar{\eta}}$ from the edge have a significant net proliferation rate.

On the other hand, the active stresses are anisotropically distributed along the edge of the tissue, as well as the growth rate ($k_c(P)|_{\partial\Omega} = k_c + \sigma_0(\hat{n}_x^2 - \hat{n}_y^2)/2\bar{\eta}$). In order to study the aspect ratio of the tissue, we performed a linear perturbation

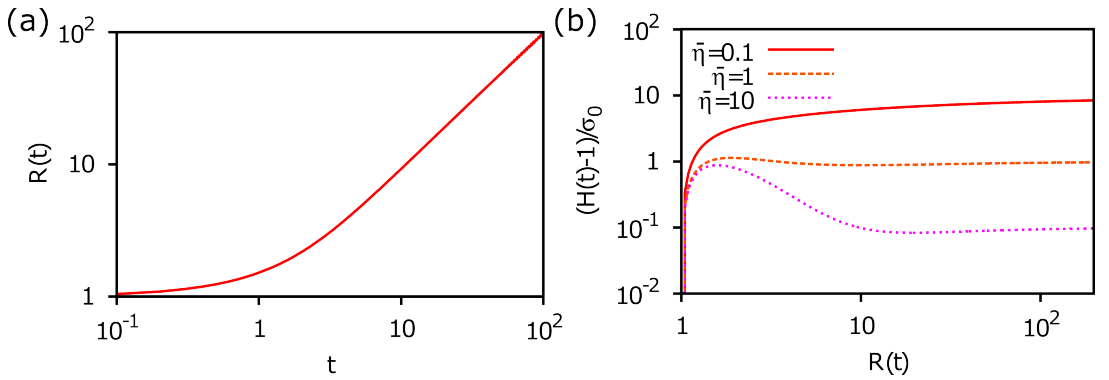

Figure 3.8: (a) Dynamical evolution of the radius (Eq. (3.50)) of an initially circular tissue for $\bar{\eta} = 100$. (b) Dynamical evolution of the aspect ratio (Eq. (3.51)) against the instantaneous radius with a circular tissue as an initial condition. Both figures are in units of $R_0 = \xi = k_c = 1$.

analysis considering $\sigma_0 \sim \mathcal{O}(\epsilon)$. The active stress causes and elliptical deformation on the shape of the tissue, $(r(\theta, t) = R(t) + a_2(t)\cos(2\theta))$, where $a_2(t) \sim \mathcal{O}(\epsilon)$. The aspect ratio is defined as $H(t) = 1 + 2a_2(t)/R(t) + \mathcal{O}(\epsilon^2)$. The dynamical equations obtained for $R(t)$ and $H(t)$ at linear order in ϵ are

$$\frac{dR}{dt} = k_c L_{\bar{\eta}} \frac{I_1(R/L_{\bar{\eta}})}{I_0(R/L_{\bar{\eta}})}, \tag{3.50}$$

$$\frac{dH}{dt} = -k_c \left(\frac{I_1(R/L_{\bar{\eta}})^2}{I_0(R/L_{\bar{\eta}}) I_2(R/L_{\bar{\eta}})} - 1 \right) (H-1) + \frac{\sigma_0}{\xi R^2} \left(-2 + \frac{R}{L_{\bar{\eta}}} \frac{I_1(R/L_{\bar{\eta}})}{I_2(R/L_{\bar{\eta}})} \right), \tag{3.51}$$

where $I_2(R/L_{\bar{\eta}})$, $I_1(R/L_{\bar{\eta}})$ and $I_0(R/L_{\bar{\eta}})$ are modified Bessel functions of the first kind [94].

Remarkably, the aspect ratio in the long time limit saturates to a finite value different from 1, as shown in Fig. (3.8 b).

3.5.2 Tissue growth in 3d

In this section, we justify that the global picture obtained in the friction-dominated regime (i.e. $R \gg L_\eta$) for $2d$ systems does not change qualitatively in 3 dimensions. As in the $2d$ case, we assume that the flows inside the tissue are described by a Darcy law for an incompressible fluid

$$\xi \mathbf{v} = -\nabla P, \tag{3.52}$$

$$\nabla \cdot \mathbf{v} = k_c, \tag{3.53}$$

combined with the boundary condition at the surface $\partial\Omega$

$$P|_{\partial\Omega} = \gamma\kappa - \sigma_0 \hat{n}_x^2, \tag{3.54}$$

where κ is the total curvature in 3 dimensions. The x-axis is taken parallel to the preferential direction of cell orientation. The movement of the physical contour $\partial\Omega$ is defined by the kinematic equation $V_n = \mathbf{v} \cdot \hat{n}|_{\partial\Omega}$.

We base our analysis on the harmonic moment expansion formalism generalized to $3d$ systems [71]. In general, we consider a function $L(\mathbf{r})$, such that $\nabla^2 L = 0$. Then

$$\begin{aligned} \frac{d}{dt}\int_\Omega L(\mathbf{r})dv &= k_c \int_\Omega L(\mathbf{r})dv + \frac{\sigma_0}{\xi}\int_{\partial\Omega} \hat{n}_x^2 (\nabla L)\cdot\hat{\mathbf{n}}da & (3.55)\\ &- \frac{\gamma}{\xi}\int_{\partial\Omega} \kappa(\nabla L)\cdot\hat{\mathbf{n}}da. & (3.56) \end{aligned}$$

We use this result for an ellipsoidal boundary $(x^2/a(t)^2 + (y^2+z^2)/b(t)^2 = 1)$, where $a(t)$ and $b(t)$ are the instantaneous semi-axes, and for the functions $L_0(\mathbf{r}) = 1$ and $L_2(\mathbf{r}) = x^2 - y^2$, whose integral over the physical domain Ω are related to the volume and the anisotropy of the shape respectively. For the sake of simplicity, we limit the discussion to shapes close to spheres, and so the aspect ratio $H(t) - 1 = \mathcal{O}(\epsilon)$, where $\epsilon \ll 1$. We obtain

$$\begin{aligned} \frac{dR}{dt} &= \frac{k_c}{3}R, & (3.57)\\ \frac{dH}{dt} &= -\left(\frac{2k_c}{3} + \frac{4\gamma}{\xi R^3}\right)(H-1) + \frac{2\sigma_0}{\xi k_c R^2}. & (3.58) \end{aligned}$$

These equations are very similar to Eqs. (3.15-3.17) so that the scaling laws found in the friction regime for $2d$ system remain valid in 3 dimensions.

3.6 Conclusion

We have proposed a hydrodynamic model to study tissue morphogenesis. In a polarized tissue, the orientation of cell divisions leads to the existence of anisotropic active stresses that drive ellipsoidal shapes. The aspect ratio of the shape has two qualitatively different behaviours depending on the dominant dissipative mechanism, either viscous or drag forces. A single length scale arises from the comparison between these two forces. For viscosity-dominated growth, the anisotropy builds up monotonically, whereas during friction-dominated growth, it decreases after a transient time of the order of the cell division time. Consequently, the aspect ratio

in general shows a non monotonic behaviour, with a maximum at finite time, for which we give simple scaling laws which depend on the physical parameters of the tissue.

Acknowledgments:

The main part of this work has been carried out at the Institute Curie in two short stays, which were financially supported by the Short Visits Grants Program form Quantissue. We thank J.-F Joanny for collaborating in the work presented in this chapter.

Chapter 4

Mechanics and collective cell migration in epithelial monolayers

4.1 Introduction

The collective migration of epithelial monolayers requires the coordination of structural and mechanical changes within the cells that conform the tissue. This is a collective mechanical phenomenon that is involved in relevant biological processes, such as wound healing [102, 103, 104], cancer invasion [105] or tissue morphogenesis [32, 77, 106]. Thanks to the continuous improvements on imaging and detection techniques, in recent years significant progress has been achieved in our understanding of the interplay between cell and tissue mechanics. In controlled environments, the forces produced by epithelial cells onto the substrate can be measured [5, 107], which are transmitted across the monolayer via cell-cell junctions, [108]. These physical connections enable cells to interact, so that collective behavior emerges at the scale of the tissue, such as guidance mechanisms or mechanical oscillations [50, 51].

In this context, we take as a reference model system an epithelial cell monolayer. The purpose of this study is to provide a theoretical framework that can give a physical explanation of some collective mechanical phenomena recently discovered in these type of systems. We develop a coarse-grained, continuum description of an epithelial cell monolayer, based on the theory of active polar gels, [2, 3]. The inherent complexity of individual cells is then effectively encoded in a set of characteristic phenomenological parameters. This approach is in line with a common strategy in the physical enquiry of biological mechanics, where the system is treated as an effective medium and the focus is on elucidating the basic mechanisms that control the phenomena, which may then be generalizable. In the case of a cell monolayer, we assume in addition that this medium can be

treated as effectively two-dimensional by means of a lubrication approximation, and accordingly, that the advance or expansion of the monolayer is driven by the active traction forces produced by the cells.

The presentation of this study is divided in three parts. First, we will construct the formal basis of the physical model and test a minimal version of it that will be sufficient to capture the first order variability observed in the stress profiles of epithelial monolayers [51]. Then we will generalize this minimal model in the direction of incorporating the contractility of the cytoskeleton, which will play a major role in the mechanical oscillations observed in expanding epithelial monolayers, and construct a global phase diagram that classifies the asymptotic mechanical states of the system. Finally, we will explore briefly the $2d$ physical patterns trying to address the underlying principles in the vortex-like migratory mode in MDCK cells [109].

4.2 Theoretical description of an epithelial cell monolayer

In this section, we present the physical model proposed to describe an epithelial cell monolayer in the experimental conditions of Ref. [5, 50, 51]. We will treat the system as a thin layer of active polar viscous material placed on top of a substrate, as depicted in Fig. (4.1). Therefore we will consider only two main physical observables: the velocity field $\mathbf{v}$ and the polarization field $\mathbf{p}$. The former can be accessed experimentally via PIV methods, whereas the latter might be inferred from estimates such as the aspect ratio of cells or the orientation of stress fibers within cells. We assume that cells have only one preferred orientation that is parallel to the substrate plane.

With respect to the density of cells, we consider that during the experimental time window the number and volume of cells is preserved. The experimental observations on expanding MDCK cell monolayers from Ref. [51] point out that less than 50% of the total area increase at ~ 600 min is due to cell proliferation. The expansion of the monolayer area is thus mainly due to changes in the thickness of the monolayer, as the cells rearrange. Nevertheless, the effects of cell division on the mechanics of the system may become dominant at longer time scales ($>$ day). We investigate in Chapter 3 the morphologies of fully polarized tissues growing by means of cell division.

We take a thin layer approximation, by considering that the height of the monolayers (~ 10 μm) is smaller than the spatial variations of the physical observables on the tangential plane to the substrate (~ 50 μm). Under this hypothesis, one

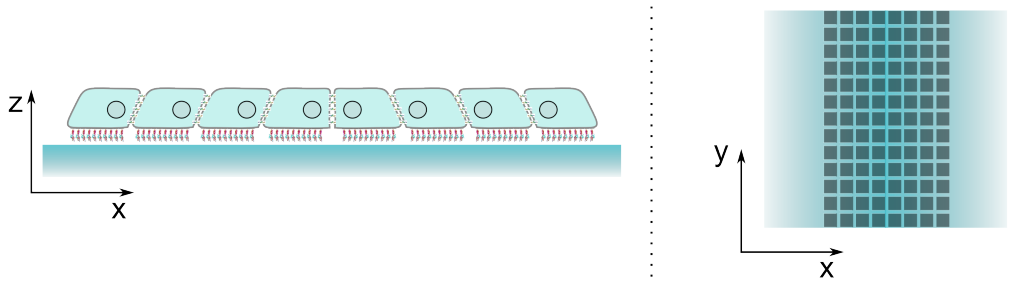

Figure 4.1: Schematic drawing of an epithelial monolayer in space. Cells are placed on top of an elastic substrate and are able to form cell-cell and cell-substrate junctions. The monolayer has a rectangular shape. For more details on the experimental conditions, see Ref. [51]

can describe the monolayer as an effective $2d$ system, in which the physical observables are averaged along the third direction. For simplicity, we will reflect this point in the notation. Accordingly, the traction forces exerted by the cells onto the substrate ($\mathbf{T}$), which by the third Newton's law are reflected back onto the monolayer, are balanced by the averaged internal stresses (i.e. intracellular forces)

$$\partial_x \sigma_{xx} + \partial_y \sigma_{xy} = T_x, \tag{4.1}$$

$$\partial_x \sigma_{yx} + \partial_y \sigma_{yy} = T_y, \tag{4.2}$$

where σ_{xx}, σ_{xy}, σ_{yx} and σ_{yy} are the components of the averaged total stress tensor, which in general depends on the microscopic properties of the cell. For more, details see Appendix 7.6.

Here we model the tissue as a one-component active polar fluid and base our study on the formalism described in Refs. [2, 3]. With respect to the assumption on the rheological properties of the epithelial monolayer, two comments are in order:

1. The typical duration of the experiments we want to model is around 15 hr. In Ref. [83] it was demonstrated that even if a tissue is modeled as an linear elastic material, at time scales longer than the cell division cycle, it behaves as a fluid with an effective viscosity. This result was validated by numerical simulations of a microscopical model of a tissue [83]. In our case, even though we have not considered cell division, this result still sets an upper bound for the viscoelastic relaxation time scale of the system of the order of ~ 1 day.

2. On the other hand, we assume that the energy dissipation in the system takes place mainly in the cell-cell junctions, whose typical turnover time is

estimated to be $\sim 1-10$ min by FRAP experiments [110, 111]. In addition, we assume that as the monolayer spreads, the cells do not offer resistive nonlinear elastic-like forces in response to elongation. On the contrary, we assume that cells are able to accommodate the volume as if they were viscous drops. The redistribution of the internal cell components, produces a certain additional dissipation of energy that may add up with the one associated to the cell-cell junctions. Under the last assumptions, the system is expected to behave as a fluid at time scales longer than the turnover time of cell-cell junctions.

The cells that conform the monolayer are considered polar and active as well. One of the characteristic landmarks of living matter is its capability to transform chemical energy into mechanical action. In our case, part of this chemical energy is converted into traction forces, which can be measured via Traction Force Microscopy, [5]. These forces are pointing inwards with respect to the main front of the monolayer (i.e anti-parallel to the direction of migration), which is a strong indication that the machinery in charge of producing them relies on polarity (see Fig. (4.1)).

It is worth remarking that the thin layer approximation described in Appendix 7.6 permits to eliminate the pressure field on the equations of momentum conservation. The pressure acts as a Lagrange multiplier that enforces the constraint of volume conservation of the cell volume. In our effective $2d$ description, however, the total area occupied by the monolayer is not conserved, as a consequence of variations of the monolayer thickness in time and space.

On the other hand, it is necessary yet another equation to describe the dynamics of cell orientation ($\mathbf{p}$). Following Refs. [2, 3], we choose the term of the free energy associated to the passive nematic properties of the system to be

$$\mathcal{F} = \int d\mathbf{r} \left(\frac{\rho}{2} p^2 + \frac{K}{2} (\partial_\alpha p_\beta)(\partial_\alpha p_\beta) \right), \tag{4.3}$$

where α and β run over the two cartesian coordinates. From now on, we use the Einstein summation convention over repeated Greek indices.

Along this chapter, ρ will be taken as negative unless stated otherwise. This choice favors energetically the isotropic phase. In the context of the epithelial monolayer, this means that in the absence of external stimuli, the cells at the interior of the monolayer are randomly oriented, which might be the case in the experiments that we are aiming to model [5, 51]. The second term in the free energy $\mathcal{F}$ introduces the energetic penalty to the spatial inhomogeneities of the orientational field. The relative weight on the total energy of these two contributions is controlled by two parameters ρ and K, whose ratio has units of length

square. Accordingly, we define the length $L_c^2 = K/\rho$, which will be called the nematic correlation length, and will play a key role in our analysis.

The equation governing the temporal evolution of the orientational field reads

$$\frac{Dp_\alpha}{Dt} = \frac{1}{\gamma_1} h_\alpha - \nu_1 v_{\alpha\beta} p_\beta = \frac{\rho}{\gamma_1} \left(-p_\alpha + L_c^2 \nabla^2 p_\alpha \right) - \nu_1 v_{\alpha\beta} p_\beta, \tag{4.4}$$

where $Dp_\beta/Dt = \partial_t p_\beta + v_\alpha \partial_\alpha p_\beta + \omega_{\alpha\beta} p_\beta$ is the co-rotational convected derivative, being $\omega_{\alpha\beta}$ and $v_{\alpha\beta}$ the antisymmetric and symmetric part of the strain rate tensor, respectively.

The quantity $h_\alpha = -\frac{\delta \mathcal{F}}{\delta p_\alpha}$ is the so-called molecular field, which is the term that drives the polarization field to the minimal energy configuration. The relaxation time scale is proportional to the ratio $\bar{\gamma}_1 \equiv \gamma_1/\rho$, being γ_1 the rotational viscosity. We consider an extra term $(\nu_1 v_{\alpha\beta} p_\beta)$, which allows a reorientation of the cells driven by the local stresses on the monolayer and will play a key role in our analysis. This term has not been invoked in other theoretical studies of epithelial cell monolayers, [112, 92]. In addition, in Ref. [113] a cellular mechanism that aligns cells to the local velocity field was proposed. It is important to remark that this study considered a mechanism for cell orientation, with no counterpart in liquid crystal systems, and so we conjecture that ν_1 might take significantly different values in our biological context. This point will be further discussed in (Sec. 4.4.3). Alternatively, in Ref. [114] experimental evidence was reported that suggests that cells polarize and generate traction forces opposite to the pulling applied external forces (see Fig. (4.2)), which may extrapolated to the cell sheet.

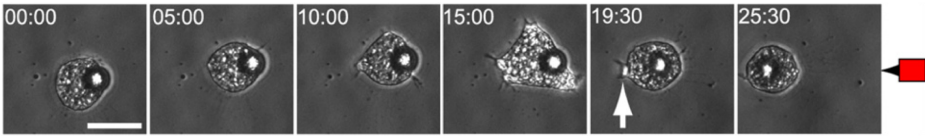

Figure 4.2: A single multipolar mesendoderm cell plated on FN in contact with a C-cadFc bead pulled by a magnet (red magnet icon). A lamellipodium forms (arrow) opposite the direction of bead pull and results in directed cell migration. Modified from Ref. [114].

Finally, in order to close the model it is necessary to propose an explicit form for the total stresses tensor. Following the standard procedure in irreversible thermodynamics and as commonly assumed in active gels theory [2, 3], we will assume a linear relationship between fluxes and forces, that is, between the total stresses are the corresponding generalized forces (i.e the symmetric part of the strain rate tensor $(v_{\alpha\beta})$, the chemical difference between ATP and the product molecules ADP and P_i, $\Delta\mu$ and the molecular field $\mathbf{h} = -\frac{\delta \mathcal{F}}{\delta \mathbf{p}}$) provided that the fundamental symmetries of the system are preserved. In each section, we will

explicitly detail the functional form of the total stress tensor.

Cell-generated traction forces

Let us first make some comments on the traction forces. As it was stated in Section 4.2, in experimental conditions either with micro-pilars arrays or polyacrylamide gels, these forces can be measured via Traction Force Microscopy, [5, 109]. In our theoretical description of epithelial cell monolayers we need to impose a certain functional form of these traction forces in terms of the physical observables, which we take of the form

$$\mathbf{T} = \xi \mathbf{v} - T_0 \mathbf{p}. \tag{4.5}$$

This ansatz was previously proposed to study the same system by [92, 115], as well as for bacterial suspensions by [116]. The above expression of the traction forces can be separated in two parts:

1. The term $\xi \mathbf{v}$ corresponds to a friction drag force arising from the relative motion between the cell sheet and the substrate, which are weakly linked by transmembrane proteins, such as integrin [117]. The coefficient ξ plays the role of a friction coefficient. For the sake of simplicity the drag force is assumed to depend only on the local velocity of cells in our coarse-grained picture, because we assume that the turnover time associated to cell-substrate adhesions is smaller compared to the experimental time window and also that the deformations over the turnover time of such proteins are not too pronounced. The estimated turnover time of the integrin is ~ 1 min, [118], and so the characteristic transversal stretching is of the order of 100 nm, provided that the typical cell velocity is 0.1 μm/min.

2. On the other hand, the term $-T_0 \mathbf{p}$ is an active term. $T_0 > 0$ is associated to the maximum active traction force per cell. It reflects the capability of cells to grab and pull the substrate. Importantly, the fact that is linearly related to the local cell orientation ($\mathbf{p}$) allows to treat in a distinct way the direction at which cells exert forces from the direction at which they move, as in Ref. [113]. The main force-generating mechanisms for cells are lamellipodia via internal actin flow and stress fibers via molecular motors contraction. It is worth remarking that the last term is consistent with the fundamental symmetries of active polar gels theory [119].

4.3 Semi-infinite rectangular geometry

In this section, we start explaining in detail the characteristic stress profiles predicted by a simplified version of the physical model presented in Section 4.2. Afterwards, we will compare the theoretical predictions with experimental data provided by X. Trepat's group of the spatio-temporal stress and velocity profiles for two type of cells: MDCK and MCF10a.

4.3.1 Effective 1d model

We will assume that the cell sheet is a semi-infinite rectangle with a finite width $2L$ and is symmetric with respect to the long midline. Then, the boundaries of the monolayer are labelled by $x = L$ and $x = -L$. Consequently, the system is translationally invariant in the transversal direction, that is the physical observables will not depend on the y cartesian coordinate.

With respect to the constitutive laws of the material, the total stress on the tissue will be given by the relation $\sigma_{\alpha\beta} = \eta v_{\alpha\beta}$ with a single effective viscosity η, being $v_{\alpha\beta}$ the symmetric part of the strain rate tensor. The intracellular forces within the cohesive tissue balance the cell traction forces $\mathbf{T} = \xi\mathbf{v} - T_0\mathbf{p}$. In the absence of viscous drag force the monolayer is under tension, [51].

The system exhibits two different dissipative mechanisms: viscous and friction forces. From the comparison between these two passive forces, one can define the friction length $L_\eta \equiv \sqrt{\eta/\xi}$. Typically viscous forces dominate at length scales $< L_\eta$, on the contrary friction forces become relevant at length scales $> L_\eta$.

With respect to the orientational field, we approximate Eq. (4.3) by $0 = -\mathbf{p} + L_c^2\nabla^2\mathbf{p}$. Estimations on the relaxation time scale of cell polarization $\bar{\gamma}_1 \sim 10 - 100$ min, [92, 114]. Therefore, since the expansion of the monolayer lasts around 900 min, this approximation is crude, but it simplifies the analysis.

In summary the model used along this section is given by the system of ODE's

$$\sigma_{xx} = \eta\partial_x v_x, \tag{4.6}$$

$$\partial_x\sigma_{xx} = \xi v_x - T_0 p_x, \tag{4.7}$$

$$0 = -p_x + L_c^2\partial_x^2 p_x. \tag{4.8}$$

Combined with stress-free boundary conditions at the edges of the cell sheet and the condition that cells are oriented outwards of the boundaries (i.e $\sigma_{xx} = 0|_{x=\pm L}$, $p_x = 1|_{x=L}$ and $p_x = -1|_{x=-L}$).

Then the system has two characteristic length scales L_c and L_η, no characteristic time scale and a single source of energy represented by the external force

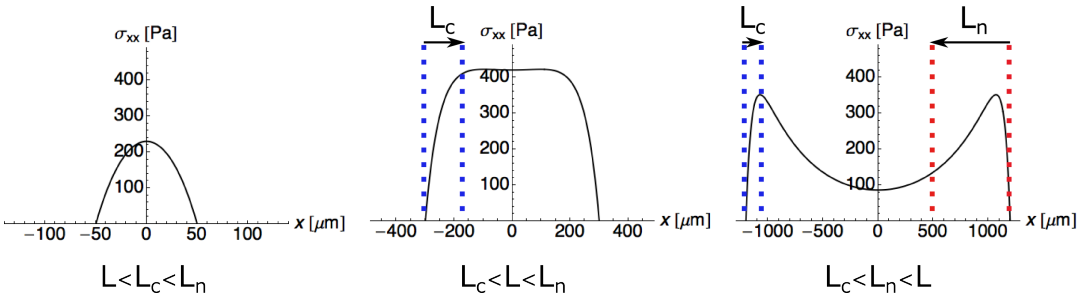

Figure 4.3: Stress profiles at different regimes. The values of the parameters are $\eta = 24 * 10^6$ Pa·s, $\xi = 100$ Pa·s/μm^2, $L_c = 50$ μm, $T_0 = 10$ Pa/μm and L varies between 50 μm (left), 300 μm (center) and 1200 μm (right).

proportional to T_0. In principle the only parameter that may change over time is the width of the monolayer. Therefore, there are three differentiated regimes as a function of the width of the cell sheet with respect to the rest of characteristic lengths, as shown in Fig. (4.3)

1. In the regime where $L < L_c < L_\eta$, viscous forces predominate over the passive friction forces throughout the monolayer and balance the active traction force. Nevertheless, all the cells are significantly polarized and contribute to the build up of stress in the monolayer. The spatial stress profile has a parabolic shape being the maximal value of the stress $\propto T_0 L$.

2. In the regime where $L_c < L < L_\eta$, the viscous forces still predominate over the friction forces within the monolayer, however now only the cells separated a distance smaller than L_c from the boundaries are polarized, and do perform active traction forces. The rest of the cells on the monolayer are randomly oriented but still move collectively towards the edges. In this case, the stress profiles exhibit a monotonic increase in the spatial coordinate from the edges towards the centre, followed by a plateau at the centre of the monolayer. The maximal value of the stress is $\propto T_0 L_c$.

3. In the regime where $L_c < L_\eta < L$, the monolayer is separated in two domains: one in a band of thickness L_η from the edges, in which viscous forces predominate over the passive friction forces, and the other, in which the role of the passive forces is exchanged, occupying the rest of the tissue. One of the consequences is that the internal stress starts to depend non-monotonically with the spatial coordinate. The stress profile has a characteristic double-peak shape with a central region where the cells are nearly static. As in the previous regime, only the cells within a distance L_c from the edges are able to perform active traction forces.

4.3.2 Physical interpretation and orders of magnitude of the parameters

The previous physical model has four parameters: T_0, L_c, η and ξ. In the following sections we will discuss how these parameters allow to interpret the complex spatio-temporal evolution of the stress and velocity profiles in expanding cell monolayers. But before, it is worth discussing in more detail their physical interpretation and the typical values that one extracts from the cells (see Fig. (4.4)).

- T_0 quantifies the strength of the active traction forces performed by individual cells. The main mechanisms to generate them is either via the lamellipodia developed by epithelial cells during the monolayer expansion or via the contraction of stress fibers anchored to the focal adhesions, [120]. The order of magnitude is expected to be around ~ 10 Pa/μm.

- L_c quantifies the spatial correlations of cell orientation. The range of values for this parameter is estimated to be between $\sim 10 - 100$ μm. A long-range mechanical mechanism by which cohesive epithelial cells might align, involve stress fibers together with the cell-cell adhesions connecting stress fibers from neighboring cells. In Ref. [51], the formation of stress fibers was imaged within the first 100 min, which is temporally correlated with the build up of tension within the monolayer. Consequently, in this context the nematic correlation length may depend on the mean stress fibers length as well as the strength of the links between stress fibers, [120].

- η is thought to be an effective viscosity of the expanding epithelial monolayer at time scales > 10 min. We conjecture that the viscous stresses are originated by the remodelling of cell-cell adhesions, that at time scales longer than 10 min allows cell rearrangements within the tissue. The order of magnitude is estimated to be $\eta \sim 10^6$ Pa·s

- ξ is a friction coefficient connected to the physical properties of cell-substrate adhesions. Its value is estimated to be around $\xi \sim 100$ Pa·s/μm^2. It provides an additional dissipative mechanism on the tissue. However, their effects are barely seen in the experimental conditions presented below, probably due to the fact that the width of the epithelial monolayer is not sufficiently large.

Finally, we stress that there are protein pathways by which the different cell components mentioned above can be upregulated or downregulated during the cell sheet expansion [121]. For instance, it has been reported a recruitment of cadherin proteins at the contact region of stretched cell doublets [118].

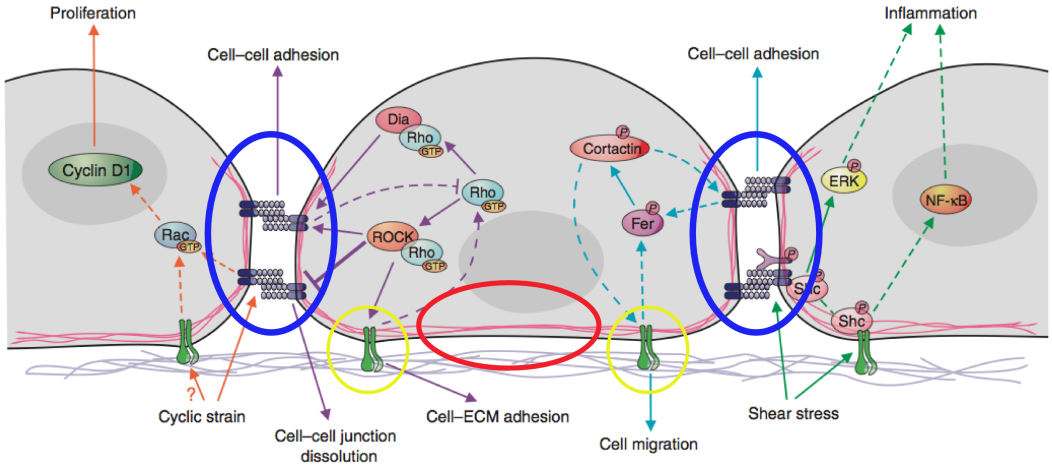

Figure 4.4: Molecular mechanisms for integration of adhesive signals. Solid lines represent direct interactions or effects, dashed lines indicate an indirect or unknown mechanism. The extracellular matrix is shown beneath the cells in blue and the actin cytoskeleton is represented by the pink lines. Modified from Ref. [121]. The red circles highlights stress fibers, the yellow circle cell-substrate adhesions and the blue circle cell-cell adhesions.

4.3.3 Predicted stress and velocity profiles

In this part, we will compute the stress and velocity profiles predicted from the model described at the beginning of Section 4.3. The analytical curves of these physical observables are afterwards compared with the ones measured by X. Trepat's group.

We assume that the monolayer is a symmetric semi-infinite rectangle with a finite width $2L$. The two boundaries of the monolayer are parametrized as $x = L$ and $x = -L$. In addition, we assume that the system is translationally invariant along the transversal direction, and so the physical observables do not depend on the y cartesian coordinate, Fig. (4.1). The physical model is given by Eqs. (4.6-4.8) with stress free boundary conditions at both edges of the monolayer (i.e $\sigma_{xx} = 0|_{x=\pm L}$) and the cell's polarization is pointing perpendicularly to the free boundaries (i. e. $p_x = 1|_{x=L}$ and $p_x = -1|_{x=-L}$). Under these hypothesis the explicit solution of the equations takes the form

$$\sigma_{xx} = T_0 \frac{L_c L_n^2}{L_c^2 - L_\eta^2} \left(\frac{\cosh\left(\frac{x}{L_c}\right)}{\sinh\left(\frac{L}{L_c}\right)} - \frac{\cosh\left(\frac{L}{L_c}\right)\cosh\left(\frac{x}{L_\eta}\right)}{\sinh\left(\frac{L}{L_c}\right)\cosh\left(\frac{L}{L_\eta}\right)} \right), \tag{4.9}$$

$$v_x = \frac{T_0}{\eta} \frac{L_c L_\eta^2}{(L_c^2 - L_\eta^2)} \left(L_c \frac{\sinh\left(\frac{x}{L_c}\right)}{\sinh\left(\frac{L}{L_c}\right)} - L_\eta \frac{\cosh\left(\frac{L}{L_c}\right)\sinh\left(\frac{x}{L_\eta}\right)}{\sinh\left(\frac{L}{L_c}\right)\cosh\left(\frac{L}{L_\eta}\right)} \right). \tag{4.10}$$

The point $x = 0$ defines the midline of the cell sheet.

In Fig. (4.5) we plot a family of stress profiles varying the parameters in a realistic range. It is important to remark that within this region of the parameter space, the latter expressions capture all the phenomenology observed in the shapes of the stress profiles.

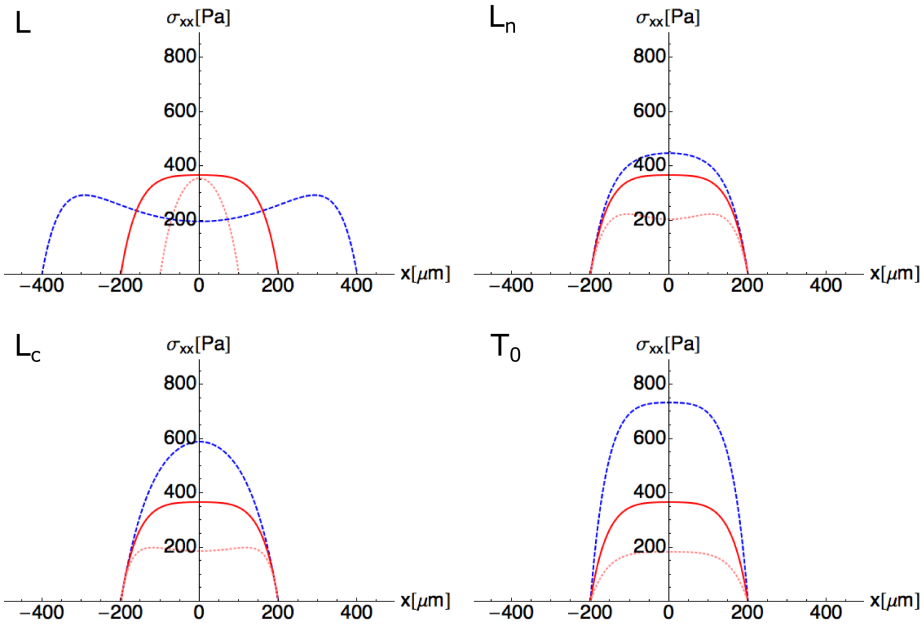

Figure 4.5: Representative stress profiles for realistic parameters. The reference values of the parameters for the stress profiles (4.9) are: $T_0 = 10$ Pa/μm, $L_c = 50$ μm, $L_\eta = 250$ μm and $L = 200$ μm, corresponding to solid red curve. The dashed blue (dotted pink) curve has the parameter, labelled at the top left side of each figure, doubled (halved).

Nevertheless, in realistic conditions the friction length is usually larger than the width of the system, ($L_c < L \ll L_\eta$). Consequently, without losing too much detail the latter expressions can be simplified to gain better insights on the physics of the system. Therefore, in the limit of negligible friction the stress and velocity profiles can be approximated to

$$\sigma_{xx} \approx T_0 L_c \left(\frac{\cosh\left(\frac{x}{L_c}\right)}{\sinh\left(\frac{L}{L_c}\right)} - \frac{\cosh\left(\frac{L}{L_c}\right)}{\sinh\left(\frac{L}{L_c}\right)} \right), \tag{4.11}$$

$$v_x \approx \frac{T_0 L_c}{\eta} \left(L_c \frac{\sinh\left(\frac{x}{L_c}\right)}{\sinh\left(\frac{L}{L_c}\right)} - L \frac{\cosh\left(\frac{L}{L_c}\right)}{\sinh\left(\frac{L}{L_c}\right)} \right). \tag{4.12}$$

4.3.4 Comparison with experiments

In this section we perform a detailed comparison between the physical model presented above and the profiles of stress and velocity measured experimentally in expanding epithelial monolayers. We apply a simple fitting technique to extract an estimated set of parameters at each time point. The experimental measurements were carried out by E. Bazellières and X. Serra-Picamal and the data was processed by R. Vincent, all of them from the group of X. Trepat.

Our objective is to provide a simple interpretation of the temporal behaviour of the effectively-$1d$ mechanical profiles in expanding epithelial monolayers at very long time scales. Each cell in the monolayer produces measurable traction forces on a collagen-coated polyacrylamide gel, that are balanced through the intracellular forces at the cell-cell junctions with the neighboring cells. This mechanism allows a large-scale stress build up extending throughout the monolayer [5] and at the same time controls the collective migration of cells [50]. It is interesting to stress that this mechanism yields an emerging collective effect that cannot be reduced to the detailed structure and mechanics of individual cells.

To study this collective dynamics, a polydimethylsiloxane (PDMS) membrane was fabricated with a rectangular opening and deposited on a polyacrylamide gel that had been coated with collagen I. The gel contains a homogeneously distributed solution of 200-nm-diameter red fluorescent carboxylate-modified beads. Then 20.000 cells were seeded on the exposed region of the polyacrylamide gel defined by the PDMS membrane. Twelve hours after seeding the cells, the PDMS membrane was carefully removed, triggering the collective cellular migration towards the newly available free space. Then, 30 minutes after that, the expansion of the monolayer was recorded during 15 hours approximately. For more details on the specific protocols, we refer the reader to Ref. [51].

The image analysis was performed at time intervals of 3 minutes. The velocity fields were computed via a particle image velocimetry software. Alternatively, the traction force maps were computed via Fourier Transform traction microscopy with a finite gel thickness. The displacements of the beads contained in the gel were recorded during the tissue expansions and the reference positions were measured after monolayer trypsinization, allowing to obtain from both measurements the gel displacements with which cell traction maps are computed.

Following the configuration depicted in Fig. (4.1) and using the above techniques, the traction force maps (i.e T_x and T_y) are reconstructed at each time point. As shown in Ref. [5], the spatial average along the transversal y-axis over the field of view of $\langle T_y \rangle$ is nearly zero, although both T_x and T_y display non-Gaussian distributions. Assuming that the system is effectively $1d$, a straightforward application of the Newton's third law permits to compute the stress component $\langle \sigma_{xx} \rangle$

at position x, as the sum of the traction forces T_x from the free edge $x = -L$ to the point x, in other words the force balance demands that

$$\sigma_{xx}(x) = \frac{1}{h_z h_y} \int_{-L}^{x} \int_{0}^{h_y} T_x(x', y') dy' dx' \tag{4.13}$$

where the cell height h_z is taken as a constant value of 5 μm and h_y is the length of the field of view.

We analyze two types of epithelial cells: MDCK and MCF10a. For each case the number of experiments analyzed were 4. On the other hand, we also analyzed the case of Blebbistatin and HGF treated MDCK cells, with one experiment for each. HGF or hepatocyte growth factor is known to promote motility and to favor individual versus collective behavior [122], and Blebbistatin is an inhibitor of myosin II [123].

It is important to remark that the measurements of the stress profiles are independent of the rheological properties of the material, given the external forcing T_x. However, it is necessary to specify the rheology of the material to provide a relation between the stress and the velocities, such as Eqs. (4.9-4.10).

In general the spatial profiles of the physical observables change over time as the monolayer expands. In order to capture at this ultraslow time scales the temporal behaviour of the system, we developed a simple method explained in Appendix 7.7. In essence, it consists on finding an optimal fit of the analytical curves of the stress and velocity profiles given by Eqs. (4.9-4.10), with respect to the experimental data (as shown in Fig. (4.6)). Interestingly, this method allows one to extract an estimation of the effective physical parameters at every instant of time. Therefore, it is possible to reconstruct the temporal evolution of the mechanics of the expanding epithelial monolayers from the trajectories of a reduced set of four parameters: active traction force T_0, nematic correlation length L_c, effective viscosity η and friction coefficient ξ.

The fact that the effective material parameters of the tissue vary over time may be related to due to a variety of reasons. On the one hand, it may be related to the changes in thickness of the monolayer, which in turn may affect the contact surface between cells and their associated forces. On the other hand, the mechanical environment of the cells may also trigger signaling pathways that result in changes on the individual properties of the cells. The temporal evolution of the estimated values of the effective parameters of the tissue can be seen in Fig. (4.7).

We do not present the estimated trajectories of the viscous length L_η or equivalently ξ, because usually the stress profiles are in the range $L \ll L_\eta$ and the fitting method is not able to compute L_η within a reasonable accuracy.

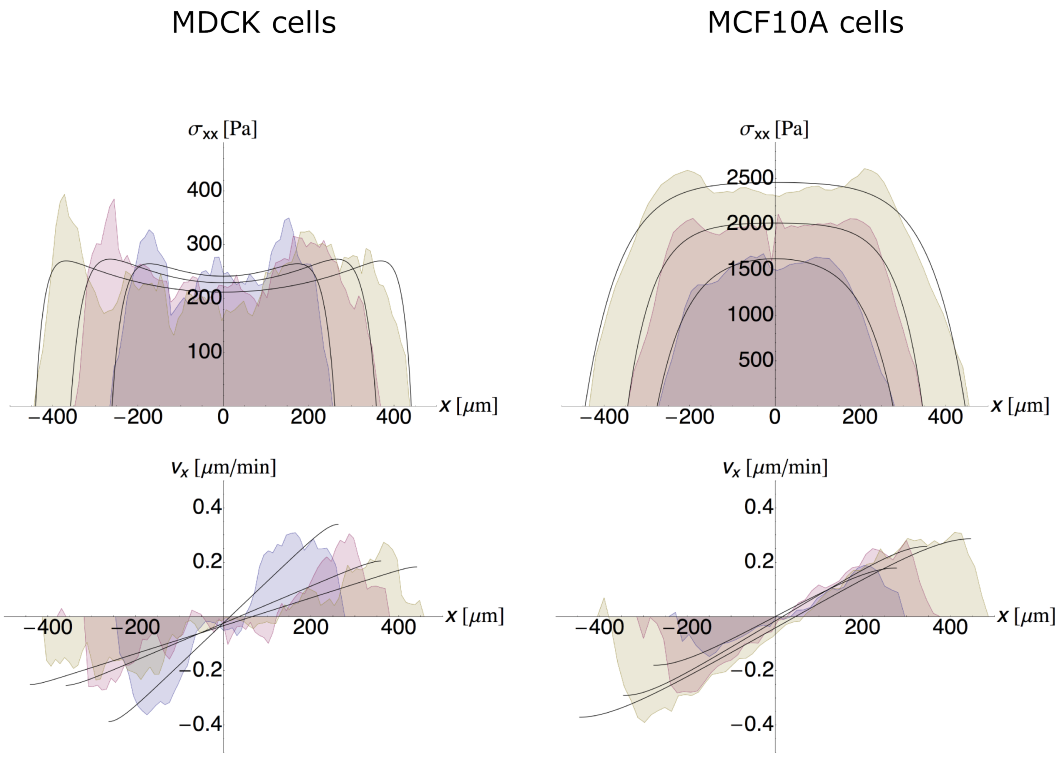

Figure 4.6: Temporal evolution of the stress profiles in expanding epithelial monolayers. The left (right) hand side shows the case of MDCK (MCF10a) cells. At the upper (bottom) row, the bluish, pinkish and yellowish coloured areas correspond to the stress (velocity) profiles at the time points: 200, 400 and 600 minutes, respectively. The solid black curves correspond to the analytical curves fitted to the experimental data at each time points.

In Fig. (4.7.a), we can observe the different trajectories of T_0. Cells have two main mechanisms by which they can produce active traction forces: the internal retrograde flow of lamellipodia and the contraction of the stress fibers anchored in the focal adhesions. HGF promotes actin dynamics, and so it might reinforce the actin-based traction forces in the system, however we do not appreciate substantial differences with respect to the control MDCK cells. Conversely, T_0 decreases notably in the case of cells treated with Blebbistatin, around 1 Pa/μm. This suggests that the main mechanism by which the cells produce traction forces is myosin-based.

With respect to the nematic correlation length in Fig. (4.7,b) all the curves seem to have a tendency to increase monotonically in time, meaning that the number of cells producing traction forces increases with time, except for the case of MCF10a. We associate the apparent decrease of L_c at the first 200 minutes to

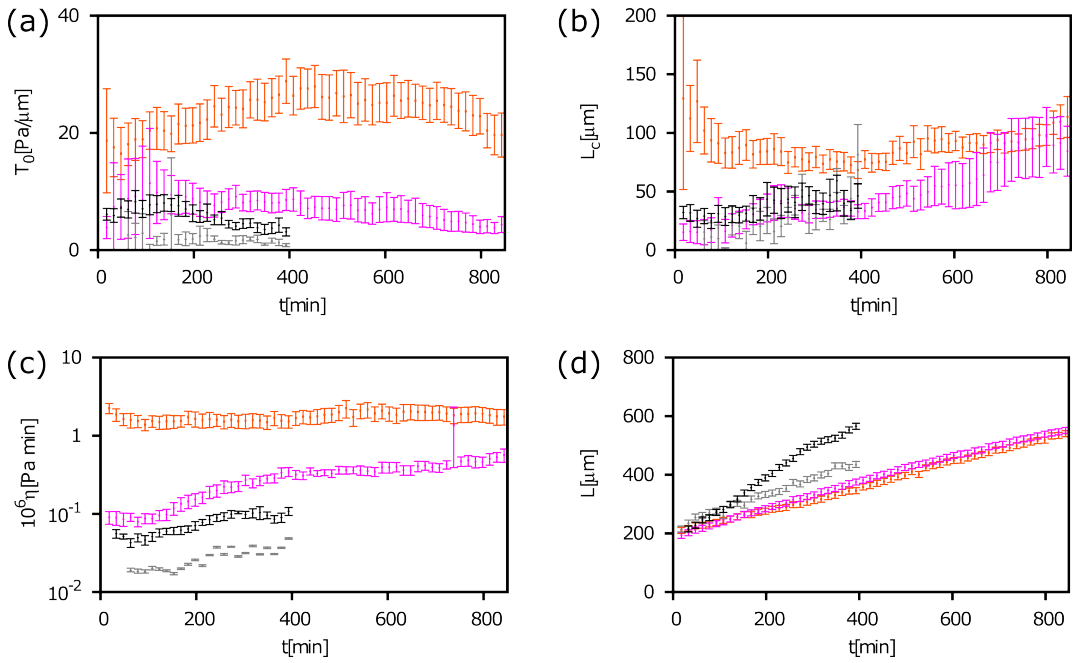

Figure 4.7: Temporal evolution of the estimated physical parameters. (a) The active traction force T_0, (b) the nematic correlation length L_c, (c) the effective viscosity η and (d) the half of the monolayer's width L as a function of time. The orange, pink, tray and black points correspond to the cases: MCF10a cells, MDCK cells, HGF-treated MDCK cells and Blebbistatin-treated MDCK cells. The error bars are the quadratic sum of the standard deviation between realisations and the mean of the numerical standard error from the estimated parameter.

the large experimental uncertainty, due to the fact that $L \sim L_c$ at the beginning of the expansion of an MCF10a epithelial monolayer. Interestingly, the curves can be grouped in both classes of cells.

With respect to the effective viscosity η in Fig. (4.7.c), one can see that the cases analyzed cover a broad range of values of several orders of magnitude. On the one hand, the viscosity of MDCK cells is one order of magnitude larger than the same cells treated with Blebbistatin. In a model system of the cytoskeleton, the dramatical changes in the rheological properties induced by the activity of these molecular motors were already evidenced [124]. Similarly, the effective viscosity of HGF-MDCK cells is lower than the control case. Interestingly, the tendency to increase of the viscosity in time is more accentuated for MDCK cells, with a relative increase of the 40% during the first 400 minutes. As a consequence, these cells do not behave as a Newtonian fluid at these time scales [51]. The temporal evolution of the apparent viscosity in this first regime is similar to the ratio between the stress (σ_{xx}) and the deformation rate (v_{xx}) of a Kelvin-Voigt material subject to a constant deformation rate, which is constituted by a viscous damper (η) connected in parallel to an elastic spring (E) (i.e $\sigma_{xx}/v_{xx} = \eta +$

Et). Fitting the latter expression, we obtained an elastic spring constant of $\sim$ 800 Pa. However, it is worth stressing that the activity of the cells might also account for these non-Newtonian effects. In Ref. [8], the response of an active suspension to shear stresses is studied, showing that there are differences between the apparent viscosity and the intrinsic viscosity of the material. The activity may change notably the mechanical response of the system, inducing for instance active thinning or thickening effects. Alternatively, the effective viscosity of actin networks subject to extensional stress exhibits two distinct regimes separated by a critical value of the stress that depends on the force-extension behavior of the actin subunits [125]. For sufficiently small applied stresses, the actin network is in the linear rheology regime, whereas for extensional stresses above a certain threshold, the apparent viscosity increases monotonically as a function of the applied stress [125]. These active mechanisms may account for the non-Newtonian effects in MDCK monolayers. Finally, the effective viscosity of MCF10a cell sheets remains approximately constant around the value of 10^6 Pa·min, so that it remains close to a Newtonian fluid.

4.3.5 Morphological instability of the leading edge

Commonly the expanding cell sheets display finger-like protrusions at the free edges [126]. In this section, we will show that the present simplified model incorporates a morphological instability that is reminiscent of the Viscous-Fingering-like instability in cell fragments Ref. [55]. The study that we propose is a linear stability analysis on the reference rectangular system Fig. (4.1). For simplicity we will focus on perturbations that preserve the mirror image symmetry of the system with respect to the midline.

The model that we use to describe the epithelial cell monolayer is the extension to $2d$ of the one given by Eqs. (4.6-4.8). Therefore the force balance equations read

$$\begin{aligned} \partial_x \sigma_{xx} + \partial_y \sigma_{xy} &= \xi v_x - T_0 p_x, \\ \partial_x \sigma_{yx} + \partial_y \sigma_{yy} &= \xi v_y - T_0 p_y. \end{aligned}$$

For simplicity, we will assume that the total stress is symmetric and $\sigma_{\alpha\beta} = \eta\left(v_{\alpha\beta} + v_{\gamma\gamma}\delta_{\alpha\beta}\right)$, being $v_{\alpha\beta}$ the symmetric part of the strain rate tensor. The model is completed with the equilibrium equation of the cell polarity field $\mathbf{p} - L_c^2\nabla^2\mathbf{p} = 0$. At the edges we assume stress-free boundary conditions and that the cells are oriented perpendicularly, pointing outwards from the edges.

The free-interfaces are parametrized by $x = L + \epsilon a_q(t)e^{iqy}$ and $x = -L - \epsilon a_q(t)e^{iqy}$, being $\epsilon \ll 1$ a dimensionless book-keeping parameter and $a_q(t)$ the

complex amplitude of a q-sinusoidal perturbation. In the case $\epsilon = 0$, one recovers the solution presented above (4.9-4.10). It is worth reminding that the cell sheet expands at a speed that depends monotonically on the actual width of the monolayer.

On the other hand, by solving the same problem at linear order in ϵ, one can obtain a dynamical equation for a_q of the form $\dot{a}_q = \omega(q)a_q + \mathcal{O}(\epsilon^2)$, which is controlled by a single characteristic rate $\omega(q)$ that in general varies with the wavenumber q. Therefore, if $\omega(q) > 0$ (< 0), the amplitude of the q-sinusoidal perturbation would grow (decrease) exponentially in time. In Fig. (4.8), we display the behavior of ω as a function of the wavenumber for a set of realistic parameters for MDCK cells.

A first remark is that at $q = 0$, $\omega(q = 0) \neq 0$. This expresses that the velocity of the edge is not constant and fixed by some conservation law of the system. In our case, the cell sheet is expanding and in addition the expanding velocity increases with the width of the system, (i.e. $\omega(q = 0) > 0$). The apparent lack of mass conservation is mostly due to the change of thickness of the monolayer.

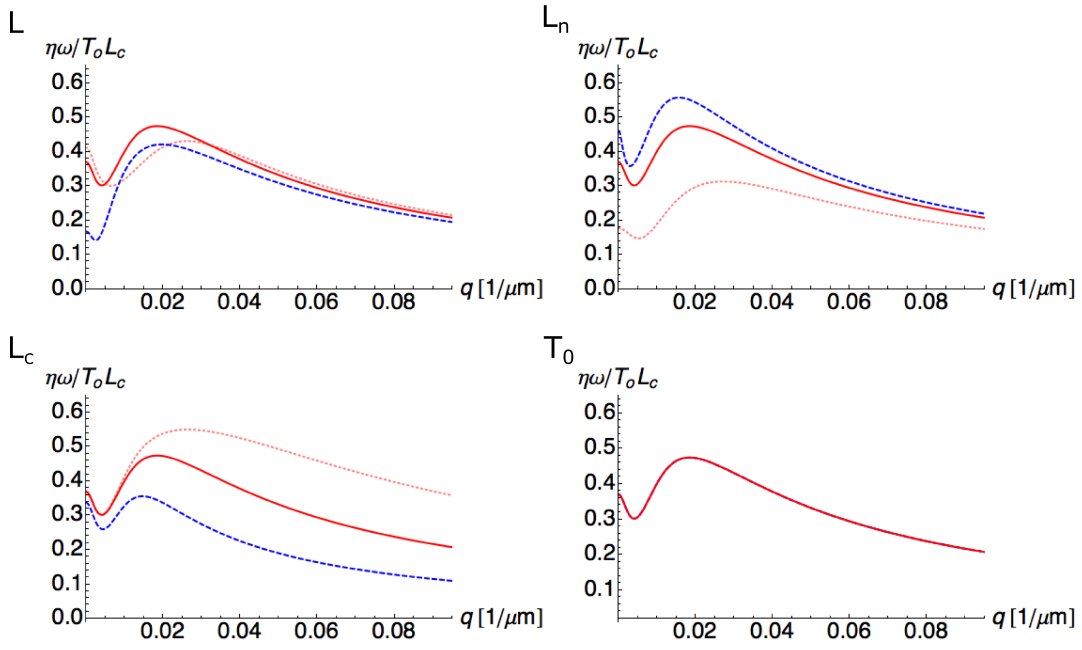

Figure 4.8: Characterisation of the linear dynamics of the perturbations at the edges of an expanding cell monolayer. The reference parameters for the solid red curve are $T_0 = 10$ Pa/μm, $L_c = 50$ μm, $L_\eta = 250$ μm and $L = 200$ μm. The dashed blue (dotted pink) curve has the parameter, labelled at the top left side of each figure, doubled (halved). The variation of the parameters is the same as the stress profiles in Fig. (4.5)

The second and most important remark is that $\omega(q)$ exhibits a second peak at a finite wavenumber. The amplitude of the q-sinusoidal perturbations with a wavenumber similar to the second peak usually grow faster than the mode $q = 0$. This instability results in the formation of finger-like protrusions at the edge of the monolayer with a characteristic wavelength controlled by the dominant mode that maximizes ω. As it can be seen, in Fig. (4.8), the order of magnitude of such dominant wavelength is $\sim 200 - 300$ μm, in agreement with experimental evidences [126].

4.4 Mechanical instability and nonlinear waves from active forces

In this section we will provide and discuss an explanation of the origin of mechanical waves observed in epithelial cell monolayers, on the basis of a purely mechanical model in the presence of active forces. First, we will motivate the topic by presenting some examples reported in the literature of such phenomena. Then we will present an coarse-grained description of a cell sheet based on active polar gels theory, which exhibits non-stationary pattern formation. The analysis of the physical model will be divided in three main parts: first we will discuss the linear stability analysis of a steady homogenous polarized state into traveling-wave solutions. Second we will compute numerically the full nonlinear dynamics of the model and construct a phase-diagram of different dynamical behavior, obtaining the steady state solutions as a result of the evolution from random perturbations of the unstable state. Finally we will derive the parameters of the Complex Ginzburg-Landau corresponding to this Hopf bifurcation in terms of the physical parameters in order to classify the different dynamical regimes within a weakly nonlinear analysis framework.

4.4.1 Experimental observations

In recent years, a variety of experimental observations have been reporting examples of oscillatory behavior of the mechanical observables in epithelial cell monolayers. We will briefly review some of them here, in particular emphasizing the aspects that are more relevant to our analysis. For more details the reader is referred to the corresponding literature.

- In Ref. [51], the system consists of an initially confined one-cell thick monolayer placed in a rectangular space in a PDMS membrane, whose dimensions are 300×2500 microns, everything rested on top of a polyacrylamide gel

with a well-known elastic rheology. After 12 hours the PDMS membrane is carefully removed, which triggers cellular collective migration towards the newly available free space.

The polyacrylamide gel is mixed with small fluorescent beads whose displacement are tracked along the expansion of the monolayer. The traction forces at each time point are computed via Fourier Transform Traction Force microscopy with a finite gel thickness. On the other hand, the monolayer stresses are computed via Monolayer Stress Microscopy.

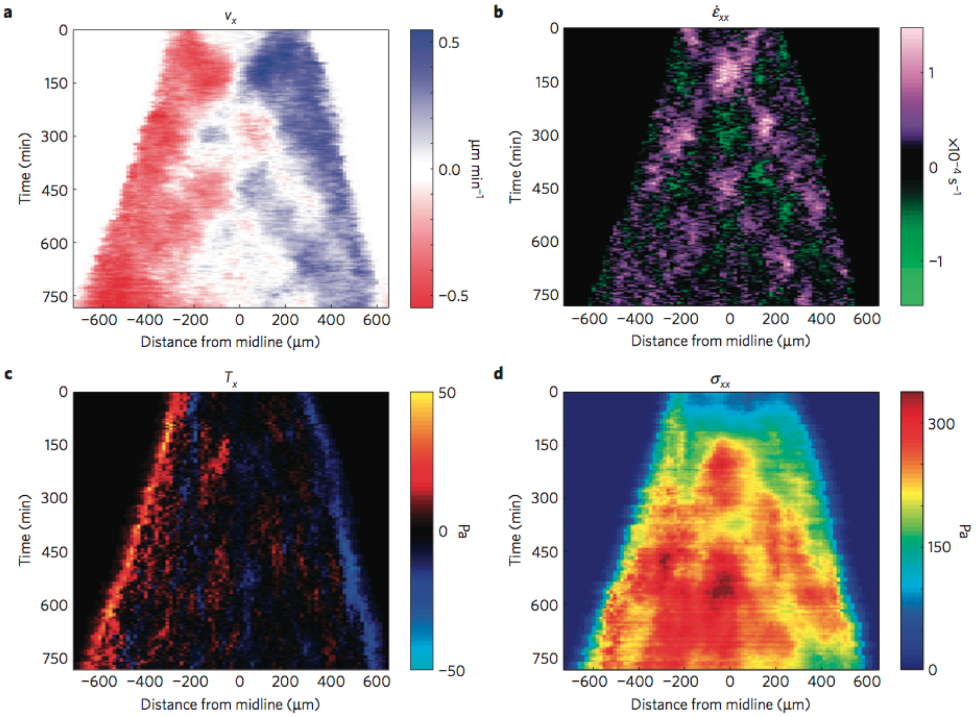

Figure 4.9: Kymographs of cell's velocity, strain rate, traction forces and intracellular stress. Figure modified from Ref. [51]

Then, cell force transmission and cell migration is initiated at the leading edges and propagate towards the central region of the monolayer. Taking advantage of the symmetries induced by the geometry of the system, the physical observables where averaged over the transversal direction. In Fig. (4.9), the temporal evolution of such averaged quantities is shown represented as a kymograph. The velocity field and consequently the strain-rate tensor are measured via PIV techniques. In the strain-rate kymograph, a couple of fronts can be seen at the midline at time ~ 150 coming from the leading edges and moving at approximately twice the expansion speed of the monolayer. A secondary and third peaks of strain rate at the midline can be observed at the time points ~ 450 min and ~ 750 min. Therefore, the strain rate at the midline oscillates with an amplitude that decreases with

time. The characteristic period and wavelength are around 300 min and 300 μm respectively. Interestingly, the intracellular stress oscillations at the same region are in phase quadrature with respect to the strain-rate oscillations, indicating that the dominant intracellular stresses are not viscous. Finally it is worth remarking that the mechanical waves are not observed in blebbistatin treated MDCK cell monolayers.

- In Ref. [109], the system is composed by fibronectin-coated micro-pillar arrays forming a striped pattern, in which one end is in contact with a reservoir, the lateral edges of the strip are non-adhesive and the width of the stripes is controlled. Then MDCK are placed at the reservoir and after reaching confluence are allowed to migrate towards these fibronectin stripes. The system is imaged during 16 hours at intervals of time of 15 min. The cell traction forces are measured through the pillar deflection caused.

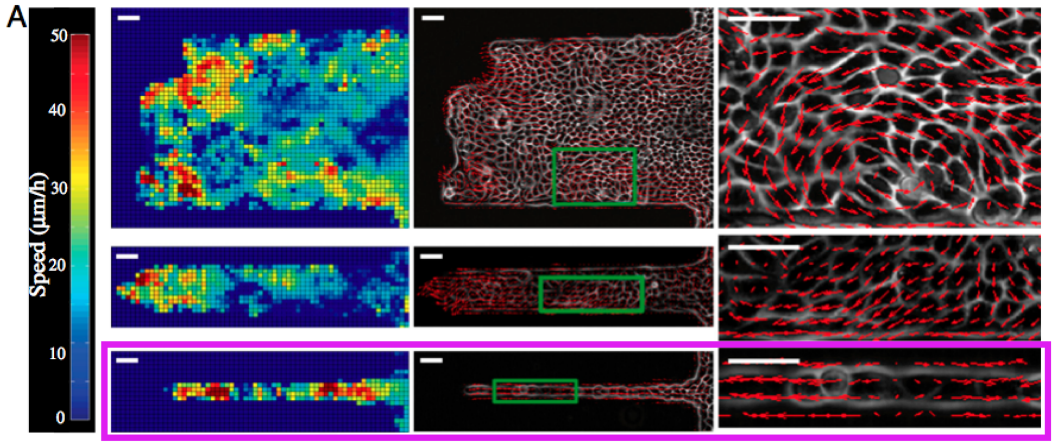

Figure 4.10: PIV analysis of migrating epithelial sheets on wide, intermediate, and narrow fibronectin stripes. Scale bars are 50 μm. Figure modified from Ref. [109]

In Fig. (4.10), the cell migration velocities for channels of widths 400, 100 and 20 μm are shown. In the present Section we will focus on explaining briefly the observations reported in the narrowest channel (pink rectangle), whereas in Section 4.5 the focus of attention will be switched into the results reported for the intermediate and the wider channels.

In the 20 μm stripe, the PIV analysis revealed that large values of the velocity span throughout the entire constrained cell monolayer and are not only restricted to the region close to the leading edge. Interestingly, significant negative velocities have been measured, such that the system exhibits a pattern similar that of a caterpillar motion. This mode of migration is exclusive of the narrowest channel. The authors highlighted the relevance of cell-cell junctions as a crucial component to observe long-range interaction within

the monolayer as well as coordinated directional motion.

On the other hand, the traction forces profiles along the longitudinal direction of the narrowest channel, exhibit several peaks of forces further away from the leading edge. The values are compressed between $70-90\%$ the average traction force at the leading edge. These forces are predominantly directed along the longitudinal direction of the channel, even though, as for the velocity profiles, the authors observed regions in space of significant negative traction forces.

Interestingly, blebbistatin-treated MDCK cells showed directed migration regardless of the channel width with similar traveling speeds ~ 0.5 μm/min. In the narrowest channel, the caterpillar-like motion was disrupted, indicating that it is driven by the acto-myosin cell machinery.

- In Ref. [127], the system is composed of adherent circular domains, whose radius is varied between 50 to 200 μm. These domains are surrounded by non-adhesive free space in which cells cannot migrate. Then between $10-100$ MDCK cells are seeded within the adherent domain. After the cell sheet reaches confluence, by means of PIV techniques the authors measure the cell velocities during a typical period of time of 60 hours. At the first 30 hours the cell density increases from the value at confluence until it reaches a steady value that persists in the second period of $30-60$ hours, in which cell division compensates for the cells that are apically extruded from the monolayer.

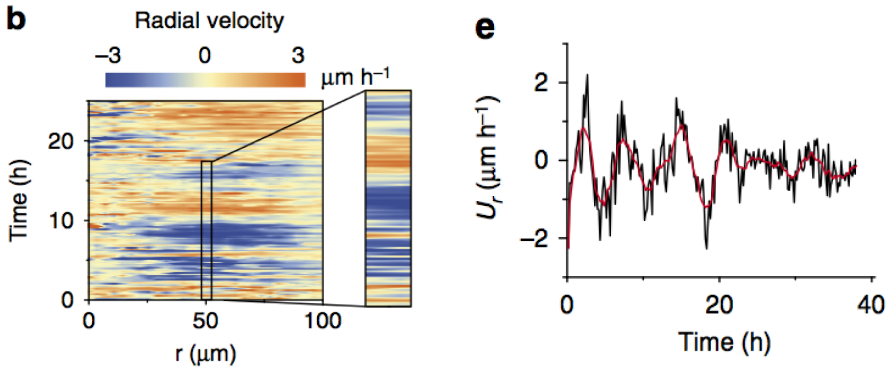

Figure 4.11: (a) Spatiotemporal evolution of the radial component of the averaged velocity. (b) Oscillations of mean radial velocity with time, size of the circular pattern ($\sim$ 100 mm). Figure modified from Ref. [127]

The quantity U_r displayed in Fig. (4.11) is the spatial average of the radial component of the cell velocity. The typical absolute value of the radial velocity is ~ 0.05 μm/min, which is one order of magnitude lower that in

[51, 109]. Then U_r oscillate with time between a zero mean value. The typical amplitude as well as the period of these oscillations are correlated with the size of the adherent domain. The period seems to be around ~ 300 min.

Finally, as well as in the previous cases, blebbistatin-treated MDCK cells do not display such an oscillatory behavior in the radial velocity, again pointing at the crucial role played by the contractile stresses of myosin.

4.4.2 Model for a monolayer with traction and contractile stresses

In this section we present a generalization of the previous continuum model for an epithelial cell monolayer, incorporating new effects such as the active contractile stresses. The objective is to provide a purely mechanical interpretation of a family of non-stationary patterns observed in cell sheets, in the framework of the active gels theory [2, 3]. In particular we will devote a special attention to the elastic-like waves observed at ultra-slow time scale in cell expanding monolayers, reported in Ref. [51].

Here we will base our study in the physical model derived in Section 4.2 for an expanding cell sheet. We also refer the reader to Section 4.2 for discussion and physical justification of the model. In its general derivation, no explicit form for the internal stresses has been assumed. In the present Section and until the end of the Chapter, we will assume that the internal stresses take the form

$$\sigma^S_{\alpha\beta} = 2\eta\tilde{v}_{\alpha\beta} - \zeta\Delta\mu(p_\alpha p_\beta - \frac{p^2}{2}\delta_{\alpha\beta}) - \frac{\nu_1}{2}\left(p_\alpha h_\beta + p_\beta h_\alpha - p_\gamma h_\gamma \delta_{\alpha\beta}\right) \quad (4.14)$$

including the terms that are consistent with the fundamental symmetries of an active polar fluid. The Greek letters run over the cartesian coordinates in the substrate plane and we take the Einstein summation convention for repeated indices.

The left-hand side $\sigma^S_{\alpha\beta}$ stands for the symmetric part of the total stress tensor. Conversely, $\sigma^A_{\alpha\beta} = (p_\alpha h_\beta - p_\beta h_\alpha)/2$ designates the antisymmetric part. Therefore the total stress tensor in Eqs. (4.1-4.2), is split as $\sigma_{\alpha\beta} = \sigma^S_{\alpha\beta} + \sigma^A_{\alpha\beta}$. We also recall that the traction forces may be written as $\mathbf{T} = \xi\mathbf{v} - T_0\mathbf{p}$.

One of the important terms are the active stresses, which couples the chemical activity in the system with the internal stresses. They are controlled by a phenomenological parameter $\zeta\Delta\mu$, which can be positive or negative depending whether theses stresses are contractile or extensile, respectively. In the case of cell sheets it has been assumed by other authors [92, 128] that these stresses at the

tissue level originate at the contractility of the cell cytoskeleton, and consequently $\zeta\Delta\mu < 0$.

With respect to the cell polarization field ($\mathbf{p}$), we will choose a free energy associated to the passive nematic properties that differs from the one proposed in Eq. (4.3), so that now the homogenous polarized state is energetically favored. This free energy takes the form

$$\mathcal{F} = \int d\mathbf{r} \left(\rho(-\frac{p^2}{2} + \frac{p^4}{4}) + \frac{K}{2}(\partial_\alpha p_\beta)(\partial_\alpha p_\beta) \right), \tag{4.15}$$

where ρ is taken as a positive parameter. The definition of the nematic length is the same and is given by $L_c^2 = K/\rho$.

In the context of the experiments of a rectangular epithelial monolayers, there is no clear direct evidence that supports the hypothesis of a fully polarized tissue. In fact it may seems more natural to assume that the cells are randomly oriented at the midline, according to the reported measurements on the traction force kymograph from Ref. [51], which are roughly zero at the monolayer central region, as shown in Fig. (4.9). Nevertheless, in our model it is necessary to assume that a large region of the tissue is polarized in order to predict non-stationary patterns. This hypothesis has also biological grounds in similar contexts, for instance in wound healing experiments, where it has been reported that cells that are hundreds of microns away from the wound edge extend basal cryptic lamellipodia underneath the neighboring cells pointing towards the wound [129]. Alternatively, in confined MDCK cell monolayers, it was observed that as the tissue invades a narrow channel of 20 μm width, the mean traction forces at a given fixed point in space, showed spikes of force away from the leading edge mainly oriented along the longitudinal direction of the rectangular channel [109].

From a theoretical point of view, we may argue on the basis of the study of Ref. [17], where it was predicted that for sufficiently small confinement width, a homogenous polarized state of an active polar fluid remains stable, whereas for a channel width larger than a threshold value that depends on the active stress coefficient, the rest homogenous polarized state becomes unstable. One can expect that in the conditions of [109] such characteristic length is above 20 microns, and thus the spikes of traction forces mentioned above may be seen as an indication of the existence of a homogenous polarized state. Alternatively, in the condition of [51], the dimensions of the rectangular MDCK cell monolayer, are 300×2500 microns. In that case, one might expect that the threshold length is above monolayer width and thus the homogenous polarized state is unobservable. Finally, it is worth remarking that in both cases from Ref. [51, 109] blebbistatin-treated cell sheets migrate collectively in a directional and persistent manner.

Under the above assumptions, to complete the physical model we need to include, in addition to the force balance equation, the equation governing the temporal evolution of the orientational field,

$$\partial_\beta \sigma_{\alpha\beta} = T_\alpha, \tag{4.16}$$

$$\frac{Dp_\alpha}{Dt} = \frac{1}{\gamma_1} h_\alpha - \nu_1 \tilde{v}_{\alpha\beta} p_\beta, \tag{4.17}$$

where $Dp_\beta/Dt = \partial_t p_\beta + v_\alpha \partial_\alpha p_\beta + \omega_{\alpha\beta} p_\beta$ is the co-rotational convected derivative, being $\omega_{\alpha\beta}$ and $\tilde{v}_{\alpha\beta}$ the antisymmetric and symmetric traceless part of the strain-rate tensor, respectively. As before, $h_\alpha = -\frac{\delta \mathcal{F}}{\delta p_\alpha}$ is the so-called molecular field.

In the next table, we provide the estimated orders of magnitude of the parameters in the present physical model.

$\eta \sim 10^5 - 10^6$ Pa·min	$\zeta \Delta\mu \sim 1000$ Pa	$\rho \sim 10$ Pa	$\xi \sim 10$ Pa·min/μm^2
$\bar{\gamma}_1 \sim 10 - 100$ min	$T_0 \sim 10$ Pa/μm	$L_c \sim 10$ μm	$L_\eta \sim 100$ μm

Table 4.1: Table of the parameter's orders of magnitude. η, ξ, T_0, L_c and L_η are extracted from the analysis in Section 4.3.4, $\zeta\Delta\mu$ is extracted from [128], ρ is extracted from [92] and $\bar{\gamma}_1$ is estimated from [114].

4.4.3 Bifurcation to traveling waves

In this section we perform a linear stability analysis of the polarized homogeneous state. We will find that the system undergoes a Hopf bifurcation at a critical value of the active stress, thus providing a natural explanation for the presence of propagating waves. The role of both active contributions in the tissue exhibit a fundamentally different role, since in the absence of active traction forces the bifurcation is stationary. Finally, we will discuss the relative phase between the stress and strain-rate profiles, which need not satisfy the usual relationship for passive viscous media. These results will be connected to the recently observed mechanical waves in epithelial cells monolayers Ref. [51].

We assume a steady state which is homogeneously polarized, defined by $p_x = 1$, $v_x = T_0/\xi$ and $\sigma_{xx} = -\zeta\Delta\mu/2$. To perform the linear stability analysis we assume

small-amplitude perturbations of the steady state of the form

$$\begin{aligned} p_x &= 1 + \delta p_x e^{i\omega(q)t+iqx}, \\ v_x &= T_0/\xi + \delta v_x e^{i\omega(q)t+iqx}, \\ \sigma_{xx} &= -\zeta\Delta\mu/2 + \delta\sigma_{xx} e^{i\omega(q)t+iqx}. \end{aligned}$$

Introducing them onto Eqs. (4.16-4.17) and keeping only the terms to linear order in the perturbations of the physical observables, we get

$$iq\delta\sigma_{xx} = \xi\delta v_x - T_0\delta p_x, \tag{4.18}$$

$$\delta\sigma_{xx} = iq\eta\delta v_x - \zeta\Delta\mu\delta p_x - \frac{\nu_1\rho(2+L_c^2q^2)\delta p_x}{2}, \tag{4.19}$$

$$\omega\delta p_x + \frac{T_0 iq\delta p_x}{\xi} = -\frac{(2+L_c^2q^2)\delta p_x}{\bar{\gamma}_1} - \frac{\nu_1 iq\delta v_x}{2}. \tag{4.20}$$

Solving these equations for each sinusoidal mode q yields the linear dispersion relation $\omega(q)$, which may be a complex number. The stability of the steady solution is determined by the sign of the real part of ω. For those modes q that give $Re[\omega] > 0$ (< 0), the homogenous solution is unstable (stable). On the other hand, those modes with a non zero imaginary part of ω, will be oscillatory indicating the existence of propagating waves that will be damped or amplified according to the real part of ω. In our case, by solving the linear system of equations, one obtains that

$$Re[\omega(q)] = \frac{-(2+L_c^2q^2)}{\bar{\gamma}_1}\left(1+\frac{\bar{\gamma}_1\nu_1^2\rho q^2}{4\xi(1+L_\eta^2q^2)}\right) - \frac{\nu_1\zeta\Delta\mu q^2}{2\xi(1+L_\eta^2q^2)} \tag{4.21}$$

$$\frac{Im[\omega(q)]}{q} = -\frac{T_0}{\xi}\left(1+\frac{\nu_1/2}{1+L_\eta^2q^2}\right). \tag{4.22}$$

It is important to recall that the present model contains two different active contributions: the active stresses that originate in the intracellular forces due to the action of molecular motors in the contraction of the cell cytoskeleton, encoded in $\zeta\Delta\mu$, and the active traction forces exerted by the cell on the substrate, encoded in T_0. Remarkably, both active mechanisms affect differently the dynamics of small perturbations on the polarized state.

The first term of the real part of omega (4.21) corresponds to the characteristic relaxation rate of a q-sinusoidal perturbation due to the energetic cost to create inhomogeneities in space and vary the modulus of the orientational field of cells. At small wavelengths, it is dominant and scales asymptotically as $-q^2$. On the other hand, the second term of the real part of ω (4.21) is an active contribution that favors (disfavors) the growth of a random perturbation provided that the sign of $\zeta\Delta\mu\nu_1 < 0$ (> 0). This term arises from the coupling between the active

contractile stresses and the capability of cells to re-orient their polarity to the local stresses tensor. The phenomenological transport coefficient ν_1 is called the flow alignment coefficient and its value is usually not known for tissues. A rich variety of effects induced by this coupling has been reported previously in other type of systems, such as a spontaneous-flow transition in active polar films [17], a shear-flow induced transition between isotropic to nematic phase [130] and an anomalous nonlinear rheology in active polar particles suspensions [8]. As it will be clear below, this coupling in our system permits sustaining elastic-like traveling waves, even though the tissue has been modeled as a purely viscous fluid.

In the case of epithelial cell monolayers, it is expected that the nature of the active stresses is contractile (i. e. $\zeta\Delta\mu < 0$), therefore in order to predict linear mechanical waves in the context of the present model it is necessary to require that $\nu_1 > 0$. The sign of the flow alignment parameter ν_1 is not restricted by thermodynamical laws or symmetries, and can in principle be both positive or negative. In liquid crystal theories, it is known that the value is controlled by the shape of the unit particles, following the criteria that $\nu_1 < 1$ corresponds to elongated rod-like particles, whereas $\nu_1 > 1$ corresponds to disk-like particles. The magnitude of $|\nu_1|$ measured in liquid crystals suspensions is of the order of 1. Nevertheless, it is important to remark that cells might re-orient their polarity to the local stresses by means of alternative mechanisms, such as remodelling the cytoskeleton, an effect with no counterpart in passive nematic media. The only experimental measurement we are aware of ν_1 in a biological system is in the imaginal disk of the Drosophila melanogaster wing, which seems to robustly fit the data within the range of $-10 < \nu_1 < -1$ [101].

The fact that there are active contractile stresses is thus crucial to generate an instability. One can compute the instability threshold ($\nu_1^c\zeta\Delta\mu^c$) and the dynamically dominant wavenumber (q^c) by solving the Eqs. $Re[\omega] = \partial_q Re[\omega] = 0$, which has a single solution.

For simplicity of the notation we introduce two new dimensionless parameters: $H \equiv \bar{\gamma}_1\nu_1^2\rho/\eta$, the ratio between the bulk and the rotational viscosities, and $G \equiv L_c/L_\eta$, the ratio between two characteristic length scales of the system. Near the instability point and with $\nu_1\zeta\Delta\mu < \nu_1^c\zeta\Delta\mu^c$, any weak amount of random noise on the polarized homogeneous state will excite the growth of the most unstable mode, and the system will approach a traveling-wave form with a characteristic wavelength and traveling speed given by $\lambda^c = 2\pi/q^c$ and $V^c = -Im[\omega(q^c)]/q^c$,

respectively

$$\frac{\nu_1^c \zeta \Delta\mu^c}{\eta/\bar{\gamma}_1} = -\left(\sqrt{2}G + \sqrt{H+4}\right)^2, \tag{4.23}$$

$$L_\eta q^c = \frac{2^{3/2}}{\sqrt{G}\sqrt[4]{H+4}}, \tag{4.24}$$

$$\frac{V^c}{T_0/\xi} - 1 = \nu_1 \left(\frac{G\sqrt{H+4}}{2G\sqrt{H+4}+4\sqrt{2}}\right). \tag{4.25}$$

At linear level the amplitude of this wave will grow exponentially and nonlinearities will eventually saturate the growth to a finite amplitude. The functional form of the above expressions is rather involved. In Fig. (4.12) we plot them in terms of the two dimensionless parameters.

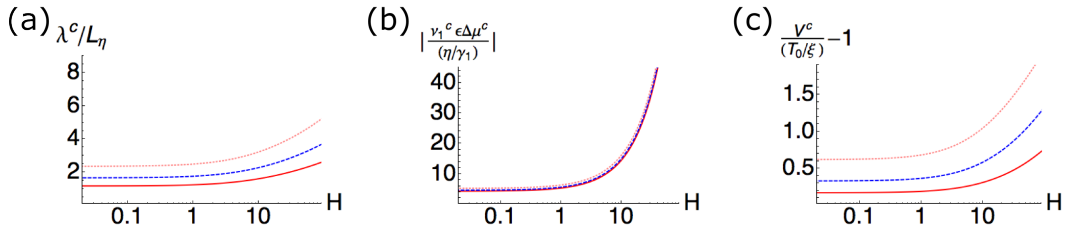

Figure 4.12: Characteristic quantities of the linear mechanical waves. (a) Critical wavelength, (b) Normalized instability threshold and (c) Travelling speed as a function of H. The solid red, dashed blue and dotted pink curves correspond to the values of $G = 0.05$, 0.1 and 0.2. In (c) $|\nu_1| = 10$.

In the case of expanding MDCK cell sheets, a long-time periodicity of ~ 400 min was reported for such waves. Their traveling speed was of the order of 1 μm/min, and the wavelength was 400 μm, [51]. If we assume that in this system the active stress coefficient is of the order of ~ 1000 Pa, based on the monotonic behavior displayed by the instability threshold (Fig. (4.12,b)), we may estimate that the dimensionless parameter $H < 10$. Alternatively, in order to adjust the range of values of the flow-alignment coefficient, we compare Eq. (4.25) with the measured traveling velocity, which leads to the result that $|\nu_1| \sim 10$, Fig. (4.12,c). Finally, the predicted values of the wavelength are within the right order of magnitude ~ 100 μm.

As an estimated value for G we obtain $G \sim 0.1$ because L_c and L_η are of the order of 10 μm and 100 μm, respectively. Conversely with respect to the other dimensionless parameter H, one can compute it from the Franck constant value estimated in Ref. [92] from wound healing assays, $K \sim 10^3$ Pa$\cdot\mu$m^2, which leads to a value H within the range $\sim 10^{-2} - 1$, if the flow-alignment coefficient is accepted to vary within the values $|\nu_1| = 1 - 10$ and $\eta/\bar{\gamma}_1 = 1000$ Pa. These values of H

are consistent with the upper bound from above.

Finally, we conclude this section with the expressions of (4.23-4.25) approximated in the limit $G, H \ll 1$, which then read

$$\begin{aligned} \nu_1^c \zeta \Delta\mu^c &\approx -\frac{4\eta}{\bar{\gamma}_1}, \\ q^c &\approx \frac{\sqrt{2}}{\sqrt{L_c L_\eta}}, \\ \frac{V^c}{T_0/\xi} - 1 &\approx \nu_1 \frac{\sqrt{2} L_c}{4 L_\eta}. \end{aligned}$$

4.4.4 Mechanism for elastic-like waves in a viscous medium

So far we have discussed the existence of traveling waves in a simple extended active medium that models an expanding monolayer such as those composed by MDCK cells as an active viscous fluid, where elastic effects are neglected at the observation time scale. However, one of the main conclusions of Ref. [51] is that, on the basis of the relative phase between stress and strain rate, the mechanical waves observed are actually elastic despite having a period of 400 min. Consequently, at this ultra-slow time scale of cellular migration, the dominant stresses of the tissue seemed not to be viscous. To reach this conclusion on the stress-strain rate waves, it is necessary to use the Stress Monolayer Microscopy technique in order to measure the intracellular forces within the tissue, and compare them with the strain rate tensor measurements via PIV techniques. In this section, we will address this point theoretically in the framework of the linear stability analysis of the homogeneous polarized state.

First of all, to gain insight on the origin of the stress-strain rate relative phase in our system, let us consider the linearized equations Eqs. (4.18-4.20) for a small perturbation on the homogenous polarized state and, for the sake of discussion, let us neglect the intracellular stresses in the force balance equation. The cells would then behave as self-propelled particles (i.e. $\delta v_x = T_0 \delta p_x / \xi$). If, in addition, we neglect the contribution to the stresses due to distortion on the orientation field of cells (i. e. $\delta\sigma_{xx} = \eta i q \delta v_x - \zeta \Delta\mu \delta p_x$), then the two equations can be combined to extract a simple relation between the stress and the strain rate perturbations, which reads

$$\delta\sigma_{xx} = \left(\eta + i \frac{\zeta \Delta\mu \xi}{q T_0} \right) i q \delta v_x. \tag{4.26}$$

Accordingly, in the limit in which viscous stresses are negligible against active stresses the latter relation states that the oscillations in the stress are in phase

quadrature with respect to the strain rate ones. Therefore, activity somehow generates a non-trivial rheology in the system. Even thought elastic effects have not been included in the passive rheology of the medium, active stresses may introduce a finite relative phase between stress and strain rate, which is characteristic of elasticity. The total stress may even be in quadrature with the strain rate, which would be the case of a purely elastic wave. In this sense we conclude that an active viscous medium can sustain elastic-like waves.

In the general case, the relative phase between stress and strain rate oscillations $\phi \equiv arg(\delta\sigma_{xx}/iq\delta v_x)$ is more complicate. Combining Eqs. (4.18-4.19) one can derive an expression for the general case

$$\delta\sigma_{xx} = \eta\left(-\frac{\zeta\Delta\mu + \nu_1\rho\left(2 + L_c^2q^2\right)/2 - iL_\eta^2qT_0}{L_\eta^2q^2\left(\zeta\Delta\mu + \nu_1\rho\left(2 + L_c^2q^2\right)/2 + iT_0/q\right)}\right) iq\delta v_x \tag{4.27}$$

In Fig. (4.13), we show the behavior of ϕ at the critical point. To obtain these curves we have plugged Eqs. (4.23-4.25) into the argument of the latter expression. In addition to the dimensionless parameters defined above, we have introduced a new one that we define as $F = T_0\bar{\gamma}_1/\xi L_\eta$, which is estimated to be within the range $1 - 10$.

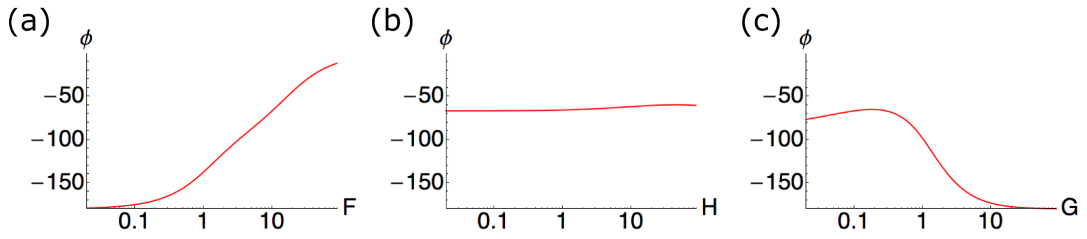

Figure 4.13: Relative phase ϕ between the linear stress and strain rate waves. In each figure the set of dimensionless parameters is chosen $G = 0.1$, $H = 0.01$ and $F = 10$, except one that is varied, in (a) F, in (b) H and in (c) G.

4.4.5 Numerical integration of the full nonlinear dynamics

In this section we integrate numerically the full dynamics of our model for initial conditions of the form of random perturbations around the homogenous polarized state. In particular we will focus the study on a range of parameters close to the instability threshold. Then, we will examine the behavior of the system in the fully nonlinear regime and classify the nontrivial solutions reached asymptotically in time.

The linear stability analysis has revealed that the homogeneous polarized state undergoes a oscillatory periodic instability at a critical value of the active stress.

Consequently, if we add a random small perturbation to the homogeneous state for values of active stress above threshold, they will grow in the form of a traveling sinusoidal perturbation with a dominant wavenumber given by (4.24). This growth will in principle be saturated by nonlinearities and it remains a non trivial open question to elucidate the properties and the different possibilities of the asymptotic behavior in the nonlinear regime. For values arbitrarily above the instability threshold, this point must be explored numerically. However, sufficiently close to the onset of instability, a weakly nonlinear analytical approach is possible and we developed it in the next section.

We construct a simple semi-implicit method, which is described in Appendix 7.8, to integrate the dynamics of the system described by Eqs. (4.16-4.17) reduced to $1d$ from Section 4.4.2. We choose periodic boundary conditions and impose a small random perturbation on the homogeneous polarized state as an initial condition.

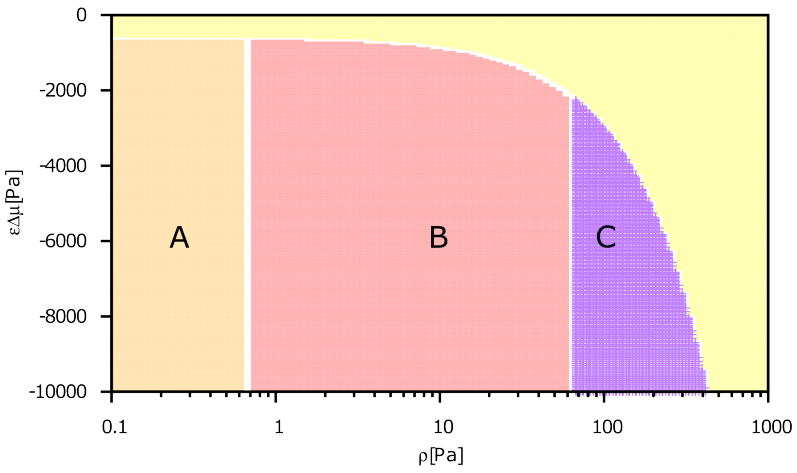

Figure 4.14: Phase-diagram represented in the plane $\zeta\Delta\mu$-ρ. There four different domains: the yellow one corresponds to the stable region of the homogeneous polarised state. The steady nontrivial solutions in the orange domain corresponds to soliton-like migrating patterns, whereas in the red and purple regions the patterns correspond to nonlinear propagating waves. The border that demarcates the yellow region is given by the instability threshold (4.23). From the weakly nonlinear analysis, one can determine the values of the rest of the borders at the instability's threshold. We have extended these values vertically into the phase diagram. The parameters are: $\eta = 10^6$ Pa·s, $\xi = 100$ Pa·s/μm^2 , $T_0 = 10$ Pa/μ, $L_c = 50$ μm, $\bar{\gamma}_1 = 600$ s and $\nu_1 = 20$.

In Fig. (4.14), we display the phase-diagram obtained for the system, which is composed by four different domains. The parameters that are varied are the active stress coefficient and ρ. We have chosen ρ instead of T_0, because to our

knowledge there is little reported information on epithelial cell monolayers that allow to estimate it. In Ref. [92], ρ has been estimated to be for MDCK cells $\rho \sim 10$ Pa. In Fig. (4.14), the yellow domain depicts the region where the homogeneous polarized state is linearly stable. For the other domains, which are labelled as A, B and C, the representative asymptotic steady solution are depicted in Fig. (4.15).

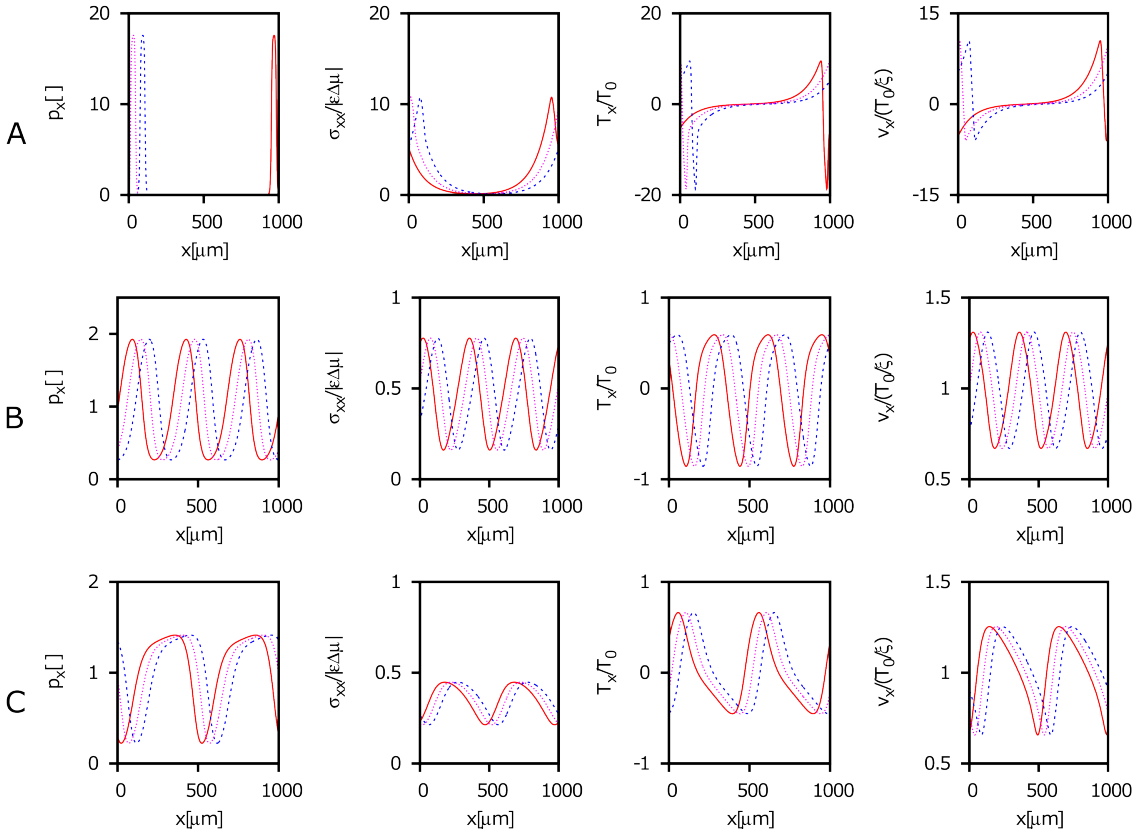

Figure 4.15: Representation of the physical observables of the asymptotic nonlinear profiles in each domain of the phase diagram. The physical observables has been normalised conveniently. It has been taken the same set of parameters as in Fig. (4.14). In the first row (A) $\rho = 0.1$ and $\zeta\Delta\mu = -1000$ in the second row (B) 10 and -1200 and in the third row (C) 100 and -3400, both coefficients are in units of Pa. The dashed blue profiles is at the time point 198 min, the dotted pink profile at 195 min and the solid red profile at 192 min.

- In domain A, we observe that the polarity field, which is initially almost homogeneous, reaches an array of equally spaced peaks, whose periodicity in space is related to the critical wavelength (4.24). Each peak has a traveling velocity that is slightly different among them. Eventually, all the polarity peaks merge between themselves and only one persists, as shown in Fig. (4.15). After this stage is reached, at the broad region with zero polarity, new peaks might be created, probably due to numerical noise.

The transition from the stability region of the homogeneous polarized solution, is discontinuous.

One of the landmarks of this type of solutions is the high values of the polarity field, with respect to the reference value. The maximal polarity seems to be controlled by $\sqrt{\zeta\Delta\mu/\rho\nu_1}$, which arises from the balance between the stress terms $\propto \zeta\Delta\mu p_x^2$ and $\propto \nu_1 p_x h_x$. In a biological context, this solution might be connected to a solitary wave of polarization propagating in a background of isotropically oriented cells. The measurements on the local anisotropy of cells might provide an estimation of ρ.

- In domain B, the physical observables display a clear wave-like behavior. The traveling wave velocity is controlled by T_0/ξ as it was predicted from the linear stability analysis. Finally, the transition from the stability region of the homogeneous polarized solution, is continuous.

- In domain C, the physical profiles as in domain B, exhibit a nonlinear periodic pattern, which propagates at a velocity controlled by T_0/ξ. However, in this case the transition from the stable region of the homogeneous polarized solution, is discontinuous.

Finally, we put emphasize on the stress-strain rate curves for each nontrivial solution. Obviously they do not satisfy the usual linear relation of a viscous fluid, Fig. (4.16), as a consequence of both the nonlinearity of the dynamics and the presence of active forces in the system. Therefore, the previous result from Section 4.4.3, regarding the dependency of the relative phase between the stress and the strain rate perturbations on the model parameters, is also validated in the nonlinear regime.

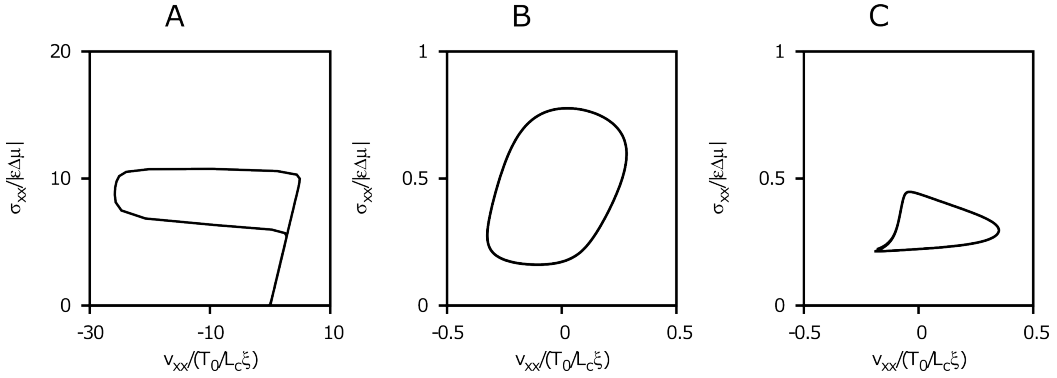

Figure 4.16: Stress-strain rate curves for the asymptotic nonlinear solutions in the phase diagram. The variables σ_{xx} and v_{xx} denotes the stress and strain rate tensor components for a $1d$ system. The conditions of the temporal evolution in each case A, B and C is the same as the one shown in Fig. (4.15)

4.4.6 Complex Ginzburg-Landau equation near onset

A numerical study of the complete nonlinear phase diagram in parameter space is beyond the scope of this work, and probably not very useful for comparison with experiments, due to the simplifications of the model and the relatively large experimental uncertainties. From a theoretical point of view, however, it is interesting to perform a weakly nonlinear analysis close to the instability threshold. In this regime an amplitude equation can be derived for the envelope of the basic wave pattern, which is universal in the sense that it is shared by all systems with the same symmetries and undergoing the same type of oscillatory (Hopf) bifurcation [131, 132]. This approach generalizes the center-manifold reduction procedure to spatially extended systems, by exploiting the separation of time scales between the narrow, nearly marginal band of unstable modes and the rest of stable modes. In this case of a Hopf bifurcation, the corresponding amplitude equation is the so-called Complex Ginzburg-Landau (CGL) equation [131]. The interest of this approach is that, once the parameters of the CGL equation are determined in terms of the physical parameters of the model, all the possible dynamical regimes are automatically classified, taking into account that the phase diagram of the CGL is known in full detail [131]. This contains a rich variety of nonlinear dynamics, including for instance the presence of intermittency and spatiotemporal chaos. In other words, sufficiently close to the instability, the phase diagram of our problem can be exactly mapped into the phase diagram of the CGL. The interest of this map relies not only in knowing the possible dynamical phenomena to be found in the original system depending on physical parameters, but the fact that in the region close to onset of the instability these dynamics are not sensitive to details of the original physical model but only to the actual values of the parameters of the CGL equation. Therefore, from a theoretical point of view it make perfect sense to derive the map between the physical parameters and those of the CGL equation. It may obviously be the case that some of the regimes of the CGL are not accessible for realistic values of the physical system, but since our instability is also quite generic, it is not ruled out that other types of tissues or active materials in general could incorporate different parameter regimes of the CGL equation.

The general form of the CGL equation can be written as

$$\partial_t A = A - c_1(1+ic)|A|^2 A + (1+ib)\partial_{xx}^2 A, \tag{4.28}$$

where the real coefficients c_1, c and b, are functions of the physical properties of each extended system and A is a complex amplitude that describes the slow and smooth modulations of the basic mode. Since one may still absorb the coefficient $c_1 > 0$ in a rescaling of A, the CGL depends essentially on two parameters, c

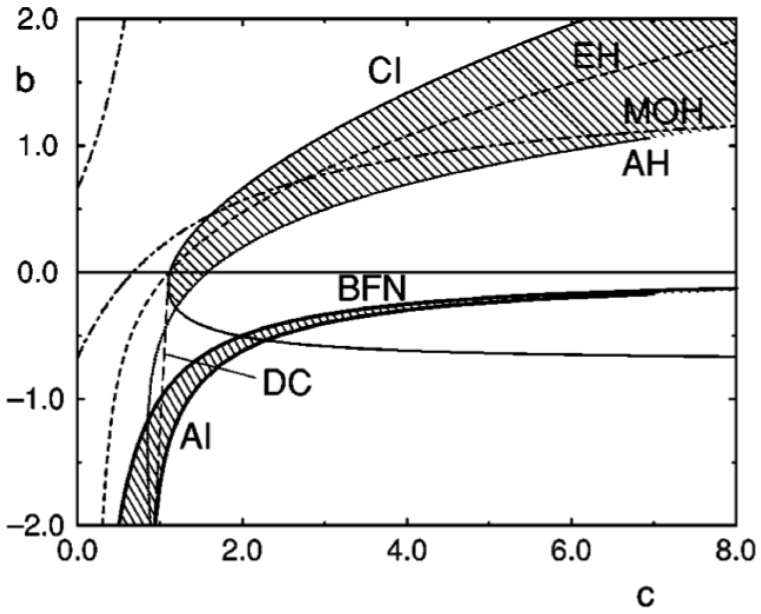

Figure 4.17: Phase diagram of the $1d$ CGL equation: BFN, Benjamin-Feir-Newell instability line up to which one has convectively stable plane-wave solutions; AI, absolute instability line up to which one has convectively unstable plane-wave solutions; DC, boundary of existence of DC towards small $|c|$. The other lines pertain to standing Nozaki-Bekki hole solutions: CI, core instability line; EH, convective (Eckhaus) instability of the emitted plane waves; AH, absolute instability of the emitted plane waves; MOH, boundary between monotonic and oscillatory interaction. Modified from Ref. [131].

and b. In Fig. (4.17), we show the phase-diagram of the CGL equation, which is invariant to the change $(c, b) \to (-c, -b)$. In the following analysis, we do not restrict the values that c_1 can take. However, in case that c_1 is negative, the bifurcation is subcritical and the cubic nonlinearity does not saturate the growth of A. A quintic CGL should be considered in that case.

A detailed explanation of the procedure to compute the CGL equation for a set of equations like ours is very technical and is sketched in Appendix 7.9. In brief, this procedure relies on a formal expansion on a small parameter defined by the distance of the control parameter to the critical value or instability threshold. In our case, the system undergoes an oscillatory periodic instability when crossing the threshold value $\nu_1^c \zeta \Delta\mu^c$, given by Eq. (4.23). Close to this threshold one exploits the separation of the time and length scales between the dominant unstable mode and the rest of modes. The distance from threshold allows one to organize systematically the different orders once the proper scaling of length and time is introduced from the knowledge of the linear dispersion relation. The solution of the problem can then be expressed as an infinite set of linear inhomogeneous PDEs.

The corresponding solvability conditions for these inhomogeneous equations yield to lowest order the amplitude equation [133].

If $\omega(q_c)$ is defined as the growth rate associated to the q_c-sinusoidal perturbation, then it can be written as

$$Re[\omega(q_c)] = \frac{2\left(\nu_1^c \zeta \Delta\mu^c - \nu_1 \zeta \Delta\mu\right)}{\eta\left(4 + \frac{L_c}{L_\eta}\sqrt{8 + 2\frac{\bar{\gamma}_1 \nu_1^2 \rho}{\eta}}\right)} + \mathcal{O}((\nu_1^c \zeta \Delta\mu^c - \nu_1 \zeta \Delta\mu)^2).$$

Consequently, the growth rate associated to the critical mode is controlled by the active stress coefficient and can be arbitrarily small.

The derivation of the amplitude equation is a generalization of the adiabatic elimination of the fast modes formalized as the center-manifold reduction in Chapter 2. Note however that the number of slow modes is formally infinite (for a system of infinite size) as it involves a continuous (narrow) band of unstable modes, with their wavenumbers contained in an interval centered at q_c and with a width $\propto \sqrt{Re[\omega(q_c)]}$, which assumed to be small slightly above threshold. This localization in q-space implies long wavelength modulations of the dominant mode with slow dynamics. The complex amplitude A that describes the frequency and modulus modulations of the dominant mode are those described in the amplitude equation, in our case Eq. (4.28), whereas the details of the specific problem are encoded in the coefficients of that equation.

In our system, we computed analytically the coefficients c_1, c and b. Some details are given in Appendix 7.9. The last coefficient reads

$$b = \frac{F}{2}\frac{(4 - 3G\sqrt{8 + 2H})}{\sqrt{G}\sqrt[4]{8 + 2H}(8 + G\sqrt{8 + 2H})^2},$$

where $F = T_0\bar{\gamma}_1/(\xi L_\eta)$, $H = \bar{\gamma}_1\nu_1^2\rho/\eta$ and $G = L_c/L_\eta$.

It is important to highlight that this parameter is proportional to T_0. This is a consequences of the fact that in the absence of active traction forces the instability becomes stationary and (spatially) periodic, and so Eq. (4.28), reduces to the Real Ginzburg-Landau equation, with real coefficients in the equation for the complex amplitude. The explicit dependence of the coefficients c and c_1 on the physical parameters is extremely complicated. This has been determined with the help of the capabilities of symbolic calculus of the software Mathematica, and they are provided in Appendix 7.9.

In Fig. (4.18), we show how they depend on the parameter ρ for the same set of parameters as in the phase diagram constructed before (4.14). When c_1 is positive (negative), the bifurcation is continuous/supercritical (discontinuous/subcritical).

There, the values at which this coefficient vanishes have been used to define the boundaries between the domains A, B and C in Fig. (4.14).

On the other hand, if we restrict ourselves to the region in which c_1 is negative, we can observe that except for values of c_1 too small, c and b move within a region of the CGL phase diagram in which a family of plane-wave solutions from Eq. (4.28) are stable. Regarding the nonlinear numerical integration of the $1d$ physical model, what we have found is that the system approaches asymptotically nonlinear oscillatory profiles.

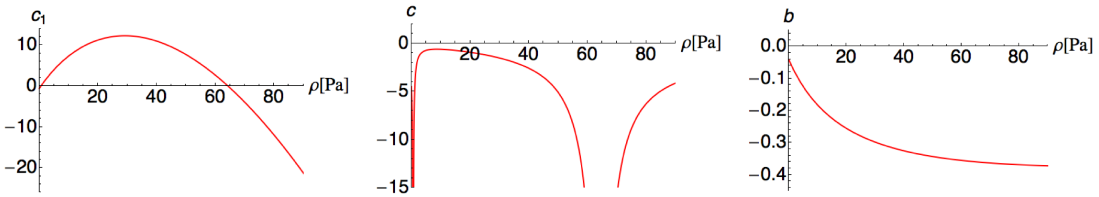

Figure 4.18: Characteristic coefficients of the $1d$ Complex Ginzburg-Landau equation as a function of ρ, in which the rest of the parameters are the same as the ones in Fig. (4.14).

Furthermore, one may also explore different regions of parameter space in search of other possible dynamic scenarios in our system. Specifically, it is interesting to elucidate whether or not the system might exhibit spatio-temporal chaotic behavior, a possibility that is contained in the CGL equation. Indeed there are many sources of noise in the experiments on this problem. A conceptually important one is the fact that cells are discrete units with finite size and significant variability of their individual properties. However, it would be interesting to know whether the continuum dynamics is by itself intrinsically chaotic and could explain in part the complex dynamics observed. In particular, in the range depicted in Fig. (4.19), our model equations are expected to exhibit the so-called defect chaos. From the partial knowledge of the physical parameters, it does not seem plausible that this regimes is realistic in our specific physical system. However one can not rule out that other similar systems may exhibit the full richness of the CGL equation.

4.5 Instabilities in $2d$ confined monolayers

In this section we address the $2d$ extension of our previous coarse-grained model of an expanding epithelial cell monolayer. The analysis will consist on the characterization of the temporal evolution of small perturbations of the uniform base

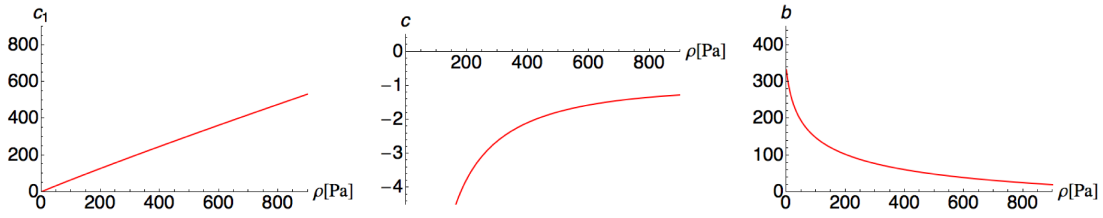

Figure 4.19: Characteristic coefficients of the 1d Complex Ginzburg-Landau equation as a function of ρ, in which the rest of the parameters are the same as the ones in Fig. (4.14), except for T_0 which is hundred times higher and L_c which is ten times lower.

state throughout the plane of the substrate, thus allowing longitudinal as well as transversal perturbations of the physical observables. Part of the results stem directly from those reported in Ref. [17] on the spontaneous-flow transition in thin layers of active polar fluids. We will put these results in the context of the recent work performed on confined epithelial monolayers in Ref. [109] and try to revisit those experiments from this new perspective.

4.5.1 Scenario for a transversal instability

As discussed in previous sections, the material properties of the cells that compose expanding monolayers allow to categorize them as soft active materials. From the general perspective of active polar gels theory, a cell sheet is qualitatively similar to cell lamellipodia equivalent of to bacterial suspensions, in the sense that, apart from the specific values of a set of phenomenological coefficients, which encode microscopic properties of each particular system, their constitutive laws are equivalent.

In Ref. [17], an instability of thin layers of such active materials was shown to lead to spontaneous flow via a Frederiks-like transition driven by their inherent activity. In briefly, the Frederiks instability in passive nematic liquid crystals, is the transition from an homogeneous polarized state into a distorted state of the director field, upon the application of a sufficiently large magnetic or electric field with which the particles interact. Qualitatively, in the absence of an external field the homogenous polarized state is a minimum of the free energy, which can be induced via boundary conditions. However, the interaction between the anisotropic particles and the external field contributes to create a new minimum in the energy in which the nematic director is modulated between the confinement walls. This becomes the new configuration as long as the intensity of the external field surpasses a specific threshold. Similarly, in the case of confined active polar materials

there is an analogue of the Frederiks instability, where the role of the external field is played by the active stress [17]. The dimensionless control parameter involves the width of layer, so for a fixed activity, when the confinement is wide enough, the homogeneous polarized state gets also distorted. The active stresses are then balanced by viscous stresses as a spontaneous flow is generated. Other authors has reconstructed parts of the global phase-diagram of these type of material as in [19, 134], showing that there is a broad diversity of $2d$ patterns, ranging from spontaneous oscillations of banded flows or rotating lattice phases.

Our cell sheet model shares some similarities with the active material described above. In that sense, one could expect that there is also a sort of Frederiks-like instability. Interestingly, the experiments performed in Ref. [109] are consistent with this picture. In their case, the cell sheet is able to migrate through an adhesive strip with a controlled width (for more details see Section 4.4). In Fig. (4.10), the velocity maps for three different widths are shown. The authors reported two modes of migration: a contraction-elongation type of motion at the narrower channel and the formation of large-scale transient rotating vortices at the wider channel. Interestingly, blebbistatin-treated MDCK cells do not display such a rich phenomenology, and yet they retain the capability to migrate directionally along the adhesive strip. Most of the discussion is centered on both extreme values for the width of the strips, but the velocity map at the intermediate channel (~ 100 μm width) in Fig. (4.10), appears as if the direction of velocity field oscillated periodically in space, specially near the edge. To the best of our knowledge, such periodic patterns have not been mentioned or commented before. Nevertheless, if we assume that they exist, one can propose the following scenario. At the narrow strip, the lateral boundary conditions favor the cells to be oriented along the longitudinal direction fixed by the geometry of the channel. However, the homogeneous polarized state is now unstable through the mechanism discussed in the previous sections, and thus unobservable at sufficiently long times. In this case the system acquires a caterpillar-like migrating mode. As the width of the strip increases, so does the largest transversal wavelength that fits in the channel and eventually a Frederics-like transition may take place. At the intermediate strip width, the first unstable transversal periodic perturbation appears in the system, and so the system undergoes a transition from the caterpillar-like motion into another state, in which the flow shows a transversal structure in the form of vortices. At wider strips, the nonlinear couplings between unstable transversal modes start to affect notably the behavior of the system, and non-stationary large vortical structures on the scale of hundreds of microns are generated. The vortex-like migrating mode seems to be maintained as the width of the channel increases further.

This scenario is related to the one discussed in Ref. [17], but it differs in that

the reference state that undergoes a Fredeircs-like instability in the narrow strip is not quiescent but motile. Nevertheless, we will show below that the physical model for the cell sheet described in Section 4.4.2 contains a Frederiks-like transition and thus, we conjecture that the expanding cell monolayer provides an experimental example of the transition predicted in Ref. [17].

4.5.2 Linear stability analysis in a $2d$ configuration

Here we perform a linear perturbation analysis of the homogeneous polarized state in a $2d$ confined geometry, allowing for both longitudinal and transversal perturbations of the physical observables. This analysis is a generalization of the one carried out in Section 4.4.3, that revealed an oscillatory periodic instability for longitudinal perturbations. However, as we will show below, for an infinitely extended $2d$ system the most unstable mode will not be the longitudinal ($1d$) case.

We assume that the systems is extended on an infinite $2d$ plane. We take the cartesian coordinates x and y such that the x direction is parallel to the homogeneous polarized state. In this case, the steady homogeneous state is defined by $p_x = 1$, $v_x = T_0/\xi$ and $\sigma_{xx} = -\zeta\Delta\mu/2$.

We will investigate the dynamics of small perturbations with wavenumber $\mathbf{q} = (q_x, q_y)$ around the steady state, which read

$$\begin{aligned} p_x &= 1 + \delta p_x e^{i\omega(q)t + iq_x x + iq_y y}, \\ p_y &= \delta p_y e^{i\omega(q)t + iq_x x + iq_y y}, \\ v_x &= T_0/\xi + \delta v_x e^{i\omega(q)t + iq_x x + iq_y y}, \\ v_y &= \delta v_y e^{i\omega(q)t + iq_x x + iq_y y}, \end{aligned}$$

where δp_x, δp_y, δv_x and δv_y will be referred as perturbation amplitudes and are thought to be of order $\epsilon \ll 1$.

We introduce them onto Eqs. (4.16-4.17) and expand these at the linear order in the perturbation amplitudes of the previous physical observables. The symmetric part of the total stress profile is given by Eq. (4.14). Then one obtains a set of linear equations, which in the case of $q_y = 0$ reads

$$\begin{pmatrix} q_x(q_x + iT_0) + \omega + 2 & \frac{i\nu_1 q_x}{2} & 0 & 0 \\ \frac{iq_x\left(2\zeta\Delta\mu + \nu_1\left(q_x^2+2\right)\rho\right) - 2T_0}{2} & \eta q_x^2 + 1 & 0 & 0 \\ 0 & 0 & q_x(q_x + iT_0) + \omega & \frac{i(\nu_1+1)q_x}{2} \\ 0 & 0 & \frac{iq_x\left(2\zeta\Delta\mu + (\nu_1-1)\rho q_x^2\right) - 2T_0}{2} & \eta q_x^2 + 1 \end{pmatrix} \begin{pmatrix} \delta p_x \\ \delta v_x \\ \delta p_y \\ \delta v_y \end{pmatrix} = 0$$

For simplicity we use units in which $\xi = L_c = \bar{\gamma}_1 = 1$.

As we can see, in the case $q_y = 0$, the dynamics of the subsets $(\delta p_x, \delta v_x)$ and $(\delta p_y, \delta v_y)$ are decoupled. We refer to them as longitudinal and transversal modes, respectively. The former corresponds to the case studied for a $1d$ system in Section 4.4.3, whereas the latter corresponds to the transversal perturbations with respect to the direction set by the homogeneous polarized state. Then, the temporal evolution of any small random perturbation can be interpreted in terms of the temporal evolution of the previous two subsets of perturbations, which are controlled by a single function ω that may be a complex number. The convention is chosen such that if $Re[\omega] > 0$ (< 0), the corresponding mode is unstable (stable). On the other hand, if the imaginary part of ω is non zero, this indicates that the random perturbations over the polarized state are oscillatory and they may propagate in space as waves. The system presents two type of modes and we define respectively the growth rate associated to the longitudinal (transversal) modes as $\omega^l(\mathbf{q})$ $(\omega^t(\mathbf{q}))$. In the general case $(q_y \neq 0)$, the longitudinal and transversal modes are complicated linear functions of the perturbation amplitudes.

The system is stable, if both $Re[\omega^l], Re[\omega^t] < 0$. In this case, any random perturbation over the reference steady state tends to decay and relax asymptotically to the base state in time. On the other hand, the system is unstable if the real part of at least one of the previous growth rates is positive. In this case, a random perturbation will produce the emergence of the most unstable mode.

We will assume from now on that $\nu_1 > 0$, as discussed in Section 4.4.3. It is important to remark that $\omega^t(q_x = 0, q_y = 0) = 0$ as a consequence of the invariance of the physical model to global rotations. We can take advantage of this property to compute a necessary condition for the transversal modes to be unstable, which reads

$$\zeta \Delta\mu < \frac{-2\xi L_c^2}{\bar{\gamma}_1(\nu_1 - 1)} + \frac{T_0^2 \bar{\gamma}_1 \nu_1}{4\xi}.$$

This imposes that the origin of the real part of the growth rate ω^t is either a saddle point or a minimum. Therefore, it sets an upper bound on the active stress coefficient below which some transversal modes become unstable. For the typical values of the parameters on epithelial monolayers, the upper bound is of the order of 1000 Pa (if we assume that $\nu_1 \approx 10$), and therefore it is positive and consequently any active contractile stress coefficient would satisfy the previous inequality. With respect to the instability threshold of the longitudinal modes, it turns out to be the same as in the case of a $1d$ system, given by Eq. (4.23). We can conclude that in the range of parameters representative of epithelial monolayers, the transversal modes become unstable before the longitudinal modes. Nevertheless, the experimental observations suggest that the longitudinal modes are

linearly unstable as well [109]. From now on, we will assume that the active stress coefficient is smaller than the instability threshold (4.23), which sets the active stress coefficient far away from the previous upper bound associated to the stability of the transversal modes. Consequently, under these conditions, the system would be unstable to longitudinal and transversal perturbations, as it can be seen in Fig. (4.20). Transversal modes, however, grow faster.

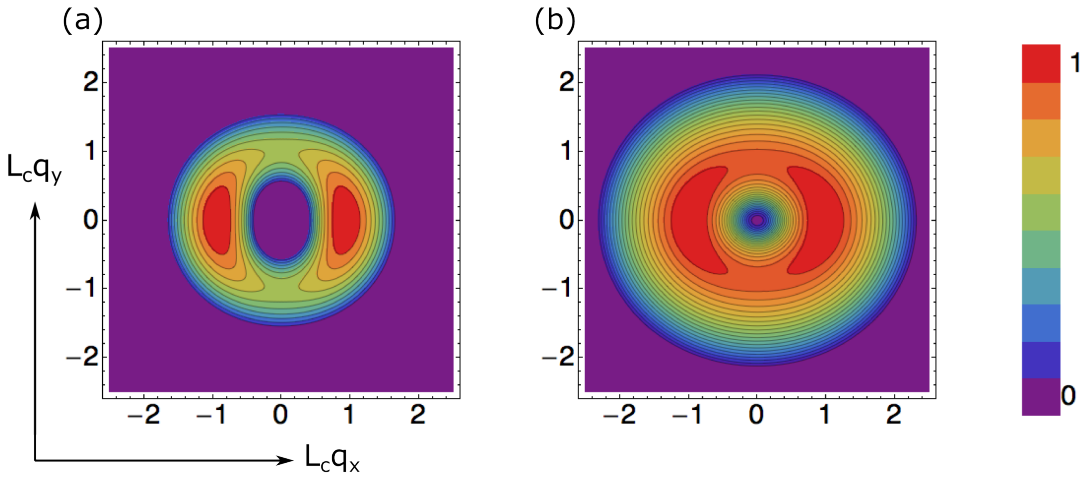

Figure 4.20: Characterisation of the linear dynamics of a random perturbation. (a) Colormap in the plane (q_x, q_y) of the real part of the growth rate of the longitudinal modes normalised by its maximum value, $max_{\mathbf{q}}(Re[\omega^l]) \approx 0.15/\text{min}$, (b) Colormap in the plane (q_x, q_y) of the real part of the growth rate of the transversal modes normalised by its maximum value, $max_{\mathbf{q}}(Re[\omega^t]) \approx 0.42/\text{min}$. The values of both figures are in units of $\xi = L_c = \bar{\gamma}_1 = 1$. The values of parameters are: $\eta = 10^6$ Pa·s, $\xi = 100$ Pa·s/μm^2 , $T_0 = 10$ Pa/μ, $L_c = 50$ μm, $\bar{\gamma}_1 = 600$ s, $\nu_1 = 10$, $\rho = 10$ Pa and $\zeta\Delta\mu = -2000$ Pa. Only the positive values of the growth rate are shown in both figures.

We want to examine in more detail the characteristic properties of the most unstable mode. Based on the information provided in Fig. (4.20), one can conclude that, if the wavenumbers are not limited by any geometrical constraint, the most unstable mode is transversal, and specifically its wavenumber is $q_y^c = 0$. Therefore, we will study the growth rates limited by the extra condition $q_y = 0$, in order to simplify the analysis

In our case, by solving the latter system of linear equations, one would obtain that

$$Re[\omega^t(q_x)] = -\frac{L_c^2 q_x^2}{\bar{\gamma}_1}\left(1 + \frac{q_x^2\bar{\gamma}_1(\nu_1^2-1)\rho}{4\xi(1+L_\eta^2 q_x^2)}\right) - \frac{q_x^2(\nu_1+1)\zeta\Delta\mu}{2\xi(1+L_\eta^2 q_x^2)}, \quad (4.29)$$

$$\frac{Im[\omega^t(q_x)]}{q_x} = -\frac{T_0}{\xi}\left(1 + \frac{(1+\nu_1)/2}{1+L_\eta^2 q_x^2}\right). \quad (4.30)$$

On the other hand, ω^l is given by Eqs. (4.21-4.22).

It is important to recall that the present model contains two different active contributions, T_0 and $\zeta\Delta\mu$. Remarkably, both active mechanisms affect differently the dynamics of small perturbations on the polarized state.

Near the critical point given by Eq. (4.23), if the wavenumbers are not limited by a finite size constraint, an arbitrary small $2d$ perturbation over the polarized homogeneous state will approach asymptotically in time, a wave-like transversal wave with a characteristic wavelength and traveling speed given by $\lambda^c = 2\pi/q^c$ and $V^c = -Im[\omega(q_t^c)]/q^c$, respectively. In the limit of $L_c \ll L_\eta$ and $\nu_1^2\bar{\gamma}_1\rho \ll \eta$ (i.e. $G, H \ll 1$), they read

$$q^c \approx \frac{2^{1/4}(1+\nu_1)^{1/4}}{\nu_1^{1/4}\sqrt{L_\eta L_c}}, \tag{4.31}$$

$$\frac{V^c}{T_0/\xi} - 1 \approx \frac{(1+\nu_1)L_c}{2\sqrt{2}L_\eta}. \tag{4.32}$$

The exact functional form of the previous expressions is complicated. In Figure (4.21), we display them upon variation of two dimensionless parameters, $H = \nu_1^2\bar{\gamma}_1\rho/\eta$ and $G = L_c/L_\eta$, that were defined in Section 4.4.3.

Interestingly, the wavenumber provided by this mechanism is quite robust to the change of ν_1. Moreover, it is worth emphasizing that the dependency on the physical parameters is similar to that of the most unstable mode in a $1d$ system near the onset of instability (see Fig. (4.12)).

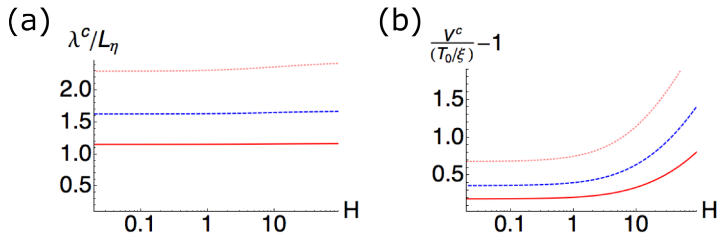

Figure 4.21: Characteristic quantities of the linear mechanical transversal waves. (a) Characteristic wavelength and (b) Travelling speed as a function of H. The solid red, dashed blue and dotted pink curves correspond to the values of $G = 0.05$, 0.1 and 0.2. In (c) $\nu_1 = 10$. Remind that $H \equiv \bar{\gamma}_1\nu_1^2\rho/\eta$ and $G \equiv L_c/L_\eta$ are defined in Section 4.4.3.

Discussion and qualitative experimental comparison

In the previous linear perturbation analysis of the homogenous polarized state for a $2d$ system, it was assumed that the wavenumbers were unconstrained. Nevertheless in the experimental conditions from Ref. [109], the epithelial monolayers

were allowed to migrate along a strip of a finite controlled width. In order to interpret their observations correctly, it is necessary to account for finite-size effects. The role of the geometrical confinement in the reported collective cell migration patterns can be understood qualitatively as discussed below.

We assume that the monolayer is essentially a $2d$ flat system, and orient the cartesian coordinate such that the x direction is parallel to the longitudinal direction of the strip. As we have seen above, the perturbations over the homogeneous polarized state have associated a wavenumber (q_x, q_y). Moreover, we identified two subsets of characteristic perturbations, that where defined as longitudinal and transversal. The geometrical constraints as well as the boundary effects provides a selection rules over the family of possible perturbations. In the case of the longitudinal perturbations, the component of the wavenumber q_x in a first approximation we assume that is unaffected by the geometrical constraints, contrarily to the component of the wavenumber q_y , whose only possible values are the harmonics of $q_y = \pi/L$ and $q_y = 0$, being $2L$ the width of the strip. The same restrictions apply to the possible wavenumber for the transversal perturbations, except that the wavenumber $q_y = 0$ is not allowed.

In the case of the strip of 20 μm width, although the most unstable mode is transversal for an infinitely extended $2d$ system, the geometrical constraints only allow a subfamily of transversal modulations, whose growth rate is smaller than the one corresponding to the most unstable longitudinal mode in a $1d$ system. Therefore asymptotically the system would evolve into one of the solutions presented in the phase diagram of Fig. (4.14).

In the case of the strip of 100 μm width, a small subset of the transversal perturbations of the physical observables grows linearly faster than the most unstable longitudinal mode in a $1d$ extended system. On the contrary, at an intermediate width between 20 to 100 μm, only a single transversal perturbation would belong to the latter subfamily, and consequently the system should display a transversal propagating wavy pattern. The number of unstable transversal modes is so reduced, however, that the velocity maps are not actually displaying vortex-like structures.

In the case of the strip of 400 μm width, the previous analysis is unable to provide a simple answer for the long time limit. The dynamics of the system are controlled by the nonlinear couplings between the unstable transversal modulations, which seems to lead to vortex-like collective motion in the tissue.

In conclusion, the physical scenario proposed in Section 4.5.1 seems to be consistent with the experimental observations. A deeper detailed analysis should be made on the characterization of the nonlinear periodic patters predicted by the model for the $2d$ extended system, in order to confirm the previous qualitative

picture, specially to test the predictions on the patterns observed for a 400 μm strip. Moreover it would be interesting to account for realistic boundary conditions to describe the system of collective migrating cells in confined geometries [109].

4.6 Final discussion and conclusions

In this chapter, we developed a physical model for expanding epithelial monolayers that relies on the active gels theory. Our objective was to construct a unified framework that captured a broad spectrum of the observed phenomena. In that sense, we investigated three different aspects of the mechanical behavior of expanding cell monolayers.

First, in a simple phenomenological attempt to interpret the complex spatio-temporal evolution exhibited by expanding cell sheets, we apply our coarse-grained approach to data from experiments on expanding epithelial monolayers. The method used provides a set of effective physical parameters that evolve in time. Despite the simplicity of the model, it turns out to be sufficient to capture the variety of shapes in the stress and velocity profiles for the two different types of cells considered: MDCK and MCF10a. Consequently, the temporal evolution of the physical observables is translated into the trajectories in a four parameter space: the active traction forces, the nematic correlation length, the effective viscosity and the cell-substrate friction coefficient. The monotonic increase of the nematic correlation length suggests that at the central region of the monolayers occurs a re-orientation of the cells towards the closest free-edge. This mechanism permits to accumulate the traction forces produced by single cells and produce an increasing total traction favoring the expansion of the monolayer. We were able to access the rheological properties of these cell sheets at time scales within the range of $10-1000$ min. The values of the effective viscosity spans a broad range of several orders of magnitude, from $\sim 10^4$ Pa·min for the blebbistatin-treated MDCK cells to $\sim 10^6$ Pa·min for MCF10a cells. The time dependence of the effective viscosity can be interpreted as a result of non-Newtonian effects, and can be accounted for with simple viscoelastic models. Nevertheless, the present of active stresses can also play a nontrivial role in modifying the rheological properties.

Secondly, we focus on the understanding of the mechanism that controls the mechanical oscillations reported in Ref. [51]. We generalize the previous physical model to incorporate the stresses produced by the active contraction of the cell cytoskeleton via myosin motors. For the theoretical analysis, we consider a homogeneous polarized state, assuming that this is the one energetically favored, in contrast to the assumption on the simple physical model from the first part of the chapter. In the latter it must be taken into account that an average over the

transversal direction was involved, so this case had to allow an effectively vanishing polarization in the 1d description. This was phenomenologically incorporated by energetically favoring the isotropic state. The precise mechanism that conciliates the two cases however, has not been worked out in detail. In this second case, we have unveiled an oscillatory spatially-periodic instability, allowing for the propagation of mechanical waves across the system. The two active contributions, traction and contractility, play a fundamentally different role: one the one hand the threshold of the instability is controlled by the activity of myosin motors. On the other hand the active traction forces control the traveling velocity of the mechanical waves. We explored numerically the different types of nonlinear solutions approach by random initial perturbations of base state. In particular we found two qualitatively different profiles, soliton-like solutions and nonlinear traveling waves. We also derived the amplitude equation description of our system obtaining explicitly the dependence of the parameters of the Complex Ginzburg-Landau equation on the physical parameters of our model, allowing for a complete classification of the possible dynamical behaviors near the onset of instability.

In the third part we have investigated the $2d$ oscillatory patterns in the cell sheets. We reveal a spontaneous Frederiks-like transition in confined epithelial monolayers, which share some similarities with the spontaneous flow transition predicted in active suspensions, [17]. In particular the threshold of the instability is controlled by the activity of the myosin molecular motors. We compare qualitatively our results with the work from Ref. [109] and provide a theoretical explanation of the observations for different transversal confinement of the tissue.

Based on our results there are several physical pictures that might explain the experimental data reported in Ref. [51]. The two possible scenario that we propose are the following:

1. The system is in the linearly stable region of parameter space, but the initial adaptation of the system to the removal of the geometrical constraints introduces large fluctuations that can prompt migration modes, otherwise unobservable, that decay with time. In particular, the two stress fronts that initiate at the free edges and propagate inwards and collide at the central region, could be a sufficiently large perturbation to excite the transient wave modes. This scenario would be essentially insensitive to the size of the initial mask in both dimensions.

2. The system is in the linearly unstable region of parameter space. At early stages it essentially behaves as a $1d$ system due to the initial configuration chosen in Ref. [51]. Nevertheless, the steady polarized state is linearly unstable to longitudinal as well as transversal perturbations. Consequently, at

the beginning of the experiment the longitudinal modes are spontaneously activated, whereas at a later time the transversal modes take over and become dominant. In this scenario the system visits different states, changing from longitudinal mechanical waves to a disordered migration state with large vortices. This second scenario is clearly sensitive of the initial system size in the two dimensions.

A deeper and more complete study of the $2d$ pattern formation mechanisms, and in particular on the possible nonlinear dynamical scenarios is still necessary to reach a better theoretical understanding of the dynamics of expanding epithelial tissues. On the other hand, experiments exploring the dynamical behavior for different aspects ratios of the masks and possibly other geometries could help elucidating the different possible scenarios in the light of our theoretical framework.

Acknowledgments:

We thank E. Bazellières, V. Conte, X. Serra-Picamal, R. Vincent and X. Trepat for enriching discussions. The work from Section 4.2 has been done in collaboration with the group of X. Trepat, who performed the experimental measurements on the epithelial monolayers.

Chapter 5

General conclusions and perspectives

5.1 Overview

In this thesis we have addressed the dynamics of different mechanical processes in living matter with focus on mechanical instabilities. The theoretical approach of the thesis has been two-fold. In the problems of spontaneous motility of cell fragments and on the shapes of growing tissues, the focus has been put on the search for general physical principles and mechanisms through a deep analysis of minimal models rather than in a realistic biological description. In the problem of epithelial tissues the comparison with experiments played a prominent role. This study was directly motivated by recent experimental data, and the emphasis has been put in the development of models that allow to interpret and explain the experimental observations and possibly gain insights that may lead to further experiments.

We consider a trademark and leitmotif of this thesis the pursuit of dynamic instabilities beyond the linear regime. In this thesis we have proven in the case of lamellar fragments that a nonlinear analysis may become necessary to address fundamental aspects. In particular the use of concepts from bifurcation theory and center-manifold reduction has been crucial to prove the spontaneous motility of fragments through a nonlinear morphological instability mechanism. Also, in the 1d instability of polarized tissues with both contractile and traction active stresses, the weakly nonlinear analysis leading an amplitude equation of the Complex Ginzburg-Landau form has allowed to identify the universal nonlinear physics that polarized epithelia may share with very different physical systems. In our problem this has allowed to classify the possible nonlinear dynamic scenarios in correspondence to the actual physical parameters.

The study of the nonlinear physics in living matter has been also pursued beyond the weakly nonlinear analysis, in some cases with exact results, such as in problems that are amenable to conformal mapping techniques. Whenever necessary, the fully nonlinear regime has been studied numerically, using different techniques and in some cases involving extremely high-precision numerics. The analytical work in weakly nonlinear expansions has also been assisted by the use of symbolic calculus software.

5.2 Summary of results and conclusions

In this section, we briefly revisit the main results and conclusions of this thesis:

- In Chapter 2, we have formulated using conformal mapping techniques the free-boundary problem presented in Ref. [55], which was proposed to study the morphological instability of lamellar fragments. This formalism provides us with a convenient framework to extend the interfacial dynamics into the nonlinear regime. We have developed a numerical method that allows us to integrate the temporal evolution of the morphological changes of the interface of the active droplets, and also another numerical method to compute branches of steady shapes. Combining both of them, we have explored the behavior of the system in a neighborhood of the phase space around the steady circular solution. A complex subcritical bifurcation scenario into traveling solutions has been unfolded. The traveling velocity is conferred via a non-adiabatic mechanism, and so it cannot be detected neither through linear analysis nor a weakly nonlinear expansion of the steady circular shape. Complementary, we have performed a weakly nonlinear analysis at referential bifurcation points of the circular steady solution, by means of which we could prove the existence of a nonlinear instability of the centre of mass and compute analytically families of steady nonlinear solutions. This study proves that polymerization forces alone are sufficient to drive motion through a nonlinear morphological instability, a point that was controversial in the literature. Spontaneous symmetry breaking is thus capable to initiate and sustain motion, in the absence of molecular motors, global actin polarization and other explicit forms of symmetry breaking.

  In addition, we have derived an exact expression that relates the center of mass velocity to the shape of the active droplet. This remarkable and simple result has also been extended to more general situations, including other types of boundary conditions, the presence of molecular motors, non-Darcyan flow, presence of external forces, and other mechanical properties of the membrane.

- In Chapter 3, we have studied and classified the time-dependent morphologies of polarized tissues subject to anisotropic but spatially homogeneous growth. Extending previous studies, we model the tissue as a fluid, and discuss the interplay of the active stresses generated by the anisotropic cell division and three types of passive mechanical forces: viscous stresses, friction with the environment and tension at the tissue boundary. The morphology dynamics is formulated as a free-boundary problem, and conformal mapping techniques are used to solve the evolution numerically. We combine analytical and numerical results to elucidate how the different passive forces compete with the active stresses to shape the tissue in different temporal regimes and derive the corresponding scaling laws and crossovers between regimes. We show that in general the aspect ratio of elongated tissues is non-monotonic in time, eventually recovering isotropic shapes in the presence of friction forces, which are asymptotically dominant. Consequently, the aspect ratio in general shows a maximum at finite time, for which we give simple scaling laws which depend on the physical parameters of the tissue.

- In Chapter 4, we have developed a physical model for expanding epithelial monolayers that relies on the active gels theory, capable to reproduce a broad spectrum of the phenomenology observed in these systems, such as the spatio-temporal evolution of the mechanical $1d$ patterns, the propagation of apparently elastic waves or the transition to $2d$ behavior in confined epithelial monolayers.

  We have applied our physical model in expanding cell cultures. The predicted stress and velocity profiles are sufficient to capture the variety of profiles of the same physical observables for two different type of cells: MDCK and MCF10a. We extract a set of physical parameters at each time point, the trajectories of which reflect the temporal evolution of the profiles of the physical observables as the cell sheets expands. We are able to access the rheological properties of these cell sheets at time scales within the range of $10 - 1000$ min. The values of the effective viscosity span a range of several orders of magnitude, from $\sim 10^4$ Pa·min for the blebbistatin-treated MDCK cells to $\sim 10^6$ Pa·min for MCF10a cells. We detected non-Newtonian effects, specially manifested in MDCK cells, which can be accounted for with simple viscoelastic models. An interesting point is the explanation of the apparently elastic waves an an active effect in a systems that is otherwise fluid.

  In the second part, we have focused on the understanding of the mechanisms that control the mechanical oscillations reported in Ref. [51]. We

generalize the previous physical model, incorporating the internal stresses produced by the active contraction of the cytoskeleton via myosin motors. We have unveiled an oscillatory periodic instability, in which the two active components of the model play a fundamentally different role: on the one hand the threshold of the instability is controlled by the activity of myosin motors. On the other hand the active traction forces control the traveling velocity of the mechanical waves. We classified the asymptotic nonlinear profiles from random initial small perturbations of the steady state. In particular, we have detected two qualitatively different profiles, a soliton-like profiles and nonlinear traveling waves. We have also performed a weakly nonlinear analysis of this instability by deriving the corresponding Complex Ginzburg-Landau equation. We have explicitly found the mapping between the physical parameters and those of the CGL equation, thus allowing for a complete classification of the possible dynamical scenarios in the region near onset.

Finally, we have investigated $2d$ oscillatory patterns in the cell sheets. We have found a new instability in confined epithelial monolayers that exhibits some similarities with the Frederiks-like spontaneous-flow transition predicted for thin active polarized gels [17] and not yet observed. In particular the threshold of the instability is controlled by the activity of the myosin molecular motors, and the width of the transversal confinement plays also an important role. This is a transversal instability that coexists with the longitudinal one discussed above. The combination of both provides a scenario whether a broad series of experimental results from different groups can be interpreted.

5.3 Publications

Some results of this thesis have already been published, but a large part is not yet published at the time of writing this thesis. The two published papers are

- Blanch-Mercader C., and Casademunt J., "Spontaneous motility of actin lamellar fragments" Phys. Rev. Lett., 110: 078102, (2013).
- Blanch-Mercader C., Casademunt J., and Joanny J.F. "Morphology and growth of polarized tissues", Eur. Phys. J. E, 37: 41, (2014).

The first one contains the main results exposed in Chapter 2, and the second one includes the full contents of Chapter 3. A more exhaustive and complete presentation of the results of Chapter 2 are included in a longer manuscript that is about to be submitted to Physical Review E:

- Blanch-Mercader C. and Casademunt J. "A nonlinear mechanism of cell motility in lamellar actomyosin fragments"

The results discussed in Chapter 4 are planned to be published in at least two different papers. A short one in letter format is in preparation including the 1d model in combination with the experiments of Trepat's group, with emphasis on the comparison between theory and experiment and the the use of the theory to interpret the data. A second purely theoretical is in preparation and will discuss the two instabilities driven by active forces, leading to longitudinal elastic-like waves in a fluid tissue, and the Frederiks-like one in confined geometries, including the weakly nonlinear analysis of the first one. Together these will be used to interpret a variety of experimental observation from different groups. The two above manuscripts that are in preparation with the contents of Chapter 4 are:

- Blanch-Mercader C., Vincent R., Bazellières E., Serra-Picamal X., Trepat X. and Casademunt J. "Mechanical properties of expanding epithelial monolayers"

- Blanch-Mercader C. and Casademunt J., "Mechanical oscillatory instabilities in epithelial cell monolayers."

5.4 Perspectives

The problem of the spontaneous motility of cell fragments has been essentially closed from the point of view of searching for minimal models and analytical insights onto the role of different ingredients. Continuations of our approach should necessary include a variety of neglected ingredients such as the dynamics of polarization, the effect of molecular motors and in general the no homogeneous distribution of the different ingredients. The next step should thus focus on a more realistic description of actin-based motility in different situations. Such a realistic description, including large-scale numerical simulations, phase-field models etc have already been developed by other groups in recent years, so we do not plan to pursue this line in depth except possibly in the use of the exact relations derived for general cases for the interpretation of existing experimental data. A continuation of this problem that is already in progress in collaboration with Sérgio Lira, is the formulation of a phase-field model for the minimal free-boundary problem here studied. The interest of this is two-fold. From a practical point of view, to develop a more standard and competitive framework for numerical simulation. From a theoretical point of view it allows to incorporate a finite viscosity

of the surrounding fluid, which is likely to modify significantly the dynamics of the problem.

With regard to the study of the interplay of the different sources of active and passive stresses in the shape evolution of polarized tissues, we foresee different possible extensions that may bring new insights. Among the simplified hypothesis that we should relax we highlight that of the independence of the expansion rate on the pressure. Including the coupling between the stress environment and the expansion rate is possibly the most interesting point to be studied in the near future.

The area of our research that we see with most potential of continuation and highest expectation of breakthrough in the pursuit of the mechanical point of view in the dynamics of tissues, with emphasis on the role of active stresses and in particular in the identification of instabilities. The ones we have already found still require a deeper study, in particular the transversal Frederics-lke wave, which we still have to pursue beyond the linear regime. The combination of both longitudinal and transversal instabilities in confined epithelial tissues in 2d is one of the important challenges that remain open. The instability of the nonlinear elastic-like waves to long-wavelength transversal modulations can be studied in the context of the CGL equation. The combination of the two instabilities discovered in the problem including their nonlinear couplings is likely to provide new insights that may lead to explain the apparent turbulence of the flows of such epithelial tissues, and possibly connect this to the presence of spatio-temporal chaos.

Chapter 6

Resum en català

Aquesta tesi s'emmarca dins de l'àmbit de la biofísica, en particular en l'estudi de la física de processos biològics a escala cel·lular i multicel·lular que involucren fenòmens col·lectius d'auto-organització. El formalisme teòric emprat modela els sistemes biològics com un gel actiu. Aquest tipus de materials ideals són intrínsecament fora de l'equilibri termodinàmic, com a conseqüència de la seva capacitat per consumir energia química del medi extern. Dins d'uns certs marges, sovint entesos de forma abstracta, les cèl·lules, el citosquelet d'actina, els teixits, els organismes,etc. comparteixen les mateixes propietats materials que un gel actiu. El nostre plantejament es basa en la hipòtesi que el sistema biològic en el límit d'escales de longitud grans i temps llargs està ben descrit per un nombre reduït de camps continus, com la densitat de cèl·lules o la velocitat dels monòmers d'actina. La teoria de gels actius és una generalització natural de la teoria hidrodinàmica dels cristalls líquids. Una de les propietats que s'utilitza de forma recurrent durant la tesi és la universalitat de les equacions constitutives d'aquests materials ideals, i per tant ens permet aplicar el mateix formalisme a medis aparentment diferents. Sota certes aproximacions addicionals en cada cas específic, ens hem centrat en els següents casos: la locomoció sostinguda en fragments cel·lulars, l'expansió lliure d'una mono-capa de cèl·lules epitelials i l'evolució dinàmica de la forma de l'ala de la mosca *Drosophila melanogaster*.

La tesi està estructurada de la següent forma:

- En el capítol 2, mostrem com un fragment cel·lular és capaç de desplaçar-se de forma sostinguda, solament amb les forces de polimerització a la membrana cel·lular, si inicialment s'indueix un trencament espontani de la simetria rotacional. Per tant, els mecanismes relacionats amb els motors moleculars o amb la polaritat global del citosquelet no són necessaris pel procés de locomoció cel·lular, tot i que poden coexistir amb l'anterior mecanisme.

El nostre estudi està basat en l'anàlisi dèbilment no-lineal d'un model previ (ideat, pensat) per a fragments cel·lulars. Per una banda, demostrem la inestabilitat no-lineal del centre de masses d'un gel actiu circular i també derivem una expressió exacta i genèrica entre la forma i la velocitat instantània del centre de masses. Per altra banda, posem de manifest una estructura complexa de bifurcacions sub-crítiques a solucions mòbils, on les velocitats s'originen a través d'un mecanisme no-adiabàtic. Exemples de solucions mòbils i la seva estabilitat s'estudien numèricament mitjançant les tècniques de *conformal mapping*.

- En el capítol 3, estudiem i classifiquem l'evolució temporal de les morfologies d'un teixit totalment polaritzat, el qual està sotmès a un creixement anisòtrop però espacialment homogeni. Estenem estudis teòrics previs, incorporant els efectes generats per la interacció entre els esforços actius produïts per la divisió cel·lular i tres tipus de forces passives: de tipus viscós, de fricció amb el medi extern i de capil·laritat. La dinàmica de la forma de l'ala de la mosca *Drosophila melanogaster* pertany a la categoria de problemes de contorn lliure, i per tant apliquem tècniques de *conformal mapping* per resoldre-la numèricament. Combinem resultats analítics i numèrics per entendre els efectes de cada força passiva sobre la forma del sistema. Finalment, demostrem que en general l'excentricitat d'un teixit allongat evoluciona de forma no-monòtona amb el temps. Eventualment les forces de fricció són dominants i indueixen que la forma del teixit tendeixi a ser isòtropa. Per tant. l'excentricitat presenta un màxim a temps finit, del qual hem estudiat les lleis d'escala amb les paràmetres físics del model.

- En el capítol 4, estudiem la migració col·lectiva en un teixit cohesiu de cèl·lules epitelials que s'expandeix sobre d'un substrat elàstic. Aquest fenomen involucra la coordinació de les forces de tracció, les quals es transmeten mecànicament a les cèl·lules veïnes mitjançant adhesions entre elles. Els mapes de les forces intra-cel·lulars mostren una distribució espacio-temporal complexa i heterogènia. Per ajudar a entendre les propietats físiques i biofísiques d'aquest tipus de teixits, que sorgeixen dels fenòmens col·lectius inherents, proposem una descripció contínua del sistema com si fos un fluid polar i actiu, el qual incorpora forces de tracció actives amb el substrat. Els perfils d'esforços i velocitat es comparen directament amb les dades experimentals obtingudes pel grup del Prof. X. Trepat per a mono-capes epitelials formades per cèl·lules MDCK o MCF10a. Mitjançant aquesta anàlisi podem derivar l'evolució temporal de la força de tracció activa per cèl·lula, la correlació nemàtica del medi i la seva viscositat efectiva a escales de temps entre $10 - 1000$ min.

En la segona part del capítol 4, generalitzem les equacions constitutives de l'anterior fluid polar actiu, incorporant nous efectes com els esforços contràctils generats per l'activitat en la xarxa d'actomyosina connectada entre cèl·lules a través de les unions d'adherència. En aquest cas, analitzem la dinàmica de pertorbacions aleatòries sobre l'estat homogeni i polaritzat. En el règim lineal hi ha una inestabilitat oscil·latòria i periòdica on els dos elements actius del model físic controlen aspectes qualitativament diferents de la bifurcació. Per una banda, el llindar de la inestabilitat depèn dels esforços contràctils i per altra banda, les forces de tracció actives controlen la velocitat de propagació de les ones mecàniques. és important remarcar que els materials actius permeten sostenir ones elàstiques, fins i tot si les propietats reològiques i passives del medi són de tipus viscós. Posteriorment classifiquem les solucions en el límit asimptòtic de temps llargs en un únic diagrama de fases restringit a valors realistes dels paràmetres en condicions estàndard de les mono-capes epitelials. Finalment, estenem l' anàlisi a un sistema 2-dimensional, però ens limitem a caracteritzar la dinàmica lineal de pertorbacions aleatòries al voltant de l'estat homogeni i polaritzat.

Chapter 7

Appendices

7.1 Appendix A: Center manifold reduction of a dynamical system

The present section is a brief introduction to the mathematical grounds upon which the discussion of the model for cell fragments is based. For a more exhaustive review on the center manifold reduction, we refer the reader to [73, 132].

Let us assume a separable dynamical system of the form

$$\begin{aligned} \dot{a}_c &= L_c a_c + N_c(a_c, a_s, a_u), \\ \dot{a}_s &= L_s a_s + N_s(a_c, a_s, a_u), \\ \dot{a}_u &= L_u a_u + N_u(a_c, a_s, a_u), \end{aligned}$$

with a fixed point at the origin, where a_c, a_s and a_u denote each one a set of real variables. The functions L_c, L_s and L_u describe the linearized dynamics around the fixed point, whereas N_c, N_s and N_u are nonlinear functions of the variables. The subindices c, s and u stand for the three components in which the tangent space at the fixed point can be split: central (or marginal), stable and unstable respectively, each one with an arbitrary dimension. The eigenvalues associated to the matrices L_c, L_s and L_u can be complex but its real part should be by definition zero (or nearly zero), negative and positive respectively. Any dynamical system having a fixed point admits this form after a linear change of variables that splits the eigenvariables of the linearized problem in these three groups, without loss of generality. In the case that the dynamical system depends on a control parameter, all the eigenvalues are functions of it. In that case, nearly marginal means that the free parameter takes values sufficiently close to a critical value at which one of the eigenvalues of L_c becomes strictly marginal. Each variable has a characteristic

time scale that controls its dynamics around the fixed point, given by the inverse of the real part of the corresponding eigenvalue. In the usual physical language it is stated that in a neighborhood of the fixed point and the critical value of the control parameter, there is a separation of time scales between the central (slow) variables and the (fast) stable variables, which may be assumed to be "slaved" to the slower evolution of the central variables. In mathematical terms this idea is phrased differently. In a neighborhood of the fixed point, a local algebraic relationship between the central variables and the rest of variables defines the so-called center manifold, which is an invariant set for the nonlinear dynamics. That is, the evolution remains within this manifold. We can express the center manifold in terms of he functions $a_s = h_s(a_c)$ and $a_u = h_u(a_c)$. In Fig. (7.1), we show a geometric representation of the center manifold.

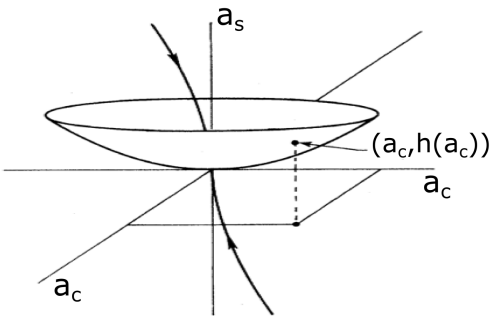

Figure 7.1: Illustrative projection of the phase space onto two marginal variables (represented by the same label a_c) and one stable variable (represented by a_s). The arrow shows a trajectory of the system. The surface parametrized as $(a_c, h_s(a_c))$ is a center manifold. Modified from Ref. [73]

The functions h_s and h_u are determined by the condition of invariance of the center manifold, thus satisfying the equations

$$\begin{aligned} \dot{a}_c \partial_{a_c} h_s &= L_s h_s + N_s(a_c, h_s, h_u), \\ \dot{a}_c \partial_{a_u} h_u &= L_u h_u + N_u(a_c, h_s, h_u), \end{aligned}$$

with the boundary conditions $h_s(0) = h_u(0) = \partial_{a_c} h_s(0) = \partial_{a_c} h_u(0) = 0$, which imply that the center manifold is tangent at the origin to the manifold $(a_c, 0, 0)$. The center manifold-reduction theorem states that in a neighborhood of the fixed point the trajectories of the original system are homeomorphic to the trajectories

of the a dynamical system of the form

$$\dot{a}_c = L_c a_c + N_c(a_c, h_s(a_c), h_u(a_c)), \tag{7.1}$$
$$\dot{a}_s = L_s a_s, \tag{7.2}$$
$$\dot{a}_u = L_u a_u. \tag{7.3}$$

The means that the above dynamical system is qualitatively (topologically) equivalent to the original one. This result was proved by [135] in the case that there are no unstable variables and afterwards it was generalised by [136] allowing for unstable variables and variation of the control parameters in a neighborhood of the critical value (suspended systems). The first equation (7.1) describes the dynamics of the original system for initial perturbations within the center manifold, whereas Eqs. (7.2,7.3) describe the dynamics of the original system for initial perturbations transverse to the center manifold. This remarkable result implies that all the inherently nonlinear structure of the original equations (that cannot be eliminated by a change of variables) including the bifurcation structure and any nontrivial dynamics, is contained in the center manifold, which in turn is of a relatively reduced dimension. If the initial conditions that are close but outside the center manifold (transversal components of the flow) they either relax exponentially towards the center manifold (the stable transversal components) or move exponentially away from it (the unstable transversal components). In physics this result is often known as adiabatic elimination but it is usually applied to separate the slow dynamics of the nearly marginal modes from the stable ones in an instability near onset. In our proof of the nonlinear instability of a center of mass of the problem of cell fragments, we make use of the fact that also the growth of the unstable (non marginal) modes are qualitatively described by a linear growth, not modifying the bifurcation structure.

The center manifold is usually computed as an asymptotic expansion around the fixed point. By extension the dynamical system (7.1-7.3) is represented as an asymptotic series. The order of the expansion can be arbitrarily large. The next example illustrates this procedure and highlights some of the mathematical subtleties involved in this type of analysis.

Example: Let us assume the following dynamical system, in which we will compute the dynamics at the center manifold

$$\begin{aligned} \dot{x} &= -x^3, \\ \dot{y} &= -y - x^2, \\ \dot{z} &= z - x^2. \end{aligned}$$

The x is a central variable, y is a stable variables and z is an unstable variable

at the fixed point on the origin. Fig. (7.2) shows the trajectories of the latter dynamical system. It serves to illustrate that the stable variable y approaches the corresponding value at the center manifold $h_y(x)$, whereas the unstable variables z moves away from it. In this example, the center manifold can be computed

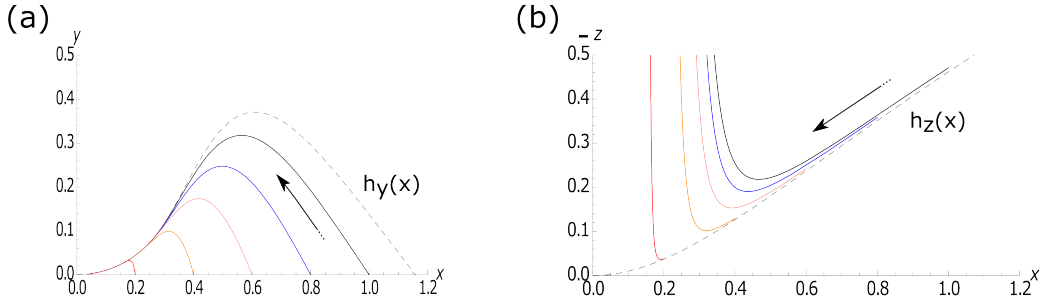

Figure 7.2: (a) Trajectories of the system in the phase space projected in the plane $x-y$ starting at the initial conditions $y(t=0)=0$ and (red) $x(t=0)=0.2$, (yellow) $x(t=0)=0.4$, (pink) $x(t=0)=0.6$, (blue) $x(t=0)=0.8$ and (black) $x(t=0)=1$. (b) Trajectories of the system in the phase space projected in the plane $x-y$ starting at the initial conditions $z(t=0)=1.02h_z(x(t=0))$ and (red) $x(t=0)=0.2$, (yellow) $x(t=0)=0.4$, (pink) $x(t=0)=0.6$, (blue) $x(t=0)=0.8$ and (black) $x(t=0)=1$.

exactly

$$\begin{aligned} h_y(x) &= Ce^{-\frac{1}{2x^2}} + \frac{1}{2}e^{-\frac{1}{2x^2}}\,\mathrm{Ei}\left(\frac{1}{2x^2}\right) = -x^2 + \mathcal{O}(x^3, e^{-\frac{1}{2x^2}}), \\ h_z(x) &= \frac{1}{2}e^{\frac{1}{2x^2}}\,\mathrm{Ei}\left(-\frac{1}{2x^2}\right) = -x^2 + \mathcal{O}(x^3, e^{-\frac{1}{2x^2}}). \end{aligned}$$

Remarkably, $h_y(x)$ is not unique due to the term $Ce^{-\frac{1}{2x^2}}$, since C is an arbitrary integration constant. Nevertheless, the latter term turns out to be equivalent to zero in an power series representation around the origin, since it vanishes to all orders. It is thus customary to select the center manifold that is formally analytic at the fixed, which it is unique. None of the crucial properties of the center manifold depends on this choice, so one may directly neglect exponentially small terms like $Ce^{-\frac{1}{2x^2}}$.

Then in a neighborhood of the fixed point at the origin, the dynamics can be approximated by

$$\begin{aligned} \dot{x} &= -x^3 + \mathcal{O}(e^{-\frac{1}{2x^2}}), \\ \dot{y} &= -y + \mathcal{O}(e^{-\frac{1}{2x^2}}, x^2), \\ \dot{z} &= z + \mathcal{O}(e^{-\frac{1}{2x^2}}, x^2). \end{aligned}$$

The exponentially small corrections have been made explicit to emphasize that,

even though they are not qualitatively relevant, in the sense of affecting the topological structure of the solutions, they may still play a significant role in possible non-adiabatic effects. The term 'non-adibatic' refers generically to all the effects that may be lost by the center-manifold reduction of the problem. We show in Chapter 2 an important example of non-adiabatic effect in the mechanism that endows the solutions of the problem of cell fragments with a finite velocity near a bifurcation points. In this case the non-adiabatic nature of the effect is manifested in the apparent exponentially small dependence of the velocity on the distance to the bifurcation. This fundamental point was elucidated numerically, but was missed by the center-manifold reduction of the problem.

7.2 Appendix B: Center manifold reduction for $\beta = \beta_2$ at higher orders

Here we write explicitly the dynamical equations that govern the temporal evolution of the cell fragment interface near the bifurcation point $\beta \sim \beta_2$ projected onto the corresponding centre manifold and expanded up to seventh order in ϵ, provided that the amplitudes of the normal modes a_1, a_2 and a and the distance to the bifurcation point $g_2 \equiv \beta - \beta_2$ are thought to be of the same order in ϵ.

$$
\begin{aligned}
\dot{a} &= 9a_1a_2g_2 + \left(18a_1a_2^2g_2 - 9a_1^3g_2 - \frac{27}{16}a_1a_2^3\right) \\
&+ \left(216a_1a_2^2g_2^2 + \frac{81}{16}a_1^3a_2^2 - 6a_1^3a_2g_2 - \frac{1053}{28}a_1a_2^3g_2 - \frac{27}{8}a_1a_2^4\right) + \mathcal{O}(\epsilon^6), \\
\dot{a}_1 &= 9a_1a_2g_2 + \left(63a_1a_2^2g_2 - 9a_1^3g_2 - \frac{27}{16}a_2^3a_1\right) \\
&+ \left(\frac{81}{16}a_1^3a_2^2 + \frac{459}{28}a_1a_2^3g_2 - 105a_1^3a_2g_2 - 216a_1a_2^2g_2^2 - \frac{189}{16}a_1a_2^4\right) + \mathcal{O}(\epsilon^6), \\
\dot{a}_2 &= -6a_2g_2 + \left(6a_1^2g_2 + \frac{9}{8}a_2^3\right) + \left(\frac{648}{7}a_2^3g_2 + 18a_1^2a_2g_2 - \frac{27}{8}a_1^2a_2^2\right) \\
&+ \left(\frac{27}{8}a_1^4a_2 + \frac{50058}{49}a_2^3g_2^2 + \frac{27}{8}a_1^2a_2^3 - 12a_1^4g_2 - \frac{2025}{14}a_1^2a_2^2g_2 - \frac{197811}{15680}a_2^5\right) + \mathcal{O}(\epsilon^6).
\end{aligned}
$$

7.3 Appendix C: Resultant and common roots of two polynomials

In this appendix, we define the mathematical concept of the resultant of two polynomials and its practical use in the exploration of the center manifold reduction

of the cell fragments problem in Chapter 2. For more details we refer the reader to the Ref. [137].

Given two polynomials $A(x)$ and $B(x)$, expressed in terms of their zeros $\mathtt{a}_i$ and $\mathtt{b}_j$ as

$$A(x) = a_n \sum_{i=0}^{n} (x - \mathtt{a}_i) \qquad B(x) = b_n \sum_{j=0}^{m} (x - \mathtt{b}_j)$$

the resultant of the polynomials $A(x)$ and $B(x)$ is defined as

$$\rho(A, B) = a_n^m b_m^n \prod_{i=0}^{n} \prod_{j=0}^{m} (\mathtt{a}_i - \mathtt{b}_j).$$

The resultant of the two polynomials is the determinant of the so-called Sylvester matrix associated to the polynomials $A(x)$ and $B(x)$ [137]. An important property of the resultant is that it is equal to zero if and only if the polynomials $A(x)$ and $B(x)$ have a root in common. This property will be exploited in the center-manifold reduction of the cell fragment problem, to control the generation of new stationary solutions as the order of the weakly nonlinear expansion is progressively increased.

7.4 Appendix D: Dynamics of the area and the center of mass of a tissue

In this section we calculate the dynamical equations for the area and the center of mass of a $2d$ tissue. Note that the argument can be generalized to $3d$ tissues. Both geometrical properties have their analogues in the harmonic moments formalism [71].

We start from the general result

$$\frac{d}{dt} \int_{\Omega} F(\mathbf{r}) da = \int_{\partial\Omega} F(\mathbf{r}) V_n dl. \tag{7.4}$$

V_n being the normal component of the velocity of the interface, (Eq. (3.7)). We use the physical model of tissues given by Eqs. (3.4,3.5) where the tissue is in the domain Ω and has a boundary $\partial\Omega$. The time evolution of the total area is governed by the equation

$$\frac{dA}{dt} = \int_{\partial\Omega} V_n dl = \int_{\Omega} \nabla \cdot \mathbf{v} da = k_c A. \tag{7.5}$$

where the left hand side accounts for the mass produced per unit time. The center

of mass position is defined in vectorial notation by $A\mathbf{R}_A = \int_\Omega (x,y) da$. Considering first the x component, we write

$$\begin{aligned}
\frac{d}{dt}\int_\Omega x da &= \int_{\partial\Omega} x V_n dl = \int_\Omega \nabla\cdot(x\mathbf{v})\, da, && (7.6)\\
&= \frac{1}{\xi}\int_\Omega \nabla\cdot\left(\sigma_{xx}^{tot}, \sigma_{xy}^{tot}\right) da + k_c \int_\Omega x da, && (7.7)\\
&= -\int_{\partial\Omega} \frac{\gamma}{\xi}\kappa\hat{n}_x dl + k_c\int_\Omega x da, && (7.8)\\
&= k_c \int_\Omega x da. && (7.9)
\end{aligned}$$

The same argument also holds for the y-component of the center of mass. The instantaneous velocity of the center of mass is thus

$$\dot{\mathbf{R}}_A = 0. \tag{7.10}$$

Since this result is exact for any shape of the tissue, we conclude that, within the assumptions of the model, the active stresses cannot drive a net displacement of the tissue. Note that this result is not trivial, because it is known that, in general, an active fluid in the presence of friction forces can indeed sustain motion provided that the shape of its boundary introduces an appropriate symmetry breaking, as discussed in Chapter 2 and in Ref. [91].

7.5 Appendix E: Self-similar tissue growth

In this appendix we review the particular case discussed in Ref. [82] where there are neither friction nor capillary forces (i. e. $\gamma = \xi = 0$). Any initial shape evolves in a self-similar fashion. However, the scaling factors (along and perpendicular to the orientation of the cells) differ as long as the active stresses are finite [82].

In the regime $\gamma = \xi = 0$, the tissue behaves as an incompressible Stokes flow with a free boundary. We assume that the polarization of the cells is homogenous across the tissue and parallel to the x-axis (i. e. $\mathbf{p} = \hat{e}_x$), and the dynamics of the interface is given by the kinematic condition (3.7).

The velocity field inside the tissue is given by $v_x = (k_c + \sigma_0/2\eta)x/2$, $v_y = (k_c - \sigma_0/2\eta)y/2$ and the pressure field is constant, $P = \eta k_c - \sigma_0/2$, where x and y are the cartesian coordinates. Importantly, this solution is independent of the instantaneous shape of the tissue.

We choose an arbitrary parametrization of a family of self-similar interfaces, $x = \lambda_x(t)x(s)$ and $y = \lambda_y(t)y(s)$, where $\lambda_y(t)$ ($\lambda_x(t)$) are the scaling factors in the

y and x directions respectively and $(x(s), y(s))$ is a parametrization of the contour of the initial shape. Combining these results, the evolution of the initial contour is specified by two dynamical equations for the scaling factors $\dot{\lambda}_x = (k_c + \sigma_0/2\eta)\lambda_x/2$ and $\dot{\lambda}_y = (k_c - \sigma_0/2\eta)\lambda_y/2$ [82]. The original contour therefore deforms self-similarly.

One of the implications of this result is that a tissue would preserve a memory of its initial shape while growing. It is worth mentioning that one cannot eliminate completely this effect by invoking only capillary forces (i. e. $\gamma \neq 0$), because their effects are negligible at length scales larger than L_c.

7.6 Appendix F: Thin layer approximation for a cell monolayer

In appendix we discuss in detail the approximation performed on the physical model to treat the epithelial cell monolayer as an effective $2d$ system.

The configuration of the system is the one shown in Fig. (7.3), in which the height (thickness) of the monolayer h is assumed to be much smaller than the length scales (l) that control the spatial variation in the plane parallel to the substrate (i.e. $\epsilon = h/l \ll 1$). For simplicity, we will assume that the system is translationally invariant along the longitudinal direction, which eliminates the dependencies of the physical observables on the y cartesian coordinate. We will assume further that the local height of the monolayer h may evolve over time but remains approximately constant throughout the tissue, in other words we impose $\partial_x h \ll 1$ based on experimental evidence (see Fig. (7.4,b)).

The z coordinate takes the value $z = 0$ at the level of the substrate and $z = h$ at the upper surface of the monolayer.

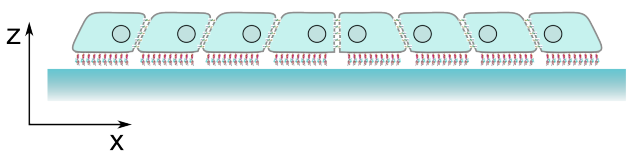

Figure 7.3: Schematic drawing of an epithelial monolayer in space. Cells are placed on top of an elastic substrate and are able to form cell-cell and cell-substrate junctions. For more details on the experimental conditions, see Ref. [51]

In the absence of external forces the reference state corresponds to the equilibrium configuration with $\mathbf{v} = 0$ and $P = P_{ext}$, in which there are neither internal fluxes nor pressure gradients.

The cell traction forces act as external forces on the monolayer (T_x) and will be accounted for in the model through a boundary condition, $\sigma_{xz} = T_x|_{z=0}$. On the other hand, we impose that $v_z = 0|_{z=0}$ at the substrate. With respect to the monolayer upper boundary, we will consider that it is stress free, and therefore $\sigma_{tn} = 0|_{z=h}$ and $\sigma_{nn} - P = -P_{ext}|_{z=h}$. The subscript t and n indicate the tangential and normal directions at the upper surface respectively. From now on, we will take P_{ext} as the origin of pressure.

The cell traction forces need to be balanced by the internal stress. The force balance condition then reads

$$\partial_z \sigma_{xz} + \partial_x \sigma_{xx} - \partial_x P = 0, \tag{7.11}$$

$$\partial_x \sigma_{xz} + \partial_z \sigma_{zz} - \partial_z P = 0. \tag{7.12}$$

As stated in Chapter 4, one of the assumptions of the model is that the cell number as well as the cell volume remains constant. Therefore, the model equations are closed by imposing the incompressibility condition $\partial_x v_x + \partial_z v_z = 0$.

Accordingly, from Eq. (7.12) one obtains that $\sigma_{zz} - P \sim \mathcal{O}(T_x \epsilon)$. The same argument on Eq. (7.11) leads to the conclusion that $\sigma_{xx} - P \sim \mathcal{O}(T_x/\epsilon)$. Altogether, these results imply the equivalence $\sigma_{xx} - P \simeq \sigma_{xx} - \sigma_{zz} = 2\sigma_{xx}$, in which at the last step we use the fact the stress tensor is traceless. In other words, the component σ_{zz} and the pressure fields P are interchangeable.

By averaging along the height direction Eq. (7.11) and using the incompressibility condition we get

$$\partial_x h \langle 2\sigma_{xx} \rangle_h = T_x, \tag{7.13}$$

$$\partial_t h - \partial_x h \langle v_x \rangle_h = 0, \tag{7.14}$$

where the operator $\langle \cdot \rangle_h$ performs the spatial average along the height direction. It is important to remark that the latter equation governs the dynamics of the height of the monolayer, which is allowed to vary in time provided that the product between the integrated volume of the monolayer remains constant (see Fig. (7.4)).

In general, if we consider variations of the system in both the longitudinal and

the transversal directions, the averaged PDEs (7.13-7.14) become

$$\begin{aligned} \partial_x h\langle 2\sigma_{xx} + \sigma_{yy}\rangle_h + \partial_y \langle h\sigma_{xy}\rangle_h &= T_x, & (7.15)\\ \partial_y h\langle \sigma_{xy}\rangle_h + \partial_y h\langle 2\sigma_{yy} + \sigma_{xx}\rangle_h &= T_y, & (7.16)\\ \partial_t h - \partial_x h\langle v_x\rangle_h - \partial_y h\langle v_x\rangle_h &= 0. & (7.17) \end{aligned}$$

In order to simplify the notation, in Section 4.2, we denote the components of the averaged total stress as $\sigma_{xx} = h\langle 2\sigma_{xx} + \sigma_{yy}\rangle_h$, $\sigma_{xy} = h\langle \sigma_{xy}\rangle_h$, $\sigma_{yx} = h\langle \sigma_{yx}\rangle_h$ and $\sigma_{yy} = h\langle 2\sigma_{yy} + \sigma_{xx}\rangle_h$. In addition, we assume that the height of the monolayer is constant through space an time, and takes the value $h = 5$ μm, consistent with the hypothesis of the experimental data in Ref. [51]. Therefore we redefine the parameters of Eq. (4.2) as $\xi/h \to \xi$ and $T_0/h \to T_0$.

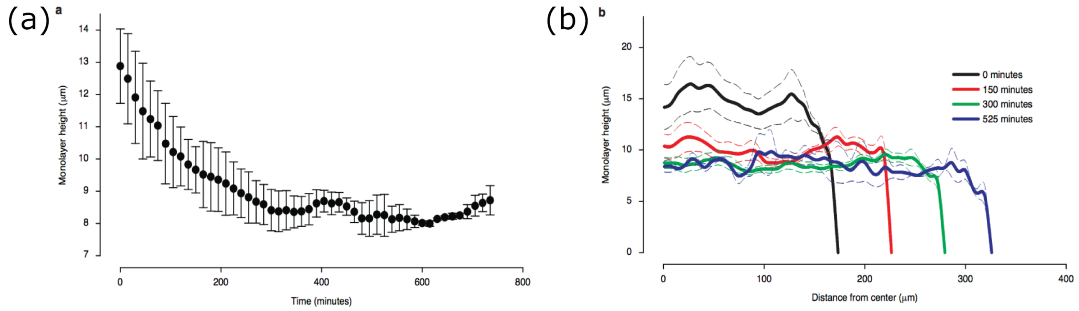

Figure 7.4: (a) Average cell height during monolayer's expansion. Error bars represent the SD (b) Average cell heights as a function of the distance to the monolayer midline at different time points. Dashed lines are the mean±SD. Both figures are modified from Ref. [51]

7.7 Appendix G: Fitting method for stress and velocity profiles

In this section we briefly describe the fitting procedure we have used to obtain the parameters of our model out of the experimentally measured stress and velocity profiles in expanding epithelial monolayer by Trepat's group. The stress and velocity profiles were measured at time intervals of 3 min.

This analysis is carried out with the help of the software *Mathematica*. The algorithm proceeds in the following steps:

1. At each time point, we choose a cutoff on the stress profiles, which is the maximal stress divided by a number. The values of the stress below such cutoff are set equal to zero. The number typically is between 6 and 10.

2. The width of the epithelial monolayer ($2L$) is estimated from the size of the stress profiles.

3. At each time point, we use the function NonlinearModelFit with the ConjugateGradient method on the measured stress profiles and put as a fitting ansatz Eq. (4.11). The outputs that are collected are the estimates and the standard deviations for the parameters T_0 and L_c, which are used as seeds when we apply the function NonlinearModelFit with the ConjugateGradient method with the fitting ansatz from Eq. (4.9). The corresponding outputs that are collected are then the estimate and the standard deviation for the parameter $L_\eta = \sqrt{\eta/\xi}$.

4. At each time point, we use the function NonlinearModelFit with the Conjugate method on the measured velocity profiles and put as a fitting ansatz a linear function of the spatial coordinate. We collect the estimated slope and its standard deviation. Based on the physical model, the numerical integration of the stress profile in space divided by the product between the latter slope and the width of the monolayer, provides a value for the viscosity η. The errors on η are propagated from the standard deviation of the slope.

It is important to remark that the previous method allows us to extract an estimation of the model parameters at every experimental time point.

This algorithm has been used on 4 different experiments for each cell line: MDCK and MCF10A, and one for each drug on MDCK cells: HGF and Blebbistatin. The data shown in Fig. (2.3) is the average among realizations and the error bars are the quadratic sum of the average standard deviations extracted from the algorithm plus the statistical standard deviation.

7.8 Appendix H: Numerical method for the $1d$ cell monolayer

In this section we detail the numerical scheme followed in order to examine the fully nonlinear regime for the one dimensional model proposed to describe the mechanical behavior of $2d$ expanding cell sheets mechanical behaviour when averaged on the transversal direction.

The complete set of equations discussed in Section (4.4.2) read

$$\begin{aligned}
\sigma_{xx} &= \eta\partial_x v_x - \frac{\zeta\Delta\mu}{2}p_x^2 + \frac{\nu_1\rho}{2}\left(p_x - p_x^3 + L_c^2\partial_{xx}p_x\right) \\
\partial_x\sigma_{xx} &= \xi v_x - T_o p_x \\
\partial_t p_x + v_x\partial_x p_x &= \frac{1}{\bar{\gamma}_1}\left(p_x - p_x^3 + L_c^2\partial_{xx}p_x\right) - \frac{\nu_1}{2}p_x\partial_x v_x
\end{aligned}$$

From now on, we will drop the subscript x in all the physical observables.

First, from the second equation, one can extract the velocity profile, and substitute it in the other two equations. Secondly, we add a temporal derivative of the stress profile at the left-hand side of the first equation, as if the passive rheology of the system would be Maxwell-like with a viscoelastic relaxation time scale $\bar{\epsilon}$. With these changes the latter system reads

$$\begin{aligned}
\bar{\epsilon}\partial_t\sigma + \sigma - L_\eta^2\partial_{xx}\sigma &= T_0 L_\eta^2\partial_x p - \frac{\zeta\Delta\mu}{2}p^2 + \frac{\nu_1\rho}{2}\left(p - p^3 + L_c^2\partial_{xx}p\right), \\
\partial_t p - \frac{1}{\bar{\gamma}_1}\left(p + L_c^2\partial_{xx}p\right) &= -\frac{1}{\bar{\gamma}_1}p^3 - \frac{\nu_1}{2\xi}p\left(\partial_{xx}\sigma + T_0\partial_x p\right) - \left(\partial_x\sigma + T_0 p\right)\frac{\partial_x p_x}{\xi},
\end{aligned}$$

which looks like a pair of coupled reaction-diffusion equations.

With respect to the term $\sim \bar{\epsilon}\partial_t\sigma$, we assume implicitly that as long as $\bar{\epsilon} \ll \bar{\gamma}_1$, it will not affect qualitatively the dynamics at time scales larger than $\bar{\epsilon}$. In Fig. (7.5), the temporal evolution of the soliton-like profiles is shown for two values of $\bar{\epsilon}$ significantly different.

The spatial coordinate is discretized as an array of equidistant points separated by a distance Dx. Similarly for the temporal coordinate in which the time step is Dt. Both are left as input parameters in the program.

The latter set of equation are integrated via a semi-implicit method, which treats the linear terms implicitly and the nonlinear terms explicitly. We denote the value of the stress component (polarization) at a given point in space at the time point mDt as σ^m (p^m). In these terms, the discretization of the latter system reads

$$\begin{aligned}
\frac{\bar{\epsilon}}{Dt}\sigma^{m+1} + \sigma^{m+1} - L_\eta^2\partial_{xx}\sigma^{m+1} &= \frac{\bar{\epsilon}}{Dt}\sigma^m + T_0 L_\eta^2\partial_x p^m - \frac{\zeta\Delta\mu}{2}(p^m)^2 \\
&\quad + \frac{\nu_1\rho}{2}p^m\left(p^m - (p^m)^3 + L_c^2\partial_{xx}p^m\right) \\
\frac{p^{m+1}}{Dt} - \frac{1}{\bar{\gamma}_1}\left(p^{m+1} + L_c^2\partial_{xx}p^{m+1}\right) &= \frac{p^m}{Dt} - \frac{1}{\bar{\gamma}_1}(p^m)^3 - \frac{\nu_1}{2\xi}\left(\partial_{xx}\sigma^m + T_o\partial_x p^m\right)p^m \\
&\quad - \left(\partial_x\sigma^m + T_0 p^m\right)\frac{\partial_x p^m}{\xi}
\end{aligned}$$

where, all the spatial derivatives are substituted by the corresponding expressions from the centered finite difference method.

In summary, starting at a certain initial random condition, the numerical program computes the values of the stress and polarization profiles at the subsequent time points, which is equivalent to solving a tridiagonal linear system of equations for which we use a standard method.

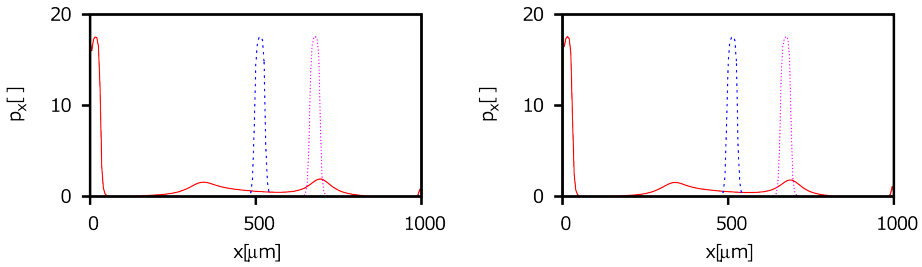

Figure 7.5: Nonlinear trajectories from the cell sheet's model. The values of are $\bar{\epsilon} = 1$ from the left-hand side figure min and $\bar{\epsilon} = 0.1$ min from the other. The parameters are: $\eta = 10^6$ Pa·s, $\xi = 100$ Pa·s/μm^2 , $T_o = 10$ Pa/μ, $L_c = 50$ μm, $\bar{\gamma}_1 = 600$ s, $\nu_1 = 20$, $\rho = 0.1$ Pa and $\zeta\Delta\mu = -1000$ Pa, as in Fig. (4.15). The dashed blue profiles is at the time point 198 min, the dotted pink profile at 144 min and the solid red profile at 93 min. The initial conditions has been imposed to be the same in both figures.

7.9 Appendix I: The Complex Ginzburg-Landau equation for mechanical waves

In this section, we give the basic details to construct the weakly-nonlinear description of the instability into traveling waves described Sec. (4.4.6) in the form of an amplitude equation. Due to the oscillatory character of this instability (Hopf bifurcation) the corresponding amplitude equation takes the form of the so-called Complex Ginzburg-Landau equation. This reproduces the dynamics of the slow and smooth modulations of the traveling waves in our physical model close to the onset.

We particularize the derivation to the case of the physical model of an epithelial monolayer in a $1d$ configuration as described in Sec. (4.4.2), which is given by the set of PDE's

$$\begin{aligned}
\sigma_{xx} &= \eta\partial_x v_x - \frac{\zeta\Delta\mu}{2}p_x^2 + \frac{\nu_1\rho}{2}\left(p_x - p_x^3 + L_c^2\partial_{xx}p_x\right) \\
\partial_x\sigma_{xx} &= \xi v_x - T_o p_x \\
\partial_t p_x + v_x\partial_x p_x &= \frac{1}{\bar{\gamma}_1}\left(p_x - p_x^3 + L_c^2\partial_{xx}p_x\right) - \frac{\nu_1}{2}p_x\partial_x v_x
\end{aligned}$$

so that there are three physical fields: the velocity v_x, the cell polarization p_x and the intracellular stresses σ_{xx}. For simplicity of notation, from now on the subscript x will be dropped.

The homogenous polarized state defined by $p = 1$, $v = T_0/\xi$ and $\sigma = -\zeta\Delta\mu/2$ becomes nearly marginal to periodic longitudinal perturbations with a finite wavenumber q_c given that the coefficient $\nu_1\zeta\Delta\mu < \nu_1^c\zeta\Delta\mu^c$. The critical wavenumber and the threshold of the instability are given by Eq. (4.24) and Eq. (4.23), respectively. In a neighborhood of this bifurcation, there is a separation of time scales between the temporal evolution of modes at the (nearly) marginal band and the stable modes, outside this band. In particular the growth rate at the critical wavenumber can be written as

$$\mathrm{Re}[\omega(q_c)] = \frac{2\left(\nu_1^c\zeta\Delta\mu^c - \nu_1\zeta\Delta\mu\right)}{\eta\left(4 + \frac{L_c}{L_\eta}\sqrt{8 + 2\frac{\bar{\gamma}_1\nu_1^2\rho}{\eta}}\right)} + \mathcal{O}((\nu_1^c\zeta\Delta\mu^c - \nu_1\zeta\Delta\mu)^2).$$

We define the dimensionless parameter $\epsilon \equiv (\nu_1^c\zeta\Delta\mu^c - \nu_1\zeta\Delta\mu)/\nu_1^c\zeta\Delta\mu^c \ll 1$ as a normalized distance to threshold, so that close to the bifurcation we have $Re[\omega(q_c)] \sim \mathcal{O}(\epsilon)$.

On the other hand, our system is infinitely extended along the longitudinal direction, so that there is a continuous family of q-sinusoidal perturbations with a wavenumber close to q_c that are nearly marginal (i.e. $\mathrm{Re}[\omega(q)] \sim \mathcal{O}(\epsilon)$). In addition, from the form of the linear dispersion relation, it turns out that these slowly varying modes are constrained by the condition that $|q - q_c| \sim \mathcal{O}(\epsilon^{1/2})$. Accordingly, the decomposition of the actual pattern as a superposition of fast and slow perturbations, leads to a slow dynamics of a smooth envelope of the dominant mode q_c. The time scale of these modulations is given by the scaling of the growth rate of the unstable modes, of $\mathcal{O}(\epsilon^{-1})$. In addition, the spatial modulations of the critical wavenumber will be expressed as wave packets within the short range of $\mathcal{O}(\epsilon^{1/2})$ in q-space, therefore with a typical scale of spatial variation of the order of $\mathcal{O}(\epsilon^{-1/2})$. The nonlinearities will eventually saturate the growth to a small amplitude of $\mathcal{O}(\epsilon^{1/2})$ (for the case of a supercritical bifurcation), so the solution of the problem will take the form of a wave with wavenumber q_c with a phase velocity given by $v_c = -\mathrm{Im}[\omega(q_c)]/q_c$, with spatial modulations on the scale $\mathcal{O}(\sim \epsilon^{-1/2})$ and temporal dynamics on the scale amplitude $\mathcal{O}(\epsilon^{-1})$. The aim is now to derive an equation for the modulations envelope.

We need to solve in a self-consistent manner the PDEs of the physical model near the bifurcation point within an expansion on the distance to threshold.

Therefore, we will propose an ansatz of the form

$$\begin{aligned} p &= 1+\sum_{n=1}^{\infty}\sum_{m=-n}^{n}\epsilon^{n/2}p_n^m(X,T)e^{imq_c(x-v_ct)} \\ v &= \frac{T_0}{\xi}+\sum_{n=1}^{\infty}\sum_{m=-n}^{n}\epsilon^{n/2}v_n^m(X,T)e^{imq_c(x-v_ct)} \\ \sigma &= -\frac{\zeta\Delta\mu}{2}+\sum_{n=1}^{\infty}\sum_{m=-n}^{n}\epsilon^{n/2}\sigma_n^m(X,T)e^{imq_c(x-v_ct)} \\ V &= \sum_{n=0}^{\infty}\epsilon^{n/2}V_n \end{aligned}$$

where p_n^m, v_n^m and σ_n^m are functions of the long spatial variables $X \equiv \epsilon^{1/2}(x+Vt)$ and the slow temporal variable $T \equiv \epsilon t$. V is a power series of $\epsilon^{1/2}$, whose coefficients are left as unknown quantities. One of the advantages of these calculations is that there is a unique choice of the scaling of the variables in ϵ that leads to consistent results.

At this point, we plug them into the PDEs of the physical model and organize consistently the different terms in powers of $\epsilon^{1/2}$. We fix that $\zeta\Delta\mu = \nu_1^c\zeta\Delta\mu^c/\nu_1$. The first order contributions establish a set of linear relations between σ_1^m, v_1^m and p_1^m. The system is undetermined but consistent. As an example these coefficients in units of $\bar{\gamma}_1 = \xi = \eta = 1$ read

$$\begin{aligned} \sigma_1^1(X,T) &= \frac{4L_c\sqrt{8+2\nu_1^2\rho}-L_c^2\left(4+\left(q_c^2\left(4+\nu_1^2\rho\right)\right)\right)+4iq_c(v_c-T_0)}{2\nu_1}p_1^1(X,T) \\ v_1^1(X,T) &= \frac{2q_c\left(iL_c^2q_c+v_c-T_0\right)+4i}{\nu_1 q_c}p_1^1(X,T) \end{aligned}$$

Similarly the second order contributions also imposes linear relations between σ_2^m, v_2^m, p_2^m and V_1, although now we have to impose a solvability condition which connects them with p_1^m. The solvability conditions are usually used in problems of the form $La = \epsilon N(a)$ to construct particular solutions applying perturbative theory in a self-consistent manner, where L is a linear operator and N a non-linear function. Finally, solving the third order contributions and imposing the solvability condition, it leads to the Complex Ginzburg-Landau equation of the form.

$$\partial_T p_1^1 = p_1^1 - c_1(1+ic)|p_1^1|^2p_1^1 + (1+ib)\partial_{XX}^2 p_1^1, \tag{7.18}$$

being c_1, c and b parameters that depend on the physical properties of the system. With respect to the Complex Ginzburg-Landau equation provided in Section (4.4.6), the variable $p_1^1 \to A$. Due to the fact that the bifurcation is oscilla-

tory (Hopf) the coefficients of the amplitude equations are non real, in contrast to the case of the Real Ginzburg-Landau equation for the complex amplitude in stationary bifurcations. A fundamental difference between the Real and the Complex Ginzburg-Landau equations is that the former is purely relaxational, that is, it exists a Lyapunov functional that is maximized by time evolution. On the contrary if the coefficients are complex, no such Lypaunov functional exists and the equation may involve persistent dynamics, opening the door for instance to spatio-temporal chaos.

Finally for completeness, we give the analytical expressions of the coefficients c_1, c and b as

$$c_1 = -\frac{f_1 f_2 + f_3 f_4}{f_2^2 + f_3^2}, \tag{7.19}$$

$$c = -\frac{f_2 f_4 - f_1 f_3}{|f_1 f_2 + f_3 f_4|}, \tag{7.20}$$

$$b = \frac{F}{2}\frac{(4 - 3G\sqrt{8+2H})}{\sqrt{G}\sqrt[4]{8+2H}(8+G\sqrt{8+2H})^2}, \tag{7.21}$$

in which the functions f_1, f_2, f_3 and f_4 expressed in terms of the physical parameters reads

$$\begin{aligned}
f_1 = {} & 16\Big\{2G^5(H+4)^2\Big[27\nu_1^2 - 42\nu_1 - 8\Big] + 16\sqrt{2}(H+4)^{3/2}\Big[H^2\nu_1^2 + H\nu_1 - 20\Big] \\
& -2\sqrt{2}G^4(H+4)^{3/2}\Big[3(5H-36)\nu_1^2 + (13H+228)\nu_1 + 2(H+52)\Big] \\
& -G^3(H+4)\Big[H^2(65\nu_1^2 - 104\nu_1 - 4) + 4H(135\nu_1^2 - 52\nu_1 + 52) \\
& -16(27\nu_1^2 - 90\nu_1 - 128)\Big] \\
& +2\sqrt{2}G^2\sqrt{H+4}\Big[2H^3\nu_1(\nu_1+11) - 3H^2(35\nu_1^2 - 96\nu_1 + 4) \\
& -12H(51\nu_1^2 - 62\nu_1 + 44) - 32(3\nu_1 + 76)\Big] \\
& +8G(H+4)\Big[H(H^2+6H-48)\nu_1^2 + (23H^2+100H+48)\nu_1 - 4(9H+88)\Big]\Big\} \\
& -F^2(H+4)\nu_1^2\Big\{\sqrt{2}G^2\sqrt{H+4}(\nu_1+2)\Big[H(\nu_1+2) + 52\nu_1 - 88\Big] \\
& -8G\Big[4(H+4)\nu_1^2 + (13H+4)\nu_1 + 2(5H+68)\Big] - 96\sqrt{2}\sqrt{H+4}(\nu_1+4)\Big\} \\
f_2 = {} & 12\sqrt{G}(H+4)^{3/2}\nu_1^2\left(G\sqrt{H+4} + 2\sqrt{2}\right)\left(3G^{3/2}(H+4) + 6\sqrt{2}\sqrt{G(H+4)}\right) \\
f_3 = {} & -24\sqrt[4]{2}F\sqrt{G}(H+4)^{7/4}\nu_1^3\left(G\sqrt{H+4} + 2\sqrt{2}\right)
\end{aligned}$$

$$
\begin{aligned}
f_4 \;=\; & 3\sqrt[4]{2}F\sqrt{G}\sqrt[4]{H+4}\nu_1\Big\{-4G^3(H+4)\Big[(9H+68)\nu_1^2+4(H-12)\nu_1-28(H+4)\Big] \\
& +\sqrt{2}G^2\sqrt{H+4}\Big[5H^2\left(3\nu_1^2+10\nu_1+8\right)+32H\left(\nu_1^2+7\nu_1+26\right) \\
& -368\nu_1^2+608\nu_1+2688\Big] \\
& +4G(H+4)\Big[\left(2H^2+63H+44\right)\nu_1^2+4\left(H^2+8H+28\right)\nu_1+96(H+7)\Big] \\
& +16\sqrt{2}(H+4)^{3/2}\left(3H\nu_1^2+(7-4H)\nu_1+28\right)\Big\}
\end{aligned}
$$

where $F = T_0\bar{\gamma}_1/(\xi L_\eta)$, $H = \bar{\gamma}_1\nu_1^2\rho/\eta$ and $G = L_c/L_\eta$.

References

[1] Marchetti MC, Joanny JF, Ramaswamy S, Liverpool TB, Prost J, et al. (2013) Hydrodynamics of soft active matter. Rev Mod Phys 85: 1143–1189.

[2] Kruse K, Joanny JF, Jülicher F, Prost J, Sekimoto K (2005) Generic theory of active polar gels: a paradigm for cytoskeletal dynamics. The European Physical Journal E 16: 5-16.

[3] Jülicher F, Kruse K, Prost J, Joanny JF (2007) Active behavior of the cytoskeleton. Physics Reports 449: 3 - 28.

[4] Parrish JK, Hamner WM (1997). Animals Groups in Three Dimensions: How Species Aggregate (Cambridge University Press, Cambridge, England).

[5] Trepat X, Wasserman MR, Angelini TE, Millet E, Weitz DA, et al. (2009) Physical forces during collective cell migration. Nat Phys 5: 426–430.

[6] Rafaï S, Jibuti L, Peyla P (2010) Effective viscosity of microswimmer suspensions. Phys Rev Lett 104: 098102.

[7] Bendix PM, Koenderink GH, Cuvelier D, Dogic Z, Koeleman BN, et al. (2008) A quantitative analysis of contractility in active cytoskeletal protein networks. Biophysical Journal 94: 3126 - 3136.

[8] Giomi L, Liverpool TB, Marchetti MC (2010) Sheared active fluids: Thickening, thinning, and vanishing viscosity. Phys Rev E 81: 051908.

[9] Saintillan D (2010) The dilute rheology of swimming suspensions: A simple kinetic model. Experimental Mechanics 50: 1275-1281.

[10] Alberts B, Bray D, Lewis J, Raff M, Roberts K, et al. (2004). Molecular Biology of the Cell (Garland, New York).

[11] Howard J (2001). Mechanics of Motor Proteins and the Cytoskeleton. (Sinauer Press: Sunderland, Massachusetts).

[12] Bray D (1992). Cell Movements (Garland, New York).

[13] Cavagna A, Giardina I (2014) Bird flocks as condensed matter. Annual Review of Condensed Matter Physics 5: 183-207.

[14] Deneubourg J, Goss S (1989) Collective patterns and decision-making. Ethology Ecology & Evolution 1: 295-311.

[15] Karamouzas I, Skinner B, Guy SJ (2014) Universal power law governing pedestrian interactions. Phys Rev Lett 113: 238701.

[16] Kruse K, Joanny JF, Jülicher F, Prost J, Sekimoto K (2004) Asters, vortices, and rotating spirals in active gels of polar filaments. Phys Rev Lett 92: 078101.

[17] Voituriez R, Joanny JF, Prost J (2005) Spontaneous flow transition in active polar gels. EPL (Europhysics Letters) 70: 404.

[18] Kruse K, Joanny JF, Jülicher F, Prost J (2006) Contractility and retrograde flow in lamellipodium motion. Physical Biology 3: 130.

[19] Voituriez R, Joanny JF, Prost J (2006) Generic phase diagram of active polar films. Phys Rev Lett 96: 028102.

[20] Joanny JF, Jülicher F, Kruse K, Prost J (2007) Hydrodynamic theory for multi-component active polar gels. New Journal of Physics 9: 422.

[21] Basu A, Joanny J, Jülicher F, Prost J (2008) Thermal and non-thermal fluctuations in active polar gels. The European Physical Journal E 27: 149-160.

[22] Salbreux G, Prost J, Joanny JF (2009) Hydrodynamics of cellular cortical flows and the formation of contractile rings. Phys Rev Lett 103: 058102.

[23] Yam PT, Wilson CA, Ji L, Hebert B, Barnhart EL, et al. (2007) Actin-myosin network reorganization breaks symmetry at the cell rear to spontaneously initiate polarized cell motility. The Journal of Cell Biology 178: 1207-1221.

[24] Wilson CA, Tsuchida MA, Allen GM, Barnhart EL, Applegate KT, et al. (2010) Myosin II contributes to cell-scale actin network treadmilling through network disassembly. Nature 465: 373–377.

[25] Keren K, Pincus Z, Allen GM, Barnhart EL, Marriott G, et al. (2008) Mechanism of shape determination in motile cells. Nature 453: 475–480.

[26] Mayor R, Carmona-Fontaine C (2010) Keeping in touch with contact inhibition of locomotion. Trends in Cell Biology 20: 319 - 328.

[27] Lodish H, Berk A, Zipursky SL, Matsudaira P, Baltimore D, et al. (2000). Molecular Cell Biology (W. H. Freeman & Company).

[28] Ananthakrishnan R, Ehrlicher A (2007) The forces behind cell movement. International journal of biological sciences 3: 303 - 317.

[29] Svitkina TM, Borisy GG (1999) Arp2/3 complex and actin depolymerizing factor/cofilin in dendritic organization and treadmilling of actin filament array in lamellipodia. The Journal of Cell Biology 145: 1009-1026.

[30] Verkhovsky AB, Svitkina TM, Borisy GG (1999) Self-polarization and directional motility of cytoplasm. Current Biology 9: 11 - S1.

[31] Fournier MF, Sauser R, Ambrosi D, Meister JJ, Verkhovsky AB (2010) Force transmission in migrating cells. The Journal of Cell Biology 188: 287-297.

[32] Lecuit T, Le Goff L (2007) Orchestrating size and shape during morphogenesis. Nature 450: 189–192.

[33] Saucedo LJ, Edgar BA (2007) Filling out the hippo pathway. Nat Rev Mol Cell Biol 8: 613-621.

[34] Burke R, Basler K (1996) Dpp receptors are autonomously required for cell proliferation in the entire developing drosophila wing. Development 122: 2261-2269.

[35] Martín-Castellanos C, Edgar BA (2002) A characterization of the effects of dpp signaling on cell growth and proliferation in the drosophila wing. Development 129: 1003-1013.

[36] Bryant PJ, A Schneiderman H (1969) Cell lineage, growth, and determination in the imaginal leg discs of drosophila melanogaster. Developmental Biology 20: 263 - 290.

[37] Baena-López LA, Baonza A, García-Bellido A (2005) The orientation of cell divisions determines the shape of drosophila organs. Current Biology 15: 1640-1644.

[38] Bornens M (2008) Organelle positioning and cell polarity. Nat Rev Mol Cell Biol 9: 874–886.

[39] Martin-Belmonte F, Mostov K (2008) Regulation of cell polarity during epithelial morphogenesis. Current Opinion in Cell Biology 20: 227 - 234.

[40] Lee M, Vasioukhin V (2008) Cell polarity and cancer-cell and tissue polarity as a non-canonical tumor suppressor. Journal of Cell Science 121: 1141-1150.

[41] DuFort CC, Paszek MJ, Weaver VM (2011) Balancing forces: architectural control of mechanotransduction. Nat Rev Mol Cell Biol 12: 308–319.

[42] Perez-Moreno M, Jamora C, Fuchs E (2003) Sticky business: Orchestrating cellular signals at adherens junctions. Cell 112: 535 - 548.

[43] Tamura A, Kitano Y, Hata M, Katsuno T, Moriwaki K, et al. (2008) Megaintestine in claudin-15-deficient mice. Gastroenterology 134: 523 - 534.e3.

[44] Niessen CM, Gottardi CJ (2008) Molecular components of the adherens junction. Biochimica et Biophysica Acta (BBA) - Biomembranes 1778: 562 - 571.

[45] Ligon LA, Karki S, Tokito M, Holzbaur ELF (2001) Dynein binds to β-catenin and may tether microtubules at adherens junctions. Nat Cell Biol 3: 913–917.

[46] Drees F, Pokutta S, Yamada S, Nelson WJ, Weis WI (2005) α-catenin is a molecular switch that binds e-cadherin-β-catenin and regulates actin-filament assembly. Cell 123: 903 - 915.

[47] Meng W, Takeichi M (2009) Adherens junction: Molecular architecture and regulation. Cold Spring Harbor Perspectives in Biology 1.

[48] Cereijido M, Contreras RG, Shoshani L, Flores-Benitez D, Larre I (2008) Tight junction and polarity interaction in the transporting epithelial phenotype. Biochimica et Biophysica Acta (BBA) - Biomembranes 1778: 770 - 793.

[49] Matter K, Balda MS (2003) Signalling to and from tight junctions. Nat Rev Mol Cell Biol 4: 225–237.

[50] Tambe DT, Corey Hardin C, Angelini TE, Rajendran K, Park CY, et al. (2011) Collective cell guidance by cooperative intercellular forces. Nat Mater 10: 469–475.

[51] Serra-Picamal X, Conte V, Vincent R, Anon E, Tambe DT, et al. (2012) Mechanical waves during tissue expansion. Nat Phys 8: 628–634.

[52] de Gennes PG, Prost J (1993). The Physics of Liquid Crystals (Clarendon Press, Oxford).

[53] Ziebert F, Swaminathan S, Aranson IS (2011) Model for self-polarization and motility of keratocyte fragments. Journal of The Royal Society Interface .

[54] Shao D, Levine H, Rappel WJ (2012) Coupling actin flow, adhesion, and morphology in a computational cell motility model. Proceedings of the National Academy of Sciences 109: 6851-6856.

[55] Callan-Jones AC, Joanny JF, Prost J (2008) Viscous-fingering-like instability of cell fragments. Phys Rev Lett 100: 258106.

[56] Bensimon D, Kadanoff LP, Liang S, Shraiman BI, Tang C (1986) Viscous flows in two dimensions. Rev Mod Phys 58: 977–999.

[57] Casademunt J, Magdaleno F (2000) Dynamics and selection of fingering patterns. recent developments in the saffman-taylor problem. Physics Reports 337: 1 - 35.

[58] Casademunt J (2004) Viscous fingering as a paradigm of interfacial pattern formation: Recent results and new challenges. Chaos: An Interdisciplinary Journal of Nonlinear Science 14: 809-824.

[59] Ben Amar M, Manyuhina O, Napoli G (2011) Cell motility: A viscous fingering analysis of active gels. The European Physical Journal Plus 126: 19.

[60] Tjhung E, Marenduzzo D, Cates ME (2012) Spontaneous symmetry breaking in active droplets provides a generic route to motility. Proceedings of the National Academy of Sciences 109: 12381-12386.

[61] Doubrovinski K, Kruse K (2011) Cell motility resulting from spontaneous polymerization waves. Phys Rev Lett 107: 258103.

[62] A Whitfield C, Marenduzzo D, Voituriez R, J Hawkins R (2014) Active polar fluid flow in finite droplets. The European Physical Journal E 37: 8.

[63] Hawkins RJ, Poincloux R, Bénichou O, Piel M, Chavrier P, et al. (2011) Spontaneous contractility-mediated cortical flow generates cell migration in three-dimensional environments. Biophysical Journal 101: 1041 - 1045.

[64] Recho P, Truskinovsky L (2013) Asymmetry between pushing and pulling for crawling cells. Phys Rev E 87: 022720.

[65] Recho P, Joanny JF, Truskinovsky L (2014) Optimality of contraction-driven crawling. Phys Rev Lett 112: 218101.

[66] Shao D, Rappel WJ, Levine H (2010) Computational model for cell morphodynamics. Phys Rev Lett 105: 108104.

[67] Hawkins RJ, Piel M, Faure-Andre G, Lennon-Dumenil AM, Joanny JF, et al. (2009) Pushing off the walls: A mechanism of cell motility in confinement. Phys Rev Lett 102: 058103.

[68] Hawkins RJ, Voituriez R (2010) Mechanisms of cell motion in confined geometries. Mathematical Modelling of Natural Phenomena 5: 84–105.

[69] Callan-Jones AC, Voituriez R (2013) Active gel model of amoeboid cell motility. New Journal of Physics 15: 025022.

[70] Dreher A, Aranson IS, Kruse K (2014) Spiral actin-polymerization waves can generate amoeboidal cell crawling. New Journal of Physics 16: 055007.

[71] Cummings LJ, Howison SD, King JR (1999) Two-dimensional stokes and hele-shaw flows with free surfaces. European Journal of Applied Mathematics null: 635–680.

[72] Miranda JA, Gadêlha H, Dorsey AT (2010) Coriolis effects on rotating hele-shaw flows: A conformal-mapping approach. Phys Rev E 82: 066306.

[73] Crawford JD (1991) Introduction to bifurcation theory. Rev Mod Phys 63: 991–1037.

[74] Guckenheimer J, Holmes P (1983). Nonlinear oscillations, dynamical systems, and bifurcations of vector fields.

[75] LeGoff L, Rouault H, Lecuit T (2013) A global pattern of mechanical stress polarizes cell divisions and cell shape in the growing drosophila wing disc. Development 140: 4051-4059.

[76] Campinho P, Behrndt M, Ranft J, Risler T, Minc N, et al. (2013) Tension-oriented cell divisions limit anisotropic tissue tension in epithelial spreading during zebrafish epiboly. Nat Cell Biol 15: 1405–1414.

[77] Bryant DM, Mostov KE (2008) From cells to organs: building polarized tissue. Nat Rev Mol Cell Biol 9: 887–901.

[78] Tlili S, Gay C, Graner F, Marcq P, Molino F, et al. (2013) Mechanical formalism for tissue dynamics. ArXiv e-prints .

[79] Murugesan YK, Pasini D, Rey AD (2011) Microfibril organization modes in plant cell walls of variable curvature: a model system for two dimensional anisotropic soft matter. Soft Matter 7: 7078.

[80] Corson F, Hamant O, Bohn S, Traas J, Boudaoud A, et al. (2009) Turning a plant tissue into a living cell froth through isotropic growth. Proceedings of the National Academy of Sciences 106: 8453-8458.

[81] Tindemans SH, Hawkins RJ, Mulder BM (2010) Survival of the aligned: Ordering of the plant cortical microtubule array. Phys Rev Lett 104: 058103.

[82] Bittig T, Wartlick O, Gonzàlez-Gaitàn M, Jülicher F (2009) Quantification of growth asymmetries in developing epithelia. The European Physical Journal E 30: 93-99.

[83] Ranft J, Basan M, Elgeti J, Joanny JF, Prost J, et al. (2010) Fluidization of tissues by cell division and apoptosis. Proceedings of the National Academy of Sciences 107: 20863-20868.

[84] Rodriguez EK, Hoger A, McCulloch AD (1994) Stress-dependent finite growth in soft elastic tissues. Journal of Biomechanics 27: 455 - 467.

[85] Amar MB, Goriely A (2005) Growth and instability in elastic tissues. Journal of the Mechanics and Physics of Solids 53: 2284 - 2319.

[86] Köpf MH, Pismen LM (2013) A continuum model of epithelial spreading. Soft Matter 9: 3727.

[87] Bittig T, Wartlick O, Kicheva A, Gonzàlez-Gaitàn M, Jülicher F (2008) Dynamics of anisotropic tissue growth. New Journal of Physics 10: 063001.

[88] Kollmannsberger P, Bidan CM, Dunlop JWC, Fratzl P (2011) The physics of tissue patterning and extracellular matrix organisation: how cells join forces. Soft Matter 7: 9549.

[89] Ranft J, Prost J, Jülicher F, Joanny JF (2012) Tissue dynamics with permeation. The European Physical Journal E 35: 46.

[90] Foty RA, Forgacs G, Pfleger CM, Steinberg MS (1994) Liquid properties of embryonic tissues: Measurement of interfacial tensions. Phys Rev Lett 72: 2298–2301.

[91] Blanch-Mercader C, Casademunt J (2013) Spontaneous motility of actin lamellar fragments. Phys Rev Lett 110: 078102.

[92] Lee P, Wolgemuth CW (2011) Crawling cells can close wounds without purse strings or signaling. PLoS Comput Biol 7: e1002007.

[93] Basan M, Joanny JFc, Prost J, Risler T (2011) Undulation instability of epithelial tissues. Phys Rev Lett 106: 158101.

[94] Abramowitz M, Stegun IA (1972) Handbook of Mathematical Functions.

[95] Álvarez-Lacalle E, Ortín J, Casademunt J (2004) Nonlinear saffman-taylor instability. Phys Rev Lett 92: 054501.

[96] Lira SA, Miranda JA, Oliveira RM (2010) Stationary shapes of confined rotating magnetic liquid droplets. Phys Rev E 82: 036318.

[97] Cummings LJ, Howison SD, King JR (1997) Conserved quantities in stokes flow with free surfaces. Physics of Fluids (1994-present) 9: 477-480.

[98] Montel F, Delarue M, Elgeti J, Malaquin L, Basan M, et al. (2011) Stress clamp experiments on multicellular tumor spheroids. Phys Rev Lett 107: 188102.

[99] Godrèche C (1992) Solids far from Equilibrium.

[100] Manning ML, Foty RA, Steinberg MS, Schoetz EM (2010) Coaction of intercellular adhesion and cortical tension specifies tissue surface tension. Proceedings of the National Academy of Sciences 107: 12517-12522.

[101] Aigouy B, Farhadifar R, Staple DB, Sagner A, Röper JC, et al. (2010) Cell flow reorients the axis of planar polarity in the wing epithelium of drosophila. Cell 142: 773 - 786.

[102] Sonnemann KJ, Bement WM (2011) Wound repair: Toward understanding and integration of single-cell and multicellular wound responses. Annual Review of Cell and Developmental Biology 27: 237-263.

[103] Brugues A, Anon E, Conte V, Veldhuis JH, Gupta M, et al. (2014) Forces driving epithelial wound healing. Nat Phys 10: 683–690.

[104] Cochet-Escartin O, Ranft J, Silberzan P, Marcq P (2014) Border forces and friction control epithelial closure dynamics. Biophysical Journal 106: 65 - 73.

[105] Wood W, Jacinto A, Grose R, Woolner S, Gale J, et al. (2002) Wound healing recapitulates morphogenesis in drosophila embryos. Nat Cell Biol 4: 907–912.

[106] Friedl P, Gilmour D (2009) Collective cell migration in morphogenesis, regeneration and cancer. Nat Rev Mol Cell Biol 10: 445–457.

[107] du Roure O, Saez A, Buguin A, Austin RH, Chavrier P, et al. (2005) Force mapping in epithelial cell migration. Proceedings of the National Academy of Sciences of the United States of America 102: 2390-2395.

[108] Leckband DE, le Duc Q, Wang N, de Rooij J (2011) Mechanotransduction at cadherin-mediated adhesions. Current Opinion in Cell Biology 23: 523 - 530.

[109] Vedula SRK, Leong MC, Lai TL, Hersen P, Kabla AJ, et al. (2012) Emerging modes of collective cell migration induced by geometrical constraints. Proceedings of the National Academy of Sciences 109: 12974-12979.

[110] Lambert M, Thoumine O, Brevier J, Choquet D, Riveline D, et al. (2007) Nucleation and growth of cadherin adhesions. Experimental Cell Research 313: 4025 - 4040.

[111] Foote HP, Sumigray KD, Lechler T (2013) Frap analysis reveals stabilization of adhesion structures in the epidermis compared to cultured keratinocytes. PLoS ONE 8: e71491.

[112] Kopf MH, Pismen LM (2013) A continuum model of epithelial spreading. Soft Matter 9: 3727-3734.

[113] Basan M, Elgeti J, Hannezo E, Rappel WJ, Levine H (2013) Alignment of cellular motility forces with tissue flow as a mechanism for efficient wound healing. Proceedings of the National Academy of Sciences 110: 2452-2459.

[114] Weber GF, Bjerke MA, DeSimone DW (2012) A mechanoresponsive cadherin-keratin complex directs polarized protrusive behavior and collective cell migration. Developmental Cell 22: 104 - 115.

[115] Lee P, Wolgemuth C (2011) Advent of complex flows in epithelial tissues. Phys Rev E 83: 061920.

[116] Aranson IS, Sokolov A, Kessler JO, Goldstein RE (2007) Model for dynamical coherence in thin films of self-propelled microorganisms. Phys Rev E 75: 040901.

[117] Schwarz US, Safran SA (2013) Physics of adherent cells. Rev Mod Phys 85: 1327–1381.

[118] Thomas WA, Boscher C, Chu YS, Cuvelier D, Martinez-Rico C, et al. (2013) α-catenin and vinculin cooperate to promote high e-cadherin-based adhesion strength. Journal of Biological Chemistry 288: 4957-4969.

[119] Jülicher F, Prost J (2009) Generic theory of colloidal transport. The European Physical Journal E 29: 27-36.

[120] Tojkander S, Gateva G, Lappalainen P (2012) Actin stress fibers-assembly, dynamics and biological roles. Journal of Cell Science 125: 1855-1864.

[121] Weber GF, Bjerke MA, DeSimone DW (2011) Integrins and cadherins join forces to form adhesive networks. Journal of Cell Science 124: 1183-1193.

[122] Sponsel HT, Breckon R, Hammond W, Anderson RJ (1994) Mechanisms of recovery from mechanical injury of renal tubular epithelial cells. American Journal of Physiology - Renal Physiology 267: F257–F264.

[123] Straight AF, Cheung A, Limouze J, Chen I, Westwood NJ, et al. (2003) Dissecting temporal and spatial control of cytokinesis with a myosin ii inhibitor. Science 299: 1743-1747.

[124] Mizuno D, Tardin C, Schmidt CF, MacKintosh FC (2007) Nonequilibrium mechanics of active cytoskeletal networks. Science 315: 370-373.

[125] Kim T, Gardel ML, Munro E (2014) Determinants of fluidlike behavior and effective viscosity in cross-linked actin networks. Biophysical Journal 106: 526 - 534.

[126] Petitjean L, Reffay M, Grasland-Mongrain E, Poujade M, Ladoux B, et al. (2010) Velocity fields in a collectively migrating epithelium. Biophysical Journal 98: 1790 - 1800.

[127] Deforet M, Hakim V, Yevick H, Duclos G, Silberzan P (2014) Emergence of collective modes and tri-dimensional structures from epithelial confinement. Nat Commun 5: –.

[128] Banerjee S, Marchetti MC (2012) Contractile stresses in cohesive cell layers on finite-thickness substrates. Phys Rev Lett 109: 108101.

[129] Farooqui R, Fenteany G (2005) Multiple rows of cells behind an epithelial wound edge extend cryptic lamellipodia to collectively drive cell-sheet movement. Journal of Cell Science 118: 51-63.

[130] Muhuri S, Rao M, Ramaswamy S (2007) Shear-flow-induced isotropic-to-nematic transition in a suspension of active filaments. EPL (Europhysics Letters) 78: 48002.

[131] Aranson IS, Kramer L (2002) The world of the complex ginzburg-landau equation. Reviews of Modern Physics 74: 99.

[132] Manneville P (1995) Dissipative structures and weak turbulence .

[133] Casademunt J (2014). Lectures of Nonlinear Physics (unpublished).

[134] Tjhung E, Cates ME, Marenduzzo D (2011) Nonequilibrium steady states in polar active fluids. Soft Matter 7: 7453-7464.

[135] Pliss VA (1964) A reduction principle in the theory of stability of motion. Izv Akad Nauk SSSR Ser Mat 28: 1297–1324.

[136] Shoshitaishvili A (1972) Bifurcations of topological type at singular points of parametrized vector fields. Functional Analysis and Its Applications 6: 169-170.

[137] Apostol TM (1970) Resultants of cyclotomic polynomials. Proc Amer Math Soc 24: 457.